EFFECTS OF THE LOCAL MICROMECHANICS AND ELECTROCHEMISTRY ON THE GALVANIC CORROSION OF AA7050-7451

by

Andrea Nicolas Flores

A Dissertation

Submitted to the Faculty of Purdue University

In Partial Fulfillment of the Requirements for the degree of

Doctor of Philosophy

School of Aeronautics and Astronautics

West Lafayette, Indiana

May 2019

THE PURDUE UNIVERSITY GRADUATE SCHOOL
STATEMENT OF COMMITTEE APPROVAL

Dr. Michael D Sangid, Chair

Department of Aeronautics and Astronautics

Dr. Weinong W. Chen

Department of Aeronautics and Astronautics

Dr. Pablo D. Zavattieri

Lyles School of Civil Engineering

Dr. James T. Burns

University of Virginia, Department of Materials Science and Engineering

Approved by:

Dr. Weinong W. Chen

Head of the Graduate Program

To my parents, Luz Maria and Jaime, my siblings, Nadia, and Jaime, my lovely lab mates, my advisor Dr. Sangid, and to you, dear reader.

ACKNOWLEDGMENTS

First and foremost, I would like to thoroughly thank my research advisor Dr. Michael Sangid for his continuous support during my doctoral studies at Purdue University. This work would not have been possible without his constant guidance and patience to my many queries. He not only introduced me to the world of research, but motivated me to go further and explore new ideas, methods, and fields. I will be forever thankful to him and will always look up to him both as a researcher and as a person. I would also like to acknowledge the agencies that supported my work. In particular the Office of Naval Research, Materials division (N00014-14-1-0544) under program manager Mr. Bill Nickerson. I would also like to thank Purdue University for his financial support through the Bilsland Dissertation Fellowship, which enabled the completion of this document.

This work would not have been possible without Dr. Alberto Mello, who performed some of the experimental work described in this document. It was an absolute pleasure working alongside him and I will be forever grateful for his support both as a coworker and as a friend. Similarly, I would like to thank Prof. James Burns and Dr. Noelle Co, our collaborators at University of Virginia who aided with the study of corrosion fatigue crack initiation. Their experimental work, prompt feedback, and sense of humor are greatly appreciated. Also, I would like to thank Dr. Andrea Rovinelli and Dr. Ricardo Lebensohn for their support with the crystal plasticity framework, as well as Dr. David Johnson and Dr. Yiwei Sun for their aid with the development of the subsurface minimization framework. Special thanks to Dr. Schaber, Dr. Gilpin, and Mr. Root for their aid with the multiple microscopes used throughout this work.

I would like to give special thanks to my present and former lab mates, who have become my family away from home: John, Kartik, Ajey, Imad, Prithivi, Ritwik, Ronald, Diwakar, Todd, Andrea, Priya, Sai, Stephen, Lena, Sven, Greg, Alex etc, for their insightful discussions both inside and outside the laboratory. It was a great pleasure working in such a vibrant environment and I am looking forward to collaborating with them in the near future. Finally, I would like to thank Mom, Dad, Nadia, James, and Sihun for their constant checkups throughout these years. To them I owe my sanity, or what is left of it.

TABLE OF CONTENTS

LIST OF TABLES

LIST OF FIGURES

ABBREVIATIONS

EVP-FFT	Elasto Visco Plastic Fast fourier Transform
EBSD	Electron BackScatter Diffraction
EDX / EDS	Energy Dispersive X-ray Spectroscopy
CLSM	Confocal Laser Surface Microscopy
XCT	X-ray Computer Tomography
ROI	Region of Interest
2D	Two-dimensional
3D	Three-dimensional
FIP	Fatigue Indicator Parameter
GB	Grain Boundary
SEM	Scanning Electron Microscopy
DIC	Digital Image Correlation
LT	Long transverse
TS	Transverse Short
TL	Transverse Long
FCC	Face Centered Cubic
CRSS	Critical Resolved Shear Stress
CP	Crystal Plasticity
FEM	Finite Element Modeling
DP	Discrete Pitting
FIS	Fissure Corrosion
NP	Nano Particles

ABSTRACT

Author: Nicolas, Andrea. PhD
Institution: Purdue University
Degree Received: May 2019
Title: Effect of Micromechanics and Electrochemistry on the Galvanic Corrosion of AA7050-7451
Committee Chair: Michael D. Sangid

The service life of aircraft structure, primarily composed of aluminum alloys, is markedly lower when galvanic corrosion is present due to early crack initiation at localized pitting, with the likelihood of cracking being higher at pits spanning several microns. To understand the joint effect that the mechanical and chemical behavior of AA7050-T7451 have on the evolution of corrosion prior and until its transition to cracking, the microstructure, constituent particles, mechanical strains, and the corrosion morphology were experimentally characterized using high-resolution methods and the mechanical stresses are computationally modeled at the micrometer level using a FFT-based crystal plasticity framework.

The material was corroded under both mechanically loaded and unloaded conditions under different corrosion intervals to properly capture the evolution of corrosion before, during, and after particle fallout. For the events prior to cracking, statistical cross-correlations between the mechanical state of the material and the corrosion morphology were performed to understand the mechanisms driving corrosion at its various stages. For the cracking event and its subsequent growth, the joint analysis of strains and stresses obtained from 3D crystal plasticity models were used to calculate Fatigue Indicator Parameters (FIPs) that can quantitatively give an insight of the major mechanisms driving crack initiation and growth in pre-corroded materials. The development of micromechanical models that account for both the environmental degradation and the microstructure in the material allowed to accurately predict the location of crack initiation arising from pits, which has been a longstanding problem in the field of corrosion. It is concluded that both corrosion growth and its transition to cracking are multivariable events, where corrosion growth is jointly driven by the local chemistry and the micromechanics, and crack initiation is driven by the coupled interaction between the corrosion geometry and the micromechanics.

1. INTRODUCTION

Localized corrosion is a feature that limits the life of many aircraft components as it is a precursor to cracking. For rolled AA7050-T7451, a material regularly used for airframe structures given its strength-to-weight ratio, pitting initiates at cathodic particles that corrode the surrounding aluminum matrix. While this coupling has been heavily investigated from an electrochemical perspective, it is of interest to investigate the mechanical driving mechanisms behind the galvanic corrosion process as well as the transition from pitting to cracking. Given the mesoscale size of the pit formation, the mechanical behavior of the microstructure must influence corrosion, in particular the heterogeneous residual strains and stresses developed when the material undergoes mechanical loading. Therefore, this research postulates that the evolution of corrosion and its transition to cracking is linked to the mechanical heterogeneity present in the material that may be fostering or delaying pitting. This work thus examines the following research questions:

- The effects that both the micromechanics and the local electrochemistry have on localized galvanic corrosion.
- The driving forces behind the various stages of corrosion up to its eventual transition to crack initiation.
- A fuller description of the material behavior at the constituent particles, which are known to be a source of pitting.
- The advantages, limitations, and considerations to make when using computer simulations to predict the behavior of a material under corrosion.

To better understand the relationship between galvanic corrosion, the local micromechanics, and the local electrochemistry, a series of material characterizations are performed over the same region of interest (ROI) on the surface of an AA7050-T7451 specimen. The microstructure morphology is characterized via electron backscatter diffraction (EBSD), the cathodic particles are located via energy dispersive x-ray spectroscopy (EDX), the residual strains are mapped via high resolution digital image correlation (DIC) of a speckle pattern captured before and after mechanical loading via Scanning Electron Microscopy (SEM), and the corrosion

evolution at the surface is measured via confocal laser scanning microscopy (CLSM). These characterizations not only allow for a quantitative analysis of corrosion evolution, but also give enough information to generate equivalent elasto viscoplastic computer models solvable via FFT-based formulations (EVP-FFT) that will help complete the description of the micromechanical fields by obtaining the stresses present in the material.

To further investigate the transition from corrosion to cracking, 3D EVP-FFT computer simulations of different corroded morphologies are reconstructed from x-ray computer tomography (XCT) scans alongside EBSD scans, in an effort to understand why initial cracking does not necessarily occur at the deepest pit. The simulations indicate that crack initiation from environmentally damaged materials can be reasonably predicted with the fatigue indicator parameters calculated from the simulated stresses and strains. In this work an analysis of the driving mechanisms behind crack initiation on environmentally degraded AA7050 is performed.

The work presented in this document led to the following research contributions:

- The ability to identify and predict strain localization based on an anisotropic grain structure.
- Improved strain field predictions based on probabilistic sub-surface reconstructions of the characterized surface microstructure.
- The verification that strain localization is not a sufficient criterion for the development of galvanic corrosion.
- The identification of a correlation between high stress concentration and galvanic corrosion under the presence of a cathodic particle.
- The verification of the ability to predict crack initiation from microstructural attributes, as well as the corrosion morphology. Further, the leading mechanisms behind pit-to-crack transition in corrosion fatigued materials were identified.

The full study of the galvanic corrosion mechanisms on AA7050 will aid in the development of tools that can accurately predict the life of a part servicing under a corrosive environment given the morphological, chemical, and microstructural characterization of the material.

2. LITERATURE REVIEW

Corrosion in aging aircraft and infrastructure is currently a 20-billion-dollar problem [1], due to the increased maintenance hours needed to preserve flight safety in fleets exposed to harsh environmental conditions. A teardown analysis of aerospace components has shown that corrosion features initiate roughly 80% of observed fatigue cracks [2]. Since there is not a clear understanding of the mechanisms driving the transition from corrosion damage to crack initiation, the current maintenance and repair protocols are largely focused on the outright removal of corrosion upon discovery [3]. This approach has been shown to be cost inefficient, incapable of properly removing complex corrosion morphologies, and detrimental to the overall service life of components [2][3], due the higher stresses arising from generalized thinning in the material.

Corrosion studies are usually limited to exploring one mechanism at a time, with most research focusing solely on either the mechanical or the chemical behavior of the material, while seldom studying their joint interaction even when both mechanisms are known to heavily affect corrosion during its early stages. To bridge the gap between the mechanical and the chemical studies of corrosion evolution up to its transition to crack initiation, this work investigates corrosion mediated failure in aluminum alloys by performing joint analyses of the various mechanisms driving the early stages of corrosion as well as its transition to cracking across the same region of interest using multimodal characterization techniques.

2.1 Corrosion growth and its transition to cracking

For AA7050, crack initiation occurs at features as small as ~ 50 μm [4], therefore it is important to study corrosion during its early stages before it reaches a critical size. Some factors affecting corrosion are either mechanical due to their role as stress/strain concentrators, such as surface roughness [5] or grain boundary density [6], or electrochemical, such as local Volta potential gradients [7], compositional heterogeneities, and the electrochemistry between particles [8]. From a mechanical perspective, the residual loads affect the corrosion behavior as they either encourage pit growth [9] or retardation [10]. However, most studies relating mechanical deformation with localized corrosion only measure the response of the material at the macroscale

level [11][12], and the few cases studying localized deformation use x-ray for zones of ~4 μm [13], or electron microscopy for zones under ~ 1 μm [14], both of which yield very limited fields of view, especially relative to cathodic particles with a diameter of ~10 μm [15].

The geometry of the corrosion pit has been consistently analyzed in an effort to locate any possible crack initiation predictors. From a purely geometric point of view the equivalent initial flaw size approach (EIFS) [16] has proven useful at studying the transition from corrosion pitting to cracking for heavily corroded materials with pits in the order of hundreds of microns. However, the EIFS approach is not reliable for pits at the mesoscale given the lack of information on the microstructurally small crack behavior [17]. This is further confirmed by geometric studies of the corrosion morphology at the mesoscale have showing that the transition from pitting to cracking does not necessarily occur at the deepest pit, indicating a strong influence from the local microstructure. Even though the corrosion depth does not translate into a crack nucleation predictor [4], it has been established that corrosion pits greater than 20 μm – 70 μm have a higher probability of evolving into a crack [4][18]. Therefore, it is important to understand the mechanisms behind the initiation and growth of corrosion pits at the micrometer scale, i.e. at the mesoscale level, before they reach that limiting depth.

2.2 Electrochemical approach

Several studies have shown that the difference in potential between the intermetallic particles and its surrounding matrix fosters localized corrosion [19], with the initiation and growth of pitting corrosion being largely affected by this electrochemical interaction [19][20]. It has been observed that, when the intermetallic particles are anodic relative to the matrix, they dissolve and leave a cavity in their place. When the particles are cathodic, they dissolve the surrounding matrix thus causing trenching attack morphologies that transform into a pit when particle fallout occurs.

For the case of AA7050-T7451, the particles that account for most of the localized corrosion initiation at the mesoscale level are the iron-based Al_7Cu_2Fe particles, which are cathodic relative to the surrounding matrix [20][21] and have diameters ranging from 1-40 μm [22][23]. It should be noted that fatigue crack initiation for non-corroded samples also happens to occur at large particles on the mesoscale level since they act as defects [24], so this specific cathodic particle is

of particular interest from both and electrochemical and mechanical perspective. Not only are these particles pit initiation points, but also they are responsible for corrosion damage accumulation since they tend to cluster along the rolling direction of the material [25]. This means that the electrochemical corrosion of these particles nucleate several smaller pits that inevitably coalesce into a bigger pit along the rolling direction, which is the reason that the Transverse Short (TS) direction of rolled AA7050 consistently shows deeper corrosion pits compared to any other direction. This coalescence develops deeper and wider pits that eventually transition into a life limiting crack [26] that ultimately shortens the residual life of a component [27]. Some other works have studied the surface increase of pitting as a factor relying of increased chemical potentials, due to the surface tension inside the ellipsoidal pit [28], however, these studies are limited by oversimplified 2D analyses of a corrosion geometry that is actually tortuous in nature.

2.3 Mechanical approach

Strain localization is a precursor to material failure that ultimately compromises the structural integrity of a component or an entire system. When a material is loaded, the strain is accommodated via discrete slip bands, which leads to heterogeneous deformation. The slip bands intensify during cyclic loading, thus potentially leading to fatigue crack initiation [29]. Similarly, the role of preexisting stresses on corrosion has been studied macroscopically, either concentrating on the instability of the exposed flat surface [30], the change in surface diffusivity [31], the changes in the pitting potential [32] and the overall electrochemistry [33]. Additionally, any prior active loading may have damaged the protective passive film and increased the susceptibility of the material to corrosion. Most notably, it was found that stresses only amplify the corrosion current and do not change the shape of the electrochemical potential and that the changes in surface texture have varying results in the overall corrosion of the material, especially when taking into account localized corrosion product accumulation [32][34]. Additionally, macroscopic plastic deformation has been shown in the literature to both increase and decrease the susceptibility to corrosion [35].

The study of corrosion pitting evolution to cracking, however, has been limited to the study of its corrosion morphology at a macroscale level. That is, individual specimens are usually mechanically studied as a macroscopic notch [36], where a homogenous material is usually assumed. Given the fact that the transition from pitting to cracking occurs on the magnitude of

tenths of microns [4], the material cannot be considered to be homogenous since the aforementioned characteristic length is akin to crossing several grains with varying orientations. Therefore, it is necessary to study the acting variables affecting pit growth at a sub grain level, which includes the heterogeneity of strains, stresses, the microstructure and the local electrochemistry.

The microstructure has been the focus of many studies within the corrosion community, mostly qualitatively via electron microscopy and sometimes quantitatively via electron backscatter diffraction (EBSD) analysis. Some studies even use the EBSD scans themselves to calculate the level of misorientation (MO) within the grains themselves, in an effort to pinpoint the effect that defect densities have on corrosion [37], with the constraint of requiring highly accurate HR-EBSD scans to properly capture the dislocations occurring in the material. This methodology is also limited to capturing geometrically necessary dislocation activity, which is only a partial representation of the complex deformation mechanisms on polycrystalline materials. From a mechanical perspective the role of the grain boundaries (GBs) has been of particular interest, as distinct GBs are prone to pit formation and associated environmental-assisted crack propagation [38]. Similarly, the grain sizes in a corroding material tend to be studied as they indirectly measure grain boundary densities and their effect on corrosion [39]. Grain boundary densities can either increase corrosion resistance by increasing the surface area that in turn creates a larger and more resistant oxide film, or decrease the corrosion resistance for situations where the passive film is not formed, therefore increasing the surface reactivity from the larger surface area exposed to a corrosive environment. In either case, grain boundaries are consistently shown to affect corrosion by degrading the grains [40], particularly under stress conditions, and thus are of interest to be studied before the corrosion process evolves into a crack.

Most corrosion studies prior to crack nucleation are typically qualitative and emphasize the effects that both the microstructure and the mechanical work have on the protective passive layer at the surface of the material. The degree of protection that this passive layer has on the material has been studied both mechanically and electrochemically, either by identifying how the mechanical work physically breaks or compresses the passive layer, or by analyzing the role of the accumulation of internal tensile stresses, which increases the potential at the surface, thickens the

passive layer, and ultimately increases the level of protection at the surface [41]. However, since the increase of potential from residual stresses is magnitudes smaller than the change of potential arising from the presence of cathodic particles, the nanometer scale increase of thickness from the residual stresses is outweighed by the local presence of the cathodic particles, which break down the passive layer given the local depletion of the potential [42]. Once the passive layer is broken the local electrochemical attack on the matrix rapidly follows.

When studying the residual strains across length-scales (e.g. Type I - macroscale, Type II – grain-scale, and Type III – point scale), most of the available literatures on corroding material focuses on Type I, and, with the exception of some Type II studies of single line scan strains across shear bands [13], the effects of the Types II + III localized mechanical behavior on corrosion have been rarely studied. This is largely due to the difficulty of characterizing Type II + III residual strains/stresses at high resolution over large regions of interest (ROI) for mesoscale analysis.

2.4 Obtaining the mechanical behavior

There have been recent developments in the materials community, in which full-field strain maps have been characterized experimentally and the same ROI is used to instantiate computational modeling efforts. For the first scenario, the tracking of high-resolution patterns before and after deformation on the surface [43] lead to experimentally acquired deformation values that can be used to calculate the local strains in the material. For the second scenario, mathematical models have been developed into virtual instances of the microstructure to obtain the mechanical response of a given microstructure via constitutive relationships of the flow rule and hardening behavior that govern the plastic response of the material.

2.4.1 Experimental techniques

To understand the underpinning physics behind strain localization, the scientific community usually relies on experimental measurements of strain, for which digital image correlation (DIC) has proved to be a good method for full-field surface displacements. DIC is a powerful technique for mapping deformation relative to the material's surface [44] and can be extended to characterize strain relative to microstructural features [45][43]. The DIC analysis requires the material surface to be patterned with features that can be tracked at the desired scale. Some of the patterning

techniques include functionalized particle speckling [46][47], in which the surface is evenly patterned with nanoparticles that are chemically bonded onto the surface, or mechanical ones such as microstamping [48], in which a flexible transparent material is added on top of the surface and patterned via a stamping technique. These procedures can accurately depict strain localization for high-resolution DIC maps.

2.4.2 Computational techniques

The use of computer models has also shown potential for obtaining the strain heterogeneity at the microstructural level. Obtaining microstructural strains via simulations is appealing, because it is relatively inexpensive, fast and provides the opportunity to understand how specific parameters affect the overall performance of the material. This is in contrast with experimental results that require a varied array of mechanical equipment, training, and specimen preparation. By incorporating micromechanical features within simulations, such as the grain orientations and morphologies and the constitutive laws governing the material behavior, more accurate descriptions of localized plastic flow can be obtained [49]. Crystal Plasticity – Finite Element (CPFE) modeling is a technique dating from the early 90's [50] that is capable of obtaining the micromechanical fields arising from the microstructural features by solving for crystalline slip activity in a continuum framework [51].

One of the earliest works where the experimentally acquired grain orientations of a specimen were used to instantiate a model was done by Becker [52]. In his work the grain orientations measured by electron backscatter diffraction (EBSD) were input into a 2D crystal plasticity finite element method (CPFEM) polycrystalline model and subjected to uniaxial loading, which was shown to generate a non-uniform strain field despite the uniformity of the macroscopic applied strain. Moreover, a 3D CPFEM polycrystalline model was presented by Beaudoin et al. [53], for which the orientation distribution function was obtained via x-ray diffraction, and parallel processing was used to efficiently simulate the full non-uniform deformation of the 3D model. As a result, there has been an interest in using CPFEM models for aspects of component analysis [54] that can account for the crystallographic orientations and thus improve their ability to predict deformation. The challenge remains in maintaining the fidelity of the predicted strain fields while keeping the size of the CPFEM model within reasonable computing times.

The elasto-viscoplastic fast Fourier transform (EVP-FFT) formulation [55] is an efficient alternative to CPFEM, as it is capable of calculating the internal strains of a loaded microstructure, based on an iterative method [56] that solves the governing equations in Fourier space, thus transforming a convolution problem into a point-wise multiplication operation that can be solved in a shorter time. Another benefit is that unlike CPFEM, EVP-FFT is performed on a voxelized grid, thus circumventing the need to create a discretized mesh. One potential drawback of the EVP-FFT method is that it is restricted to periodic structures and therefore limits the types of geometries that can be analyzed [57]. The EVP-FFT technique has been consistently shown to give the same results as CPFE when both analyzing the full micromechanical fields in the material [57] and the local fields at regions with high stress concentrations such as crack tips [58].

2.4.3 Limitations

Any method, however, has shown to encounter issues with obtaining a full representation of the microstructural behavior, especially when there is only surface data available. As seen by Turner et al. [52], the neighboring microstructure of an analyzed surface strongly affects its strain field. Therefore, unless the uncertainty of the surrounding microstructure is minimized, the accuracy of a simulated strain field will remain unknown. Studies of equiaxed polycrystals have shown that accounting for the subsurface microstructure improves the predictive capabilities of computer models, since the through-thickness grain assumption tends to over-constrain the deformation of grains [59]. Two recent studies have reconstructed subsurface grains via differential-aperture X-ray microscopy [60] or by tessellating grains at the subsurface [61]; the consensus of these studies is that a subsurface two to three grains deep is sufficient to account for the subsurface constraints imposed on the surface. However, these studies are limited to equiaxed polycrystals and have not accounted for the subsurface uncertainty for rolled materials with elongated grains, which are usually assumed to be perfectly elongated in computer simulations.

The influence of the subsurface uncertainty on the strain distributions has seldom been validated with experimentally observed distributions for the same region of interest (ROI).

One approach for reducing the subsurface uncertainty of the simulation involves the use of oligocrystal specimens. These specimens exhibit relatively large grains compared to the thickness of the sample, such that the effect of the subsurface microstructure has on the surface is mitigated

by its distance from the free surface [62]. Therefore, a better match between CPFEM simulations and real material features is observed [63]. The predictive capabilities of oligocrystal CPFEM models is further explored by Lim et al. [64] by studying the effects that meshing, slip plane activity, and crystal orientation have in predicting the failure location of a specimen subjected to large plastic strains. Another approach for improving the modeling of highly anisotropic materials with limited information is by generating 3D statistically equivalent virtual microstructures, where the statistics necessary to instantiate the virtual microstructure can be directly obtained from surface characterizations. 3D virtual reconstructions, which contain more realistic grain morphologies than those generated from tessellation, have been used to statistically study the micromechanics in anisotropic materials without the need of destructive characterizations [65], and therefore show promise in improving the performance of micromechanical models with subsurface uncertainty.

2.5 Predicting corrosion cracking

The mechanisms behind crack initiation on pristine materials has been thoroughly studied by the community both from an experimental and a computational perspective; for a detailed review, please refer to [29]. As earlier as 1903, Ewing and Humfrey concluded that fatigue crack initiation is mediated from a slip-based damage mechanism [66]. Experimental studies have shown that microstructural variables, such as the grain sizes [67] or types of grain boundaries [43][68] affect the dislocation activity and subsequently the onset of crack initiation. Engineering alloys are tailored with complicated microstructures, in which a collection of attributes determine the crack initiation event. Computational mechanics models allow the analysis of competing mechanisms that would be difficult to isolate experimentally, and have been used to address crack initiation stemming from rank order based on microstructure ensembles [69], as large as grains in Ni-based superalloys [70], rogue grain combinations in Ti alloys [71], and critical pore size in additive manufacturing [72], to name a few. In each of these models, the heterogeneous deformation around microstructural attributes leading to strain accumulation results in the crack initiation event. Each of these fatigue crack initiation studies have demonstrated the prognosis capabilities towards the concept of a digital twin; yet the number of papers that predict fatigue crack initiation from the microstructural attributes in a corroded environment are scarce.

The study of pit-to-crack transition has been mostly studied via continuum mechanics, where the existing pits are modeled as pre-existing cracks [73] that need to surpass other competing mechanisms, such as pit growth rate, for crack initiation to occur. Most of these analyses are constrained to a 2D study of the corrosion geometry that oversimplifies the corrosion tortuosity, and the few mechanical studies of 3D corrosion morphologies only analyze single pits with an ellipsoidal geometry [74]. Since the mechanical study of corrosion is limited by the characterization and modeling of corrosion over large surfaces, the pit-to-crack transition is often studied via statistics where the distributions of the size and geometry present in the material are obtained from the characterization of a much smaller region [75].

One of the largest limitations of the current pit-to-crack studies is the size of the pits that can be evaluated with these type of methods. While the continuum mechanics approach from the current methods is suitable for the large corrosion pits usually found during maintenance, smaller pits in the order of tens of microns have been observed to nucleate cracking [27], with the life limiting corrosion features being capable to be as small as 20 μm deep [18], thus the initiation point for fatigue will not necessarily occur at the largest or deepest observable pit. Since cracking forms at a very localized region within the pit instead of at the periphery of the corrosion damage, at this length scale we need to account for the microstructural mechanisms fostering damage, namely the slip activity active in the material that is known to affect cracking in pristine materials [76], since the study of the geometry alone is insufficient [26]. In other words, pit-to-crack transition requires a joint analysis of the irregular pit geometry, the microstructure in the material, and any constituent particles that may affect the micromechanics leading to crack nucleation [77][78].

To study pit-to-crack transition at the micrometer length scale, there is a need to perform high-resolution characterizations of the material over a large area such that a reasonable number of pits are properly captured. X-ray computer tomography (XCT) [79] is capable of capturing the full tortuosity of corrosion [74] as well as the shapes and location of the Al_7Cu_2Fe particles [80] over regions spanning millimeters with resolutions up to half a micrometer. The higher resolution of XCT characterization allows to spatially locate cracking, both its initiation and growth, within the 3D corroded morphology [81], which gives it a great advantage over the traditional surface

roughness characterizations, for which the location of crack initiation is not a straightforward process.

The characterizations from XCT can be directly used as input in computer models [82] that can yield the micromechanical fields present in the material. These micromechanical fields, in turn, can be used to compute well known crack initiation metrics that are based on localized slip activity [83]. These crack initiation metrics, commonly known as Fatigue Indicator Parameters (FIP), are able to reflect the driving forces behind crack formation for a wide array of loading conditions and for different types of microstructures [84]. Most importantly, FIPs are a good metric for crack nucleation in models where the micromechanics are affected by additional microstructural features such as constituent particles [85]. Therefore, the onset of crack nucleation can be analyzed quantitatively given a holistic approach that accounts for the multiple variables behind failure in environmentally damaged materials.

3. METHODS

3.1 Material

The 7000x series of aluminum alloys, notably AA7050-T7451, is commonly used in high performance components that require high strength and durability, and as such is commonly found in aerospace applications, particularly in airframes where high tension and compressive loads are present. Under these loading conditions not only is the material required to be nominally strong, but also to remain reliable during the projected life cycle of the component, including its exposure to environmental degradation. Even though AA7050-T7451 is one of the most corrosion resistant aluminum alloys, its life is conditioned by corrosion pitting that develops on saline environments, as pits are the main source of cracks. As such, there is an invested interest in studying the mechanisms behind corrosion growth and cracking for one of the strongest, lightest, and most used materials used in the aerospace industry. In the present work, a commercial plate of a rolled aluminum alloy AA7050-T7451, was used to machine all specimens studied, thus leading to the study of a highly anisotropic microstructure.

It should be noted that AA7050-T7451 exhibits a local electrochemical behavior arising from secondary phase particles, such as Al_7Cu_2Fe, Mg_2Si, Al_2CuMg, AlCuFeMnSi or $MgZn_2$. At the mesoscale level, the particles present in the material are the cathodic Al_7Cu_2Fe particles and the anodic Mg_2Si particles. Since the Mg_2Si particles are known to have a lower volume content in AA7050-T7451, the main focus of the local electrochemical studies will focus on the cathodic Al_7Cu_2Fe particle.

3.2 Surface Topology Characterization

To ensure a high resolution characterization of the surface roughness generated from corrosion, Confocal Laser Surface Microscopy (CLSM) was used, a technique that allows the 3D characterization of surfaces from a grayscale stack of confocal images spaced evenly in the z direction. To minimize noise and maximize signal intensity, the pinhole size needs to be reduced such that it only captures the first dark ring of the diffraction pattern surrounding the laser point, in order to block any light that was out of focus. This is controlled by setting a capture radius of 1

Airy Unit (AU), with an Airy Unit defined as the distance from the center of the major light intensity peak to the first minimum. The ROI can be segmented into areas if a larger area needs to be analyzed. The first and last slices on the grayscale z-stacked images is manually determined by checking the highest and lowest points captured by the grayscale intensities in the ROI.

For the work presented in this document, CLSM was performed using a Zeiss LSM 880 upright Confocal Microscope with a 561 nm laser wavelength, a Plan Apochromatic 10x/0.45 objective, a step size of 1 μm in the z-direction, and a resolution of 0.10 μm in the x-y directions. A high resolution was achieved by using a slow dwell time of 2 μsec/pixel during scanning, which also meant that the characterization of the ROI was sufficient to quantify the corrosion around the particles. Finally, to maximize the grayscale gradient of the confocal images, the laser was set to 25% intensity, with an optical gain of 633, a digital offset of 0, and a digital gain of 1.

A MATLAB code was developed to reconstruct the surface from the grayscale stacked images, where the topographic height was calculated based on a procedure proposed by [86] with the main **Eq. 3.1** being:

$$h(x_i, y_j) = dz \frac{\sum_{z_k \in FWHM} I(x_i, y_j, z_k) z_k}{\sum_{z_k \in FWHM} I(x_i, y_j, z_k)} \tag{3.1}$$

where $h(x_i, y_j)$ is the topographic height, $I(x_i, y_j, z_k)$ is the image intensity for each pixel, dz is the step size on z, z_k is the stack number, and $FWHM$ is the full width at half maximum (the width of the Gaussian distribution of $I(x_i, y_j, z_k)$ at $0.5I_{max}$). To account for global surface evolution the profiles were offset such that the tallest feature on Day 01 became the zero-reference point and the subsequent corrosion profiles were offset by Δh_{n+1} between Day n and Day n+1, such that:

$$\Delta h_{n+1} = \langle \max(h_n) - \max(h_{n+1}) \rangle + \langle \overline{h_{n+1}} - \overline{h_n} \rangle \tag{3.2}$$

for which $\langle \cdot \rangle$ are the Macaulay brackets, (i.e. $\langle x \rangle = x$ if $x > 0$, and 0 otherwise). The first half of **Eq. 3.2** ensures that the evolution of the deepest features either keeps growing deeper or remains the same. The second half of **Eq. 3.2** ensures the proper description of surface recession where

material addition is not possible. Finally, to account for variations in flatness the slope of the surface was calculated and removed from the reconstructed maps.

3.3 Microstructural Characterization

Electron backscatter diffraction (EBSD) is a material characterization technique capable of capturing individual grain orientations, local texture, spatial orientation correlations, and the phases present in the material. To achieve the mirror-like surface necessary for EBSD characterization, the surface of each specimen needs to be incrementally ground from a 400 grit sandpaper (21.8 μm particle diameter) down to a 1200 grit sandpaper (2.5 μm particle diameter), to remove any machining marks such that no significant scratches could be observed at a magnification of 10x. Afterwards it needs to be gently polished in a series of short 30s exposures to a NAPPAD cloth with distilled water and various suspensions from 15 μm alumina down to a 0.05 μm colloidal silica suspension. It should be noted that the final polishing with colloidal silica needs to be done during intervals to improve the kikuchi patterns while at the same time minimizing any surface deformation and preventing any particle fallout.

To remove any leftover silica on the surface, the specimens need to be cleaned with a fresh NAPPAD cloth containing only distilled water, with frequent rinsing of the cloth using fresh distilled water. To remove any other contaminants, each specimen needs to be sonicated with a Sper Scientific ultrasonic cleaner using isopropyl alcohol, acetone, and methanol (in that order). For each cleaning agent, the specimen can be sonicating for 360 s, after which it has to be taken out, rinsed with a fresh batch of the cleaning agent, and dried with compressed air. Extreme care needs to be taken to not touch the specimen with bare hands or dirty utensils. SEM scanning can be performed prior to EBSD scanning for a final evaluation of the surface quality.

All EBSD scans of AA7050 on the present document are performed using a 25 kV accelerating voltage, a spot size of 5, 21 mm working distance, 500x magnification, and a 70-degree tilt. The EBSD setup used a gain of 14.08, a black level of 3.86, 82.55 ms exposure time, and a step size of 1.50 μm. Afterwards, the built-in EDAX OIM Analysis software was used to perform noise cleanup of the raw orientation datasets via a 2-pixel step erosion-dilation process and removal of bad data points, where a point is considered to be bad if its confidence index is below 0.1 and its

angle relative to its neighbors surpasses 5°. This bad data removal also removes any orientations scanned at the cathodic particles and replaces them with the surrounding matrix orientation, especially since the particles usually cover a couple of voxels and they tend to contain noise around them on the EBSD scans. Finally, each orientation file is processed via the MTEX toolbox [87] for additional analysis of the orientation data.

3.4 Particle Characterization

Energy Dispersive X-ray Spectroscopy (EDS) it a chemical characterization technique capable of locating spatially the distribution and location of the different elements present in the material. This technique stimulates the emission of characteristic x-rays that can be measured by an energy dispersive spectroscoper and subsequently can pinpoint spatially the elemental composition in the material. In the present work EDS is used to characterize the constituent particles present in AA7050-T7451, namely the cathodic particle Al_7Cu_2Fe which is highlighted in EDS by spatially pinpointing the copper-rich and iron-rich zones of the material. All EDS scans are performed using a FEI Quanta 3D FEG Dual-beam SEM with 30 kV accelerating voltage, spot size of 4, 10 mm working distance, 700x magnification, and 0.4 μm/pixel resolution able to spatially particles. It should be noted that the Mg_2Si anodic constituent particles present in AA7050-T7451 can be also located via EDS but, given their lower content on AA7050 and their smaller size, no anodic particles were found on the ROIs studied and therefore were out of the scope of this document.

3.5 Strain Characterization

Digital Image Correlation is a nondestructive technique capable of characterizing strain in materials by tracking a pattern placed at the surface of the material before after deformation occurs. For DIC surface strain characterization, the substrate must be patterned with features that will allow strain measurements at the desired resolution. To obtain high-resolution strain maps necessary to capture the intragranular strain localization, the surface needs to be patterned with either microstamping techniques or via placement nanoparticles such as the ones developed by titanium or gold suspensions [88], particularly if it is of interest to resolve the strain around the Al_7Cu_2Fe particles. For a proper characterization of the surface, the speckling needs to be

homogeneous throughout the ROI, which can be verified via a SEM scanning of the surface prior to testing. To perform DIC, the nanoparticle speckling at the surface is imaged ex-situ via SEM before and after the specimen experiences loading. Afterwards, DIC can performed on each pair of undeformed/deformed images using VIC-2D [44], resulting in a full map of in-plane strains at the surface.

Finally, to remove any potential distortions of the strain fields due to electromagnetism present during acquisition of the SEM images, the DIC strain maps need to corrected following a distortion correction protocol developed in house and described in [89], in which a certified grid is scanned alongside with the specimen during every SEM image acquisition. By fitting a response surface on the quantified distortion of the grid, the inherent spatial distortion and magnification uncertainty can be identified and removed from the raw strain maps from DIC. This results in more reliable strain field mapping with an uncertainty kept below 0.1% strain. The final corrected strain field maps can be then used for micromechanical analysis of the material.

3.6 Crystal Plasticity Simulations

To fully understand the mechanisms that drive localized corrosion, a more complete description of the micromechanical state relative to the microstructure is needed, as the strains alone are not a definite indicator of the regions that are prone to pitting corrosion. Therefore, it is necessary to also obtain the stress distributions in the material. To characterize the grain-level stresses, an analogous crystal plasticity computer model of the microstructure is necessary, such that, once macroscopically calibrated to the average specimen response and microscopically validated to the experimental strain observations, can be used to obtain the full stress distribution.

To obtain a complete mechanical description of the material studied at the mesoscale, An EVP-FFT formulation was used to model the behavior of FCC polycrystals under uniaxial loading [55] based on the original formulation by Moulinec and Suquet [56]. This formulation relates the viscoplastic strain rate $\dot{\varepsilon}^{pl}$ with the stress $\sigma(x)$ at a single crystal material point x as:

$$\dot{\varepsilon}^{pl}(x,\sigma) = \dot{\gamma}_0 \sum_{\alpha=1}^{N} M^{\alpha}(x) \left(\frac{|M^{\alpha}(x):\sigma(x)|}{\tau_0^{\alpha}(x)}\right)^{n} sgn(M^{\alpha}(x):\sigma(x)) \tag{3.3}$$

where $\dot{\gamma}_0$ is the reference shear rate, $\tau_0^\alpha(x)$ is the Critical Resolved Shear Stress (CRSS), which gets incrementally updated due to strain-hardening, n is the stress exponent, M^α is the Schmid Tensor, and N is the total number of active slip systems with each slip system denoted with an index of α. Using an Euler implicit time discretization scheme and Hooke's law, the stress in material point x and time $t + \Delta t$ becomes:

$$\sigma(x) = C(x) : \varepsilon^{el}(x) \tag{3.4}$$

where:

$$\varepsilon^{el}(x) = \varepsilon(x) - \varepsilon^{pl,t}(x) - \dot{\varepsilon}^{pl}(x,\sigma)\Delta t \tag{3.5}$$

with the supraindex t indicating field values evaluated at time t. Here $\sigma(x)$ is the Cauchy stress tensor, $C(x)$ is the elastic stiffness tensor; $\varepsilon(x)$, $\varepsilon^{el}(x)$, $\varepsilon^{pl}(x)$ are the total, elastic and plastic strain tensors, and $\dot{\varepsilon}^{pl}(x)$ is the plastic strain-rate tensor given by Eq. (1). The inverse relation of Eq. (3) becomes:

$$\varepsilon(x,\sigma) = C^{-1}(x) : \sigma(x) + \varepsilon^{pl,t}(x) + \dot{\varepsilon}^{pl}(x,\sigma)\Delta t \tag{3.6}$$

Separately, the stress tensor can be rewritten by adding and subtracting the reference medium stiffness C^o_{ijkl} multiplied by the the displacement gradient tensor $u_{k,l}(x)$ as:

$$\sigma_{ij}(x) = C^o_{ijkl}u_{k,l}(x) + \sigma_{ij}(x) - C^o_{ijkl}u_{k,l}(x) \tag{3.7}$$

Given the polarization field $\varphi_{ij}(x) = \sigma_{ij}(x) - C^o_{ijkl}\varepsilon_{kl}(x)$, Eq. (5) is rearranged as:

$$\sigma_{ij}(x) = C^o_{ijkl}u_{k,l}(x) + \varphi_{ij}(x) \tag{3.8}$$

where $\varepsilon_{k,l}(x) = (u_{kl}(x) + u_{kl}(x))/2$. Deriving Eq. (6) and adding equilibrium ($\sigma_{ij,j} = 0$):

$$C^{o}_{ijkl}u_{k,lj}(x) + \varphi_{ij,j}(x) = 0 \tag{3.9}$$

Gives a partial differential equation (PDE) that can be solved in a periodic unit cell under strain $E = \langle \varepsilon(x) \rangle$ via the Green's function method, such that the displacement gradient can then be obtained as a convolution in real space:

$$u_{k,l}(x) = \int_{R^3} G_{ki,jl}(x - x')\varphi_{ij,j}(x')dx' \tag{3.10}$$

where $G_{km}(x - x')$ is the Green's function associated with the displacement field $u_k(x)$. After integrating Eq.(8) by parts such that $\tilde{u}_{i,j}(x) = \int_{R^3} G_{ik,jl}(x - x')\varphi_{kl}(x')dx'$, the problem can be solved in the Fourier space as a product instead of an integral, thus shortening the computational time required for the simulation, i.e.

$$\hat{u}_{i,j}(x) = \hat{\Gamma}_{\text{ijkl}}(\xi)\hat{\varphi}_{kl}(\xi) \tag{3.11}$$

where the Green operator $\hat{\Gamma}_{\text{ijkl}}(\xi)$ is only a function of stiffness and frequency $\left(\hat{\Gamma}_{\text{ijkl}}(\xi) = -\xi_j\xi_l\left[C^{o}_{ijkl}\xi_j\xi_l\right]^{-1}\right)$. Therefore, the strain field becomes:

$$\varepsilon_{ij}(x) = E_{ij} + FT^{-1}(sym(\hat{\Gamma}_{\text{ijkl}}(\xi))\hat{\varphi}_{kl}(\xi)) \tag{3.12}$$

Where the symbol "^" indicates a Fourier transform and ξ is a frequency of Fourier space. This strain field (**Eq. 3.12**) is replaced in Eq. (**Eq. 3.6**) and solved at every point to obtain a new guess for the stresses, using an iterative process that seeks a compatible macroscopic strain and an equilibrated stress fields [57]. Also, this formulation allows the use of different microscopic hardening laws without changing the main algorithm. For modeling of AA7050 the Generalized Voce Hardening Law was used:

$$\tau(\Gamma) = \tau_o + (\tau_1 + \theta_1\Gamma)\left[1 - e^{-\frac{\Gamma\theta_0}{\tau_1}}\right] \tag{3.13}$$

where τ_0 and θ_0 are the initial yield stress and hardening rate, respectively, and τ_1 and θ_1 are the parameters that describe the asymptotic behavior of the material. For the elasto viscoplastic modeling of AA7050, these parameters were obtained given an initial guess from the macroscopic stress-strain curve that characterizes the material through the Taylor factor [90] and a final manual fitting. For all specimens modeled in this document, the AA7050 material is modeled with the parameters shown in **Table 3.1** and **Table 3.2**, where the Voce hardening parameters were obtained in **Chapter 4** from the stress strain curves of the TL-LT-TS specimens shown in **Fig 4.4**. For large EVP-FFT models, the parallelization method described in **Error! Reference source not found.** can be used to achieve convergence under reasonable computer times.

Table 3.1 Voce Hardening Parameters

τ_0	θ_0	τ_1	θ_1
135.8337	3061.5587	8.4697	167.586

Table 3.2 Elastic parameters for matrix and particles

AA7050 Matrix	**C_{11}**	**C_{12}**	**C_{44}**
	111.2	57.4	26.4
Al_7Cu_2Fe Particles	**Modulus E**		**Poisson μ**
	160.2		0.33

3.7 Crack Nucleation Metrics

Fatigue Indicator Parameters (FIPs) are metrics capable of capturing the onset of crack nucleation given the slip activity in the material. In the present work, eight different FIPs [85][92] were calculated from the micromechanical fields calculated from the EVP-FFT simulations. The first four parameters studied: Slip System (SS), Slip Plane (SP), Accumulated Slip (AS) and Opening Plane (OP), evaluate the maximum accumulated shear strain per slip system or plane; whereas the last four parameters: Slip System Energy Density (SSED), Slip Plane Energy Density (SPED), Accumulated Slip Energy Density (ASED) and Opening Plane Energy Density (OPED)

are the energetic counterparts for the first four parameters that represent the dissipated energy in the slip system or plane. These FIPs are described in **Eq. 3.14** to **Eq. 3.21** as:

$$SS = \max_{\alpha} |\Gamma^{\alpha}| \tag{3.14}$$

$$SP = \max_{p} \sum_{\alpha=1}^{N} \left|\Gamma_p^{\alpha}\right| \tag{3.15}$$

$$AS = \sum_{\alpha=1}^{N} |\Gamma^{\alpha}| \tag{3.16}$$

$$OP = \max_{p} \sum_{\alpha=1}^{N_s} \left|\Gamma_p^{\alpha}\right| \left(1 + k \frac{\langle \sigma_n^p \rangle}{\sigma_Y}\right) \tag{3.17}$$

$$SSED = \max_{\alpha} |\tau^{\alpha} \Gamma^{\alpha}| \tag{3.18}$$

$$SPED = \max_{p} \sum_{\alpha=1}^{N} \left|\tau_p^{\alpha} \Gamma_p^{\alpha}\right| \tag{3.19}$$

$$ASED = \sum_{\alpha=1}^{N} |\tau^{\alpha} \Gamma^{\alpha}| \tag{3.20}$$

$$OPED = \max_{p} \sum_{\alpha=1}^{N_s} \left|\tau_p^{\alpha} \Gamma_p^{\alpha}\right| \left(1 + k \frac{\langle \sigma_n^p \rangle}{\sigma_Y}\right) \tag{3.21}$$

Where τ is the resolved shear stress, Γ is the accumulated plastic shear strain, α is the slip system number, p is the index of each slip plane, N_s is the number of slip systems associated with a particular slip plane p, N is the total number of slip systems , k is a scaling factor set to 0.5 as seen in [93], $\langle \sigma_n^p \rangle$ is the opening stress normal to the slip plane p, σ_Y is the yield stress (460MPa), and $\langle \cdot \rangle$ are the Macaulay brackets where $\langle x \rangle = x$ if $x \geq 0$, and $\langle x \rangle = 0$ if $x < 0$.

4. EFFECT OF MICROSTRUCTURE ON STRAIN LOCALIZATION

4.1 Introduction

It is necessary to investigate the material deformation at the microscale level by means of experimental analyses and material modeling. To investigate polycrystalline deformation at this level, non-destructive techniques such as non-contact Digital Image Correlation – Electron Backscatter Diffraction (DIC-EBSD) are necessary to identify spatial maps of strain heterogeneity [1][94][43][95], using different patterning methodologies [96][88][97] that can resolve strain down to a slip level resolution. To model polycrystalline deformation, Elasto Viscoplastic – Fast Fourier Transform (EVP-FFT) simulations capable of yielding a micro-mechanical response from a macroscopic load are necessary. As seen by Zhao et al. [62] the micro-texture influences strain heterogeneity, being the subsurface microstructure a source of discrepancy between observations and predictions [52][98]. Thus, olygocrystals show a better match because of their lower subsurface uncertainty [63]. Therefore, it is of interest to investigate rolled Al7050 for different material orientations both via experiments and simulations.

4.2 Materials and Methods

4.2.1 Material

A plate of rolled AA7050-T7541 [99] was used to machine three specimens parallel to the rolling direction (L-T), perpendicular to the rolling direction and aligned with the long direction (T-L); and perpendicular to the rolling direction and aligned with the short direction (T-S), as shown in **Fig 4.1**. The geometry of the specimen was adapted from the ASTM E8 standard [100] taking into account the size of the surface to be analyzed.

The experimental work in this chapter was performed by Dr. Alberto Mello, and the EVP-FFT models were performed by the author. A complete description of this chapter can be found in: *A.W. Mello, A. Nicolas, R.A. Lebensohn, M.D. Sangid, Effect of microstructure on strain localization in a 7050 aluminum alloy: Comparison of experiments and modeling for various textures, Mater. Sci. Eng. A. 661 (2016) 187–197. doi:10.1016/j.msea.2016.03.012.*

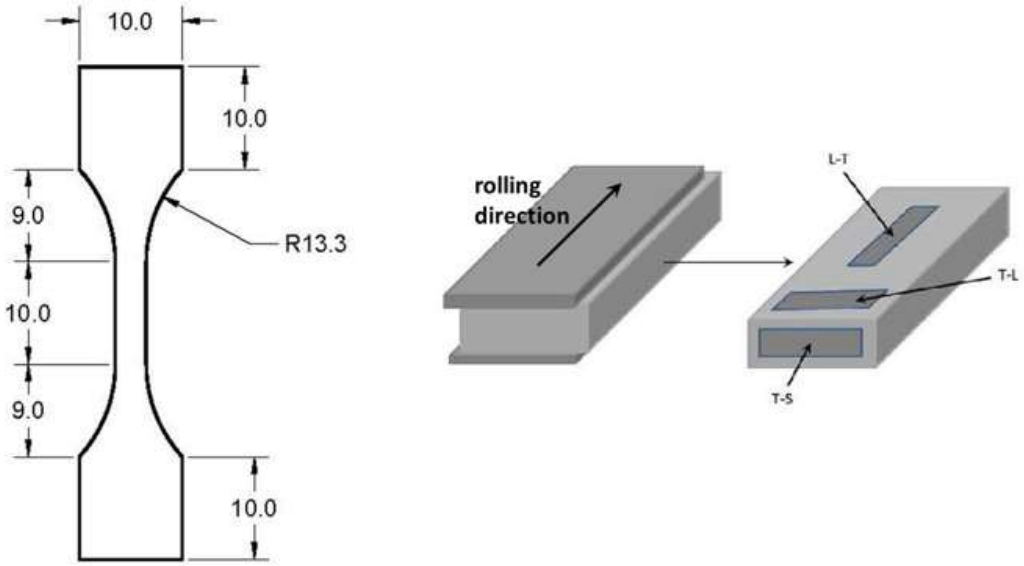

Fig 4.1 Specimen geometry and orientations from AA 7050-T7451 plate (dimensions in *mm*) with length of 48 *mm* and thickness of 1.6 *mm*.

4.2.2 Experimental Procedures

The specimens were polished using a 1200 grit sand paper followed by 0.05 μm blue colloidal silica until a mirror-like surface was obtained. Afterwards two 800 μm by 600 μm regions of interest (ROI) were delimited using fiducial markings [101] as depicted in **Fig 4.2** using a LECO Microhardness Tester LM247AT and forces of 1N and 0.5N for the bigger and smaller indents, respectively.

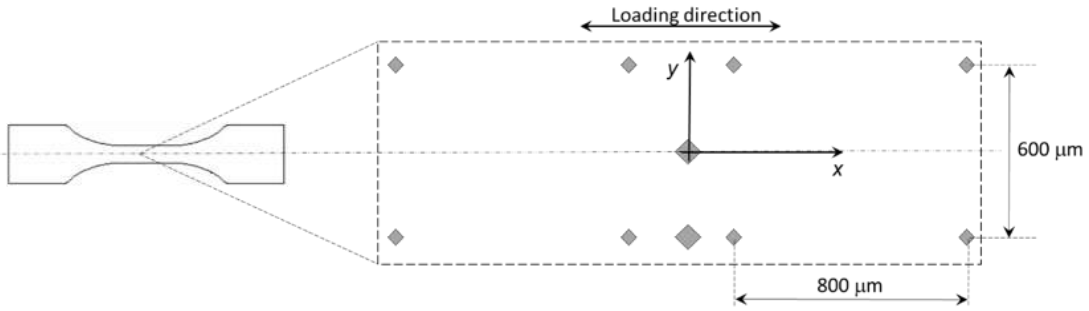

Fig 4.2 Delimited area for EBSD and DIC analysis.

EBSD characterization of the microstructure was performed, finding an average grain size of 80 μm and a range between 30 to 500 μm. A reusable micro stamp designed for DIC reference

patterning [102] was applied. The stamping process involves generating a master via lithography with a 10 μm base-element size speckle pattern and imprinting it into a castable material that polymerizes without shrinking nor bonding to the master [103], with the full protocol being described by Cannon et al. [48]. The resulting speckle pattern shown in **Fig 4.3** was used to stamp all AA 7050-T7451 specimens.

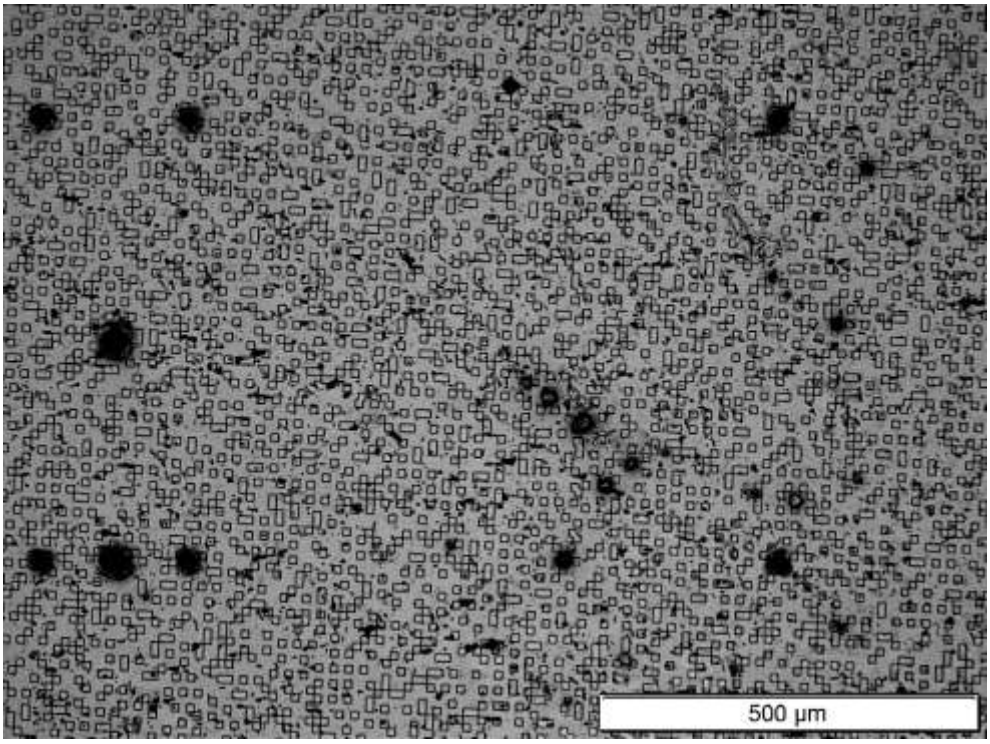

Fig 4.3 Area of interest viewed at *20x* in optical microscope, *10 μm* pattern

Six specimens, two for each direction (L-T, T-L, T-S), were loaded up to tensile rupture to determine mechanical properties from the stress-strain curves shown in Fig 4.4. All tension tests were performed in a 6.7 kN Mark-10 ESM-1500 Force Test Stand at a rate of 2 mm/min. A dedicated Epsilon extensometer Model 3542 was used to measure strain. The stress-strain results exhibit very similar mechanical properties in the three tested directions, with the final elongation being smaller for the L-T specimen due to the material plastic deformation in the longitudinal direction during the rolling process.

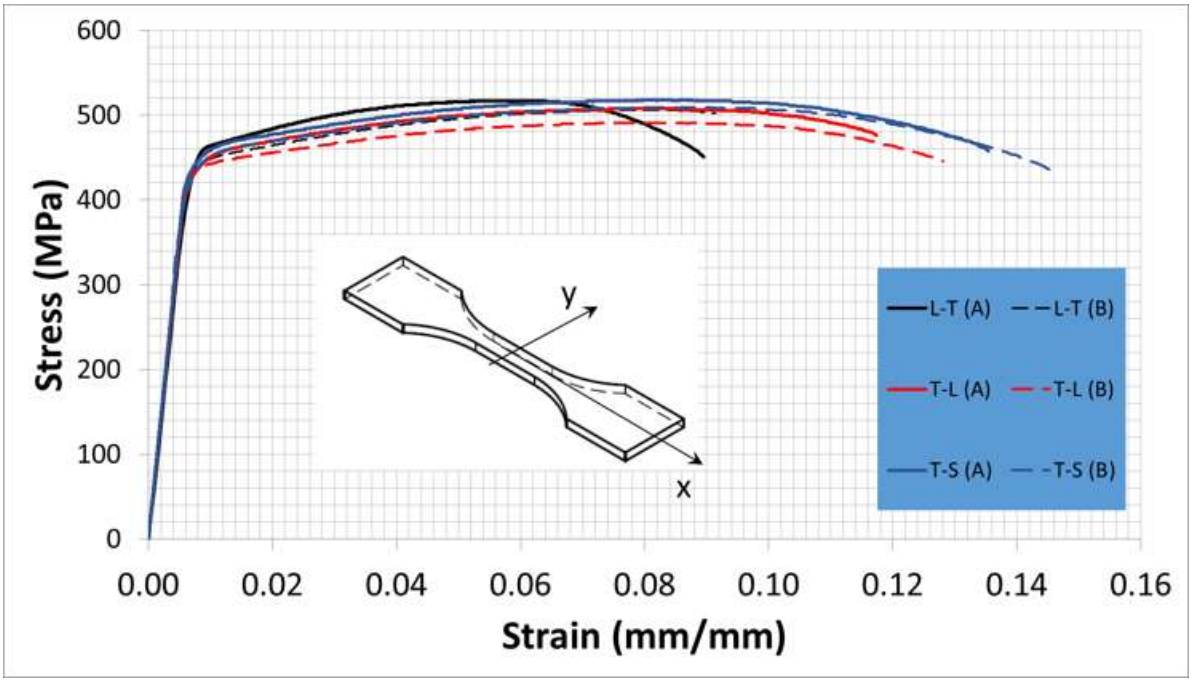

Fig 4.4 Stress-strain curves – AA 7050-T7451

4.3 Results

4.3.1 Experimental Strain Field Mapping

For a full-field strain measurement of the ROI, DIC [43][101][44] was performed using the stamping protocol described above, along with grain morphology characterization via EBSD seen on **Fig 4.5**. The average grain sizes for the L-T, T-L, and T-S specimens were 88, 79, and 59 μm, respectively, with the T-S specimen exhibiting smaller grains due to grain elongation being perpendicular to the plane. The Taylor factor was ~2.44 due to texture from rolling. Some constituent particles, possibly a combination of $MgZn_2$, AI_7Cu_2Fe, Al_2CuMg, and Mg_2Si [104], may have been identified as small grains on the EBSD scans on Fig. 5 due to their FCC crystal structure similarity to AA7050, but the Inverse Pole Figure (IPF) coloring do not represent their actual crystal orientation since their composition was not identified.

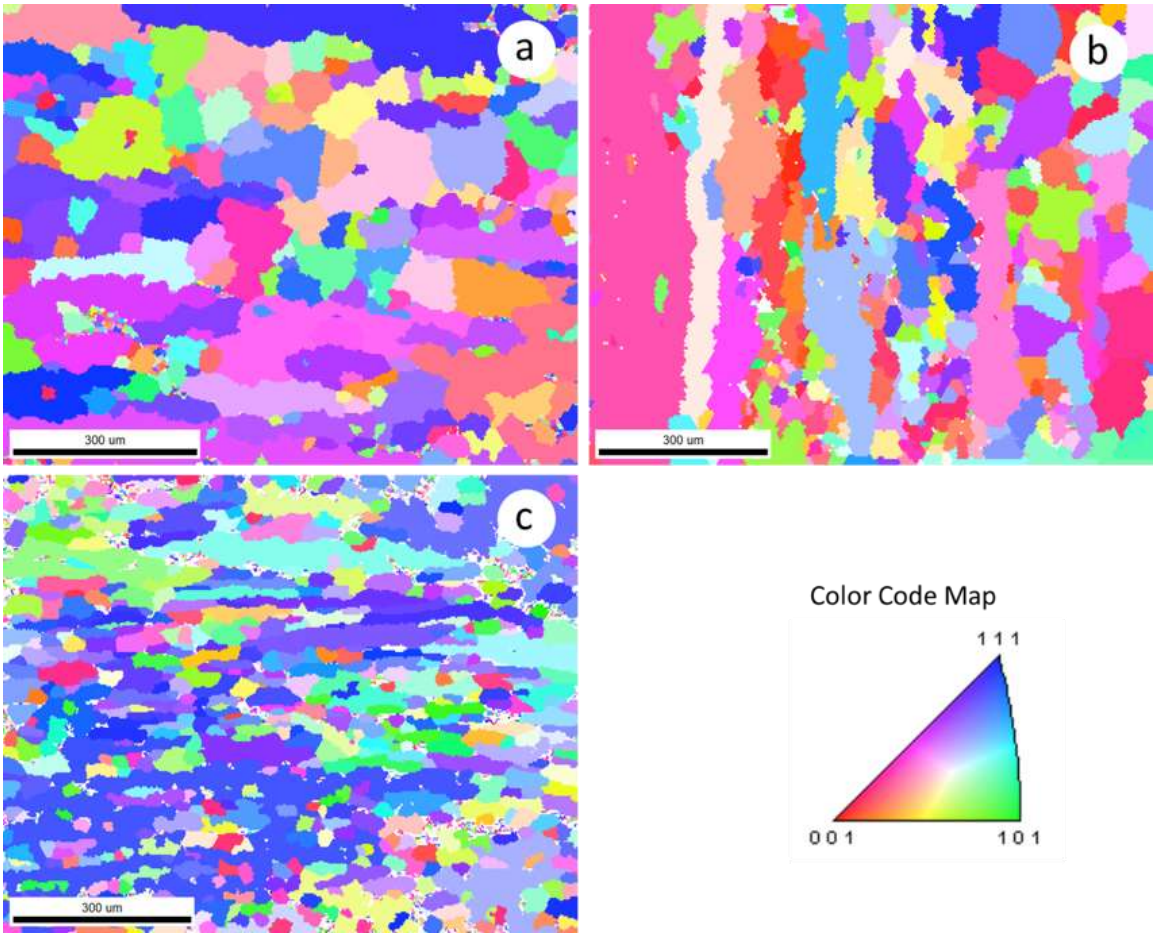

Fig 4.5 Inverse Pole Figure for: (a) L-T, (b) T-L, and (c) T-S.

All three specimens were loaded to 3% axial strain and unloaded to an unstressed condition. Vic-2D was used to perform DIC [44] for all specimens with a subset of 56 μm (about the size of the average grain) and a step of 3 μm. The localized residual strains are a result of strain accommodation due to crystal anisotropy, therefore the making overall mechanical response orientation dependent [105]. A sensitivity analysis on the subset size was performed to avoid strain dipoles [49][106].

For the L-T specimen the loading axial strain was 3.11%, reaching *427 MPa*. **Fig 4.6** shows the residual axial, transverse, and in-plane shear strain maps, ε_{xx}, ε_{yy}, and ε_{xx}, with the grain boundaries superimposed. For the T-L specimen the loading axial strain was 3.12%, reaching *489 MPa*, with **Fig 4.7** showing in-plane strains along with the grain boundaries colored according to the misalignment angle. Some isocurves are seen along low-angle grain boundaries (15º) on **Fig**

4.7a. For the T-S specimen the final total axial strain was 3.10%, reaching *488 MPa*. The strains are shown on **Fig 4.8** and exhibit the largest strain variations, possibly due to the need for a finer speckle size that can better resolve sub-grain strains. All maps show regions with a much higher strain than the average value that can facilitate crack nucleation.

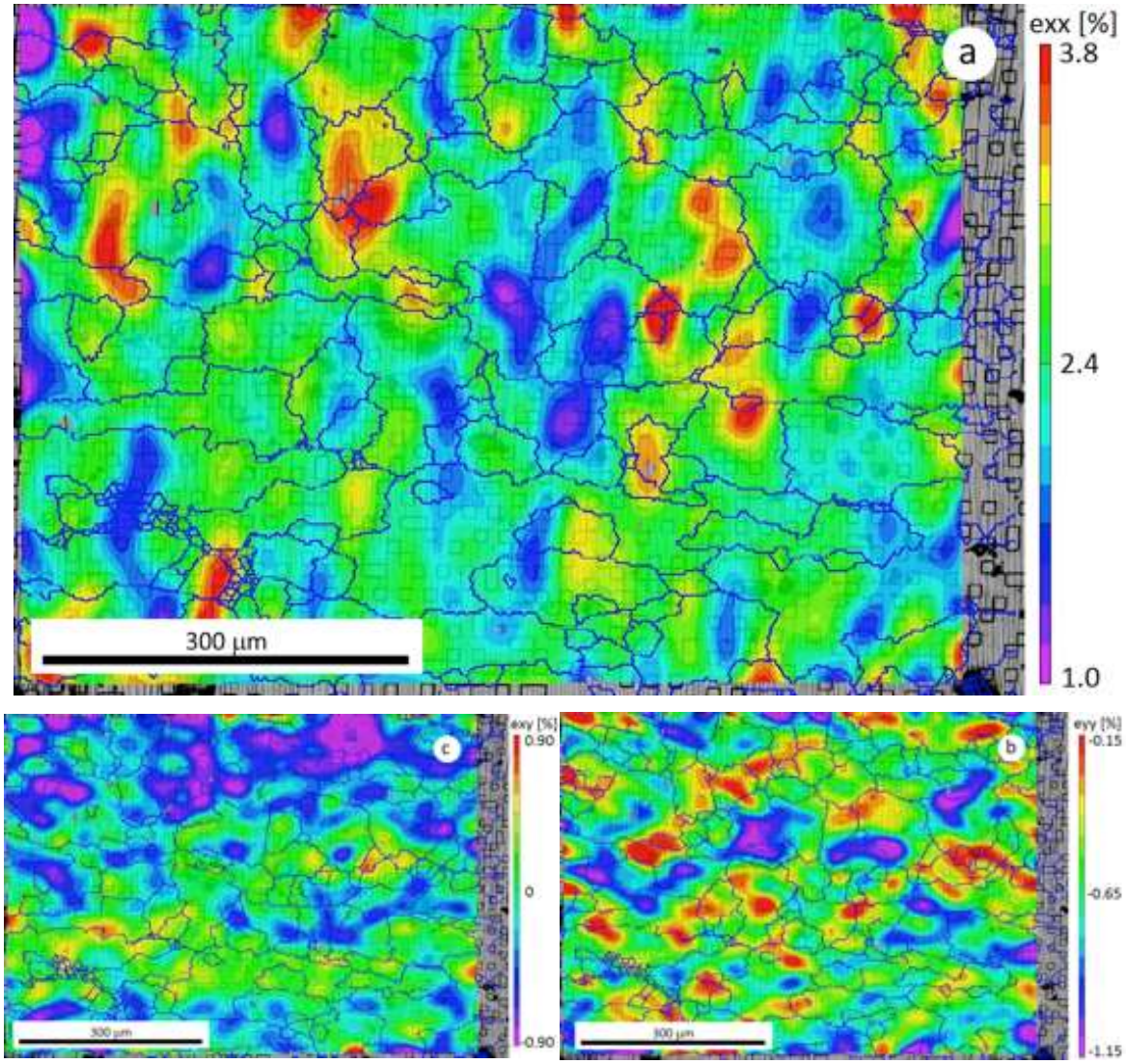

Fig 4.6 Specimen L-T residual (a) ε_{xx} strain field w/avg. strain = 2.44%; (b) ε_{yy} strain field w/avg. strain = -0.75%; and (c) ε_{xy} strain field w/avg. strain = -0.15%.

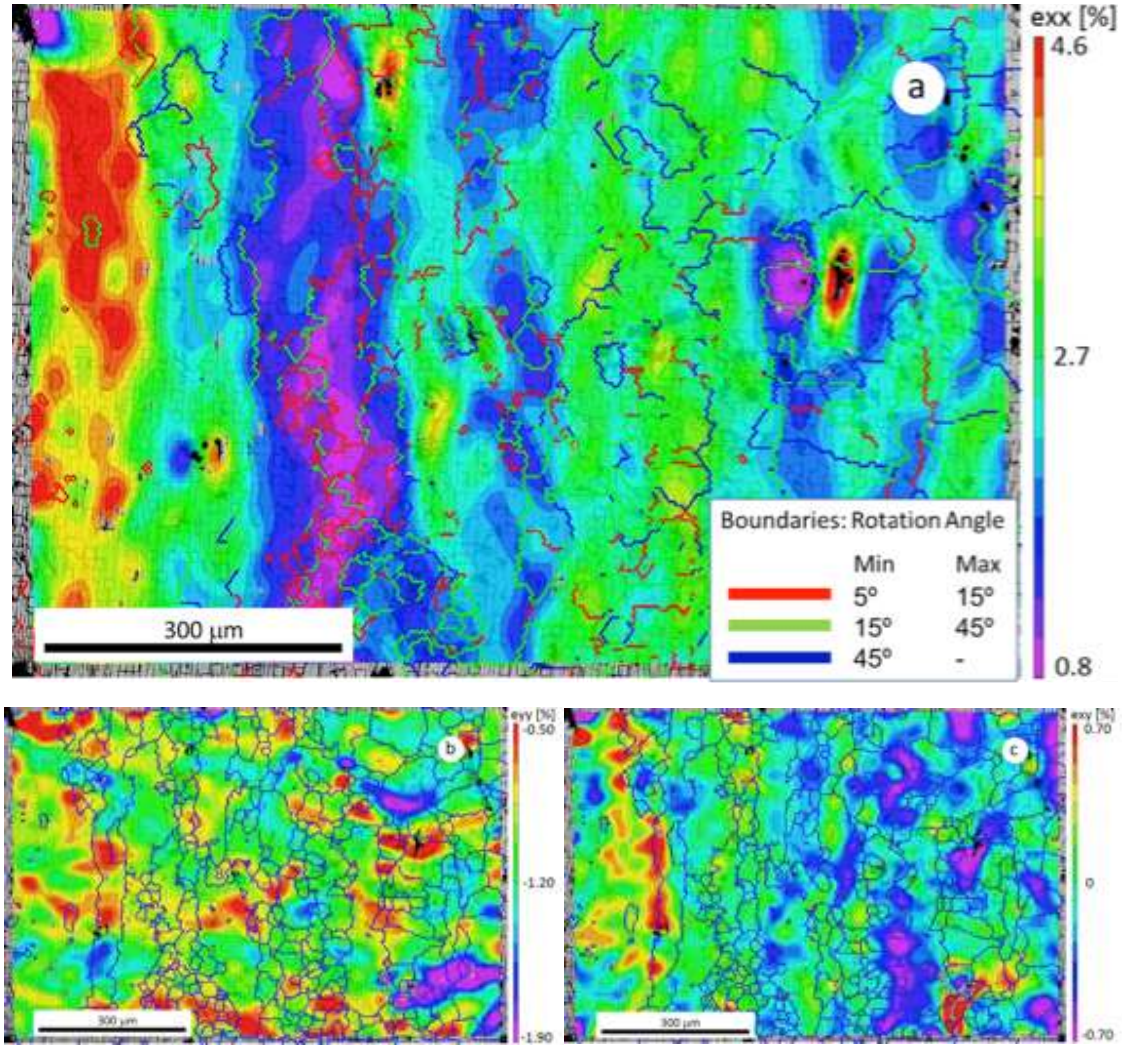

Fig 4.7 Specimen T-L residual (a) ε_{xx} strain field w/avg. strain = 2.41%; (b) ε_{yy} strain field w/avg. strain = -1.02%; and (c) ε_{xy} strain field w/avg. strain = 0.05%.

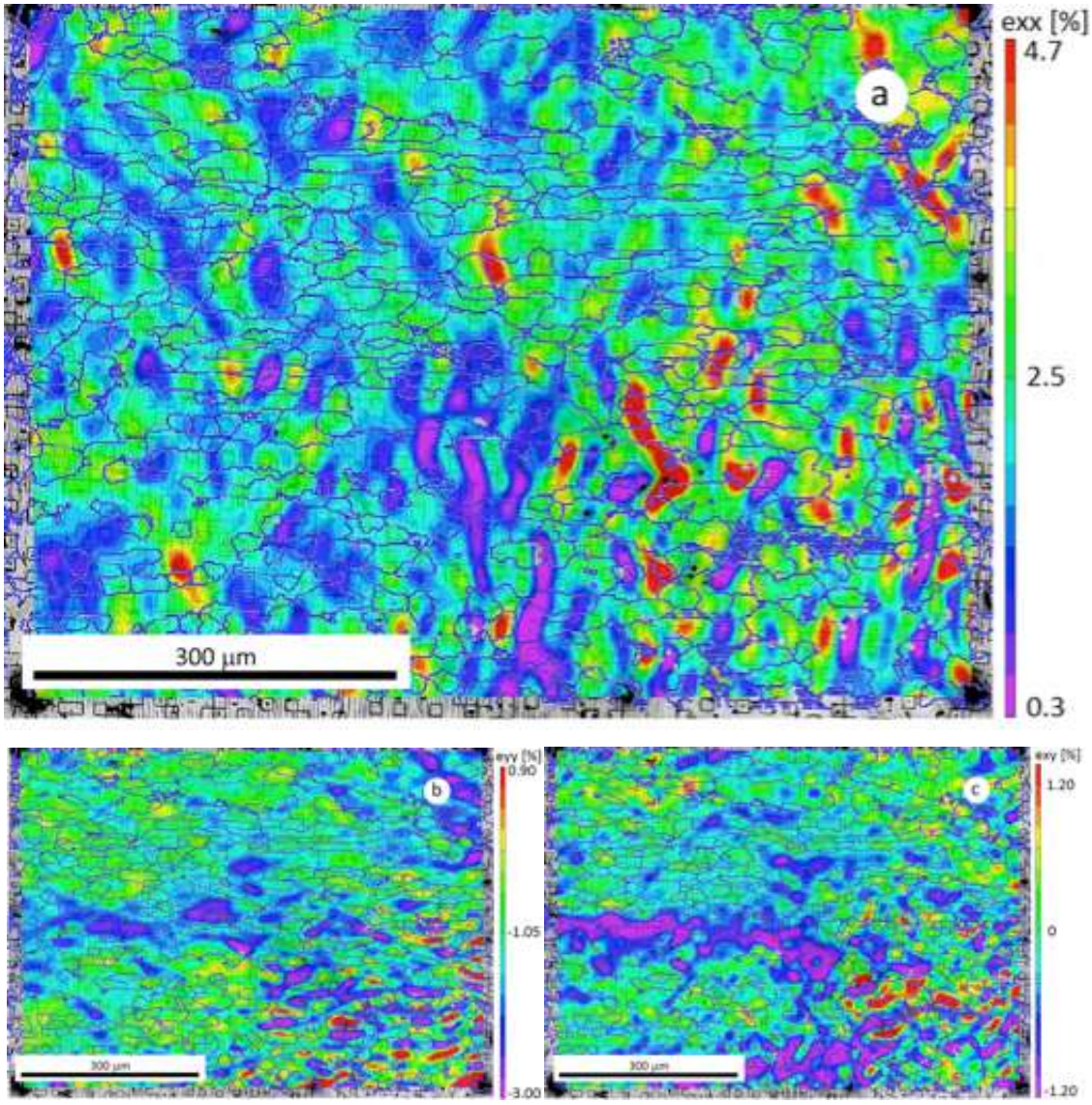

Fig 4.8 Specimen T-S residual (a) ε_{xx} strain field w/avg. strain = 2.26%; (b) ε_{yy} strain field w/avg. strain = -1.18%; and (c) ε_{xy} strain field w/avg. strain = -0.20%.

4.3.2 Simulations

The EBSD orientation data files were used as input files for the simulations. DREAM3D [107] was used to appropriately convert the hexagonal gridded data into a square-gridded format within an h5ebsd file, rotate the Euler frame 90° about the <001> to match the spatial frame, and correct any bad data point encountered (confidence index below 0.2 and local misorientation angle above 5°). The final simulation files contain the orientation angles, the spatial locations, the grain

ID, and the phase id number. A macroscopic strain rate along the *x*-direction was imposed while allowing the other components to adjust for stress-free conditions.

The final simulation sizes for each specimen was (i) T-L = 232x190x1 voxels = 1000x700x3.7 μm; (ii) L-T = 361x290x1 voxels = 938x754x2.6 μm, and (iii) T-S = 372x297x1 voxels = 967x772x2.6 μm. To ensure a 2^n geometry required for FFT, extra gas phase and material were added at the boundaries. The grains were assumed to be infinitely columnar so the thickness was left as 1 infinitely periodic voxel to ensure a plane strain model. A summary of the elastic and plastic material parameters used to model AA7050 can be seen in **Table 3.1** and **Table 3.2**, where the parameters used to model the plastic behavior in the Voce Hardening Law were iteratively obtained by matching the EVP-FFT macroscale stress strain curve with the curve experimentally observed on the TS-TL-LT specimens.

4.4 Discussion

Fig 4.9 shows both the simulated and experimental strain field maps for all three specimens. The comparison shows that he simulations do not capture the exact heterogeneous strain distributions at the microstructural features as represented in the DIC-EBSD experiments, especially for the L-T and T-S specimens. However, they correctly predict the statistical strain distributions for each crystallographic texture, as seen on **Fig 4.10**. Both figures show that low macroscopic loadings may create high local plastic strains prone to failure.

The possible sources for the discrepancy between simulated and experimental strains are explained as follows: (i) the boundary conditions may be different, since the simulation applies a uniform strain rate on the entire material whereas in reality this is only applied to the grips of the specimens (ii) the unknown subsurface has a considerable effect on the surface strain response [52] and therefore the columnar assumption needs further study, possibly by using oligocrystals [98][63] (iii) the physics of the constitutive equations used in the materials models is incomplete, especially when using such a simple hardening law for which the resulting slip system activity can vary drastically [108], and (iv) the resolution from the 10 μm-pattern DIC is limited. Given that the discrepancy between experimental and modeled strains is lowest for the TS specimen, it is possible that the mechanism dominating the discrepancy between the strains is the subsurface

microstructure, since the TS orientation has the lowest subsurface uncertainty due to the elongated nature of the grains. **Chapter 5** analyzes in further detail the role of subsurface uncertainty on the spatial and statistical prediction of strains.

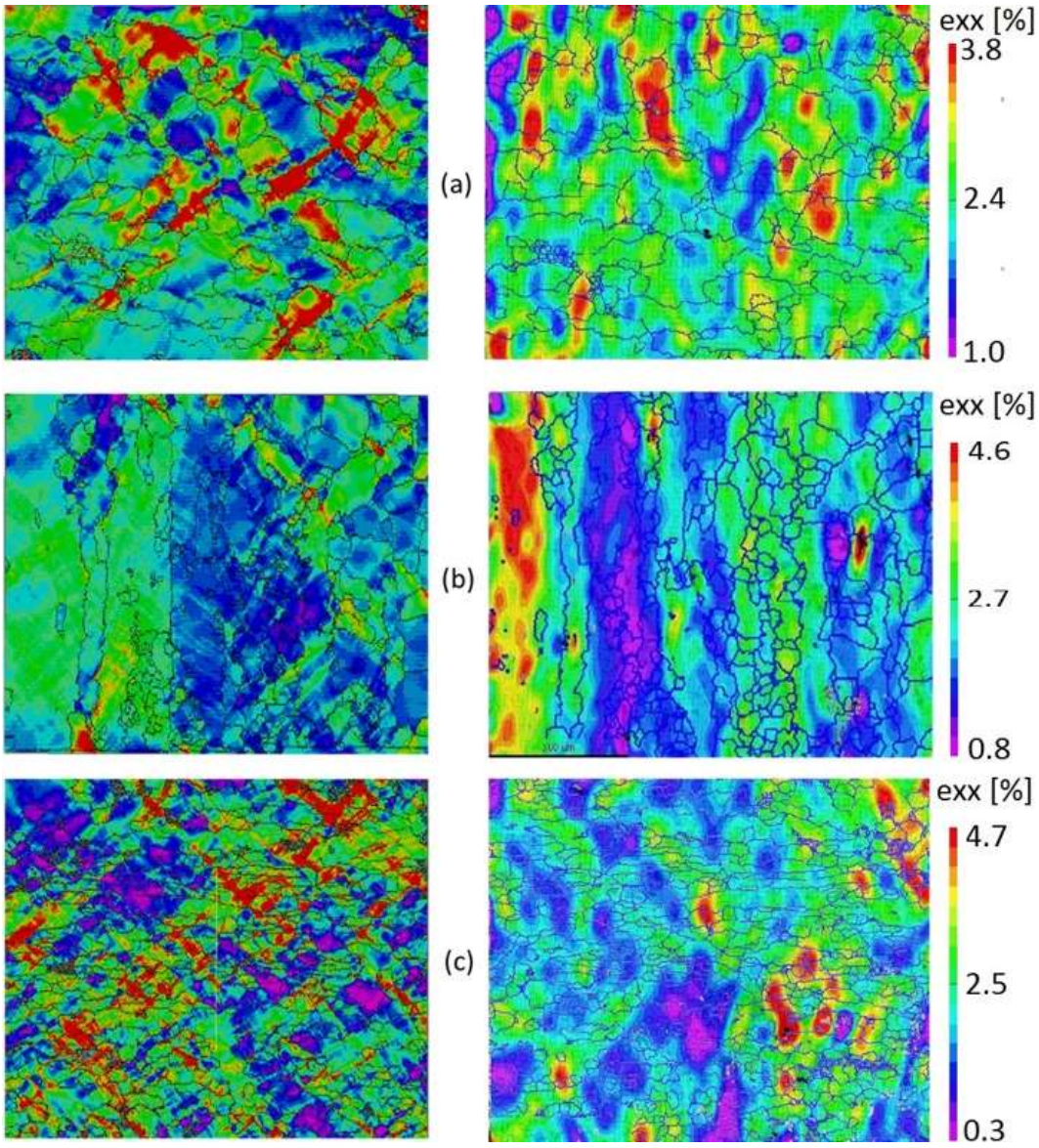

Fig 4.9 Simulation (left) vs. experimental (right) results for (a) L-T, (b) T-L, and (c) T-S specimens.

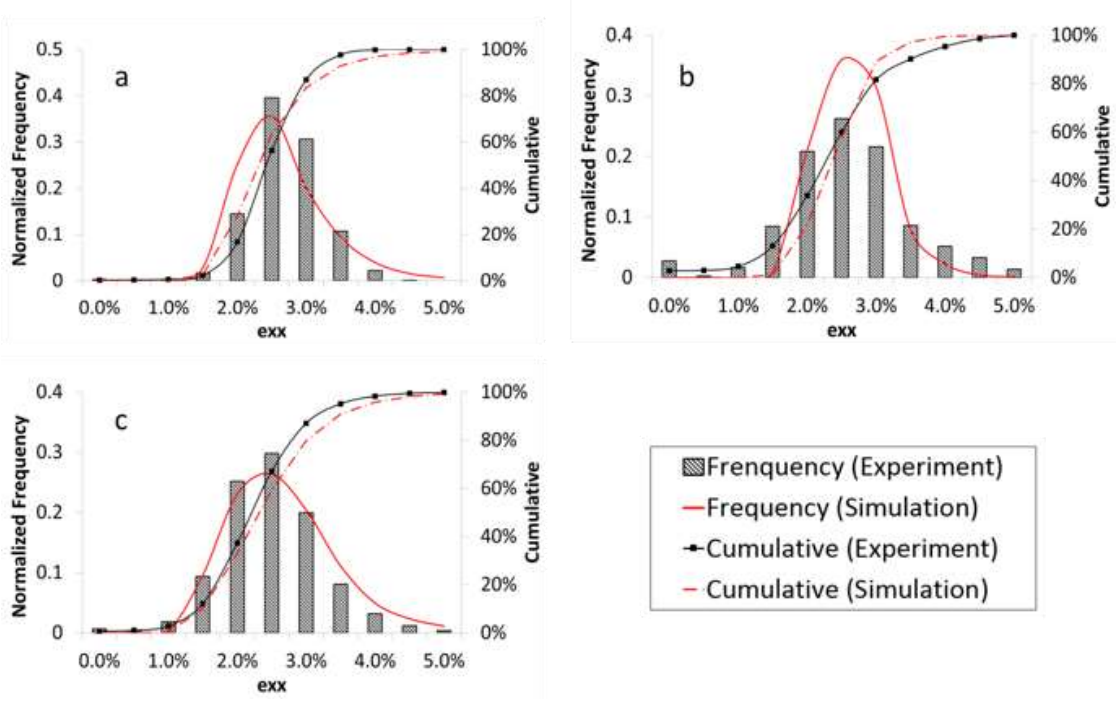

Fig 4.10 Histograms of axial plastic strain distribution for (a) L-T, (b) T-L, and (c) T-S.

4.5 Conclusion

Micro-stamping is very effective for DIC, being the 10 μm base pattern sufficient for grain level resolution of strains. The resulting strain field maps show that the strain varies according to the microstructure. There is a tendency for the axial strain to form isocurves perpendicular to the load of the elongated T-L grains.

The EVP-FFT simulations predict reasonably well the statistical nature of the strain fields, as the maximum microstructural strains were roughly double the macroscopic residual plastic strains, which could be useful on the material design that may experience failure below the yield point. However, EVP-FFT could not accurately predict the heterogeneous strain fields at each microstructural feature.

5. SUBSURFACE UNCERTAINTY FOR ANISOTROPIC MICROSTRUCTURES

5.1 Introduction

To characterize the mechanical behavior of materials, the scientific community usually relies on experimental measurements, such as the ones obtained from DIC, as well as crystal plasticity computer models, which can obtain the mechanical heterogeneity at the microstructural level. Either method, however, has shown to encounter issues with obtaining a full representation of the microstructural behavior, especially when there is only surface data available. As seen by Turner et al. [52], the neighboring microstructure of an analyzed surface strongly affects its strain field. Therefore, unless the uncertainty of the surrounding microstructure is minimized, the accuracy of a simulated strain field will remain unknown. One approach for reducing the subsurface uncertainty is by generating 3D statistically equivalent virtual microstructures, where the statistics necessary to instantiate the virtual microstructure can be directly obtained from surface characterizations.

In this chapter, we propose a subsurface reconstruction methodology that allows us to investigate the effect of the subsurface uncertainty on the modeling of a rolled AA7050-T451 specimen in the transverse short direction (TS) by characterizing its surface response via DIC and comparing the results with two types of EVP-FFT models: a 2D plane strain model without any subsurface information, and a full 3D model with a statistically reconstructed subsurface microstructure. Additionally, a case study is performed on a material with a through-thickness grain structure, thus reducing the subsurface uncertainty, where no subsurface reconstruction is performed and for which the 2D plane strain model should be sufficient.

The experimental testing and characterization in this chapter was performed by Dr. Alberto Mello, with the development of the cast material being performed by Dr. Sun and Dr. Johnson. The reconstruction and modeling was performed by the author. Full details of this chapter can be found in: *A. Nicolas, A.W. Mello, Y. Sun, D.R. Johnson, M.D. Sangid, Reconstruction Methods and Analysis of Subsurface Uncertainty for Anisotropic Microstructures, Mater. Sci. Eng. A. (2019) Accepted.*

5.2 Materials and Methods

5.2.1 Specimen Characterization

A tensile specimen of AA7050-T4751 was machined in the transverse-short direction (T-S), thus aligning the elongated grains along the thickness of the specimen, where the subsurface uncertainty can be considered to be low. The geometry was the same one described in **Chapter 4**. As a case study of a microstructure with minimized subsurface uncertainty, a second variant of AA7050 was produced via directional casting to generate verifiable through-thickness grains, with cold work performed on the material to emulate the wrought processing of rolled AA7050. Full details of this material can be found in **Appendix A**. For the rolled TS AA7050 specimen a 300 μm x 400 μm ROI was delimited at the center of the specimen by adding fiducial markers via microhardness indents (LECO LM247AT). Afterwards, the specimen was thoroughly cleaned in acetone and methanol in a sonicator for 3 minutes each. The ROI was then characterized via EBSD.

5.2.2 DIC Experimental Procedure

DIC was performed using nanoparticle patterning of titanium [46] at the surface of the specimen. A full description of the speckling procedure is available in [47]. To ensure a high-resolution characterization, the ROI was also subdivided into 9 regions with a 20% surface overlap and separately scanned via SEM using a 10 kV voltage, a spot size of 4, a 10 mm working distance, and a 700x magnification. Each scan had a resolution of 14.5 pixels per μm. DIC was then performed on each of the 9 regions using a subset size of 111 pixels (7.7 μm) and a step size of 2 pixels (0.14 μm). Afterwards, the DIC maps were corrected for distortion following the correction protocol described on [89]. The final strain map of the ROI composed of nine strain datasets stitched after correlation are shown in **Fig 5.1**. The tensile experiment was conducted at room temperature (23 °C) in a 6.7 kN electromechanical Mark-10 ESM-1500 Force Test Stand. The force indicator has a ±0.1% of full scale accuracy with a resolution of 5 N. The cross head displacement has a travel resolution of 0.02 mm, and the tests were conducted at 2 mm/min. An Epsilon extensometer Model 3542 was used to measure strain. The targeted strain, 3%, was chosen to ensure that the material was loaded beyond the elastic-plastic transition and significant strain localization occurred.

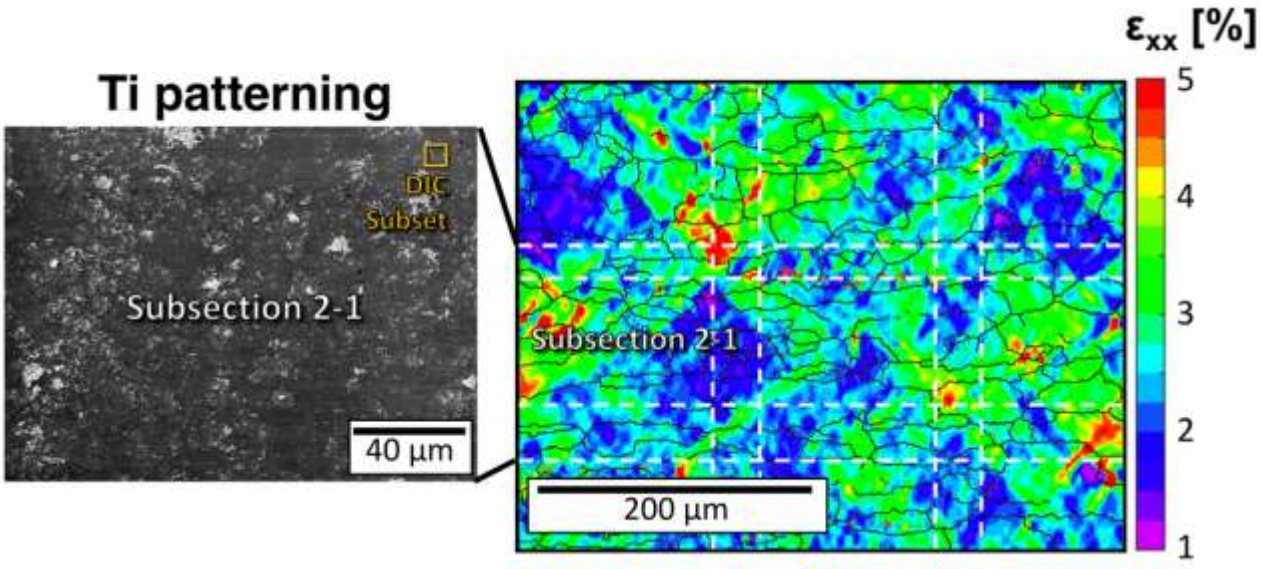

Fig 5.1 View of the titanium speckle patterning tracked before and after deformation (left) and the resulting full axial strain map (right) after stitching the 9 regions together after DIC.

5.2.3 Crystal Plasticity Simulations

The surface EBSD scans were used to instantiate two types of EVP-FFT models: one without subsurface reconstruction, therefore limiting the simulation to a 2D model, and one with a 3D subsurface microstructure statistically reconstructed from the EBSD data. The modeling of both types of microstructures will help understand two main points: a) how the subsurface uncertainty affects the discrepancies between the simulations and experiments and b) the potential of statistical subsurface reconstructions as a tool to improve microstructural models.

5.2.3.1 Preprocessing of EBSD orientation Data

The square grid data from the EBSD orientation file was preprocessed with DREAM3D [107] to remove noise in the data. The optimal microstructure representation is obtained from the EBSD scan when a point is cleaned if both the confidence index is below 0.2 and the misorientation angle relative to at least six of its 8 voxel neighbors surpasses 5°. For all simulations, the spacing between data points was indicated by the step size from the EBSD scan. Next, the data file was imported into an h5 file, and the Euler frame was rotated 90° about the <001> to match the spatial frame. The final orientation file contained the grain orientation (in Euler angles), the spatial locations, the grain ID, and the phase to which every spatial point belongs.

5.2.3.2 Subsurface Reconstruction Methodology

To reconstruct a subsurface that can properly represent the geometry and the orientation distribution of the AA7050 samples in the TS orientation of the rolled plate, an algorithm capable of extracting information directly from the EBSD surface scan was developed. The full algorithm can be found in **Appendix B**. An overview of the subsurface reconstruction procedure can be seen in **Fig 5.2**.

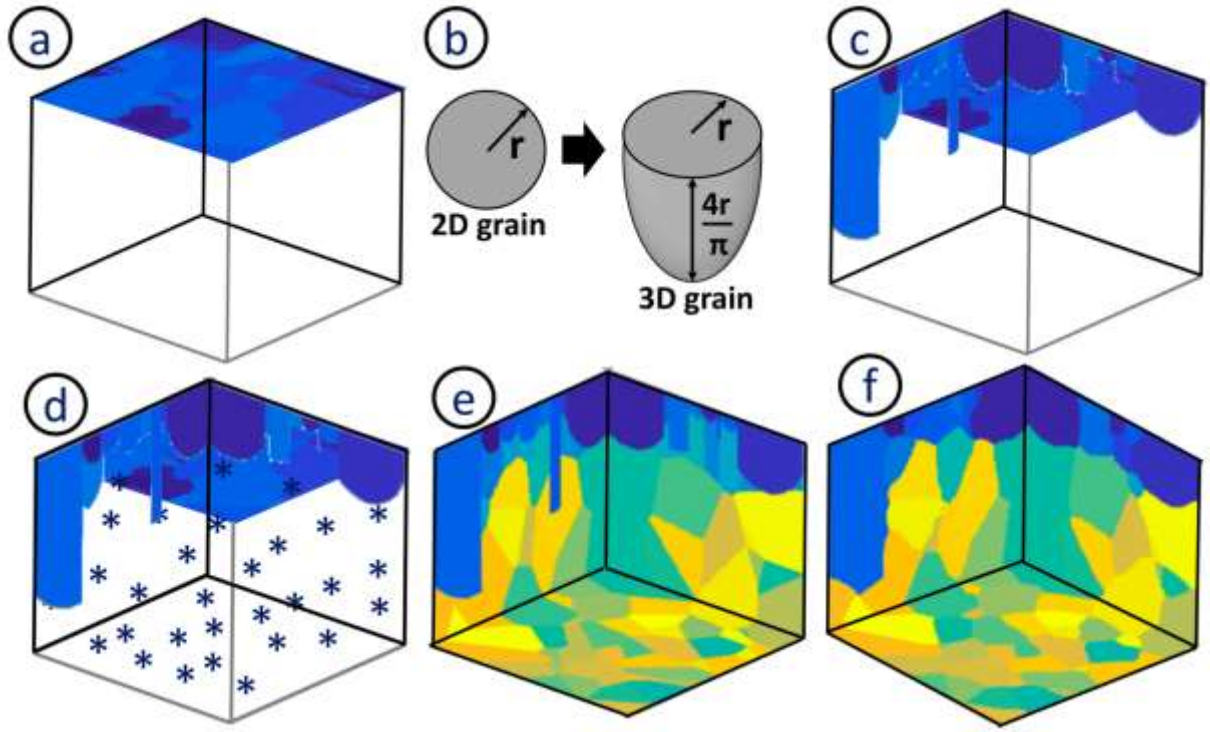

Fig 5.2 Visual overview of the subsurface reconstruction algorithm. First the EBSD characterization is used as input to directly reconstruct the subsurface geometry (a-c). Then tessellated grains are generated (d-e) based on spatial distances observed for this material from EBSD characterization of orthonormal sections [110]. A final smoothing is performed (f) to improve the grain morphology.

For the first step to reconstruct a statistically equivalent subsurface, the grains part of the EBSD characterization were allowed to grow into the subsurface a distance based on the equivalent radius of the grain of interest with a stereological factor of $4/\pi$, which has been shown to be a reasonable scaling value from 2D to 3D [109]. Next, tessellations of randomly generated grain seed points were generated underneath the extruded grains. The seed points were spatially positioned to maintain the statistical grain aspect ratio. These length-to width grain size ratios were

statistically obtained from surface EBSD scans of rolled AA7050-T7451 along the rolling direction (LT), across the rolling direction (TL), and transverse to the rolling direction (TS) obtained on a previous study of the same material [110].

The third step involved statistically equivalent grain orientations for the grain seed points from the surface EBSD characterization via the *StatsGenerator* command in DREAM3D [107]. This ensures that the texture present on the specimen is preserved in the model. As a fourth and final step, the entire microstructure, excluding the EBSD surface, was further refined via an erosion-dilation smoothing algorithm to remove the unnaturally sharp grain boundaries generated from the extrusion and tessellation of grains. This type of reconstruction allows for a direct spatial comparison between the strain distributions at the surface of the 3D simulation and the experimental strains observed in the material, which is very advantageous since the user is not limited to purely statistical comparisons to assess the performance of the computer model.

5.2.3.3 2D and 3D modeling

To examine the effect of the subsurface uncertainties on the modeling results, as well as the performance of the proposed reconstruction methodology, one 2D model and two 3D subsurface reconstructions were generated for the same EBSD scan. Each 3D subsurface reconstruction contained the same surface microstructure, but the subsurface microstructure exhibited different grain morphologies and orientations. Each microstructure was used as input for EVP-FFT modeling [55], and a gas phase was added on the free boundaries to ensure stress free surfaces, including a gas layer at the surface of the model. Regions of the EBSD scan outside the ROI were included in the simulations until a size of 2^q was reached, where q is a positive integer to satisfy the FFT periodicity requirements, as seen in **Fig 5.3**. Neither of these extra phases outside the ROI was considered for the strain map comparisons. For all three simulations, the minimum size needed for a representative simulation of the strains at the surface was found to be 512 x 512 x n voxels, where n is the subsurface depth that was reconstructed. It is important to note that the periodic nature of the FFT formulation will perceive the 2D model size as 512 x 512 x infinity voxels therefore making it a plane strain model. It should be noted that the results from extruded models with a free surface converged towards the plane strain results, since the plane

strain approach restricts the out-of-plane movement. Parallelization was used as well as the material properties described in **Table 3.1** and **Table 3.2**.

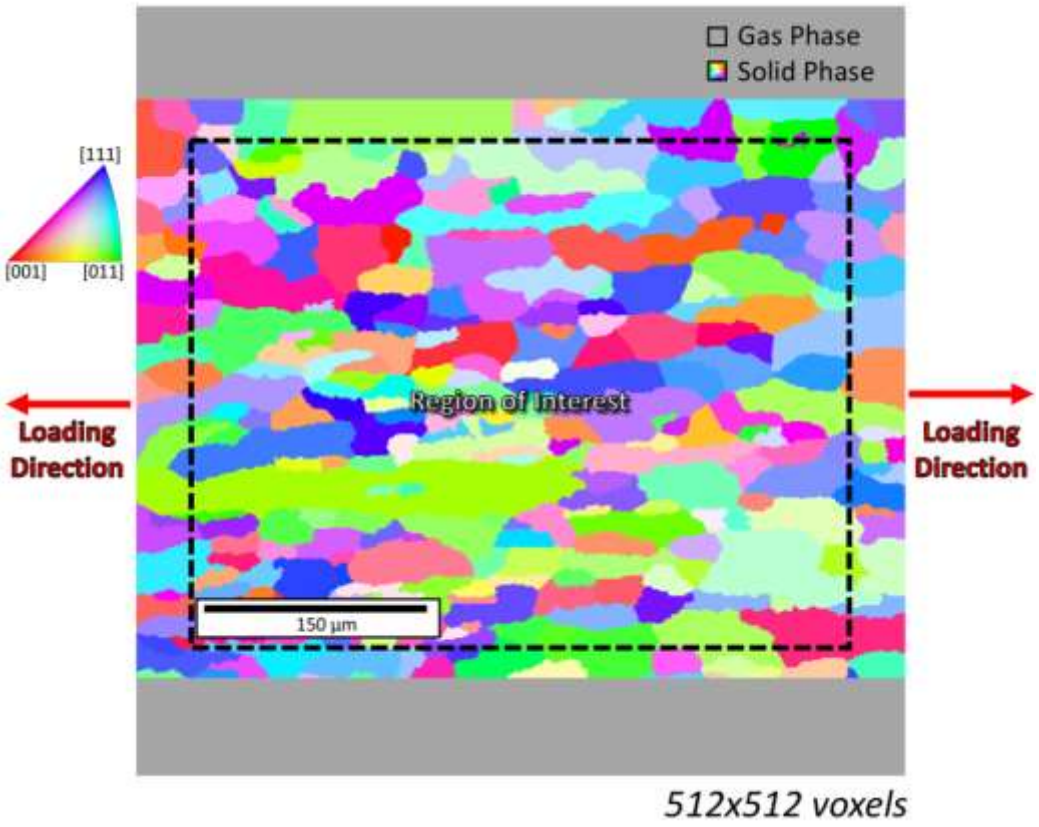

Fig 5.3 Schematic and boundary conditions (BCs) for the EVP-FFT model. The additional material outside the ROI prevents edge effects on the modeling results.

5.3 Results

Strain maps produced by the experiments and simulations, on the same surface microstructure with different subsurface instantiations, were generated and compared. The strain maps were displayed in terms of the maximum principal shear strain, which has been shown in literature to be a good representative of the physical basis for deformation from DIC results [96]. The local principal shear strain was determined by **Eq. 5.1**:

$$\frac{\gamma_{max}}{2} = \sqrt{\left(\frac{\varepsilon_{xx}-\varepsilon_{yy}}{2}\right)^2 + \left(\frac{\gamma_{xy}}{2}\right)^2} \tag{5.1}$$

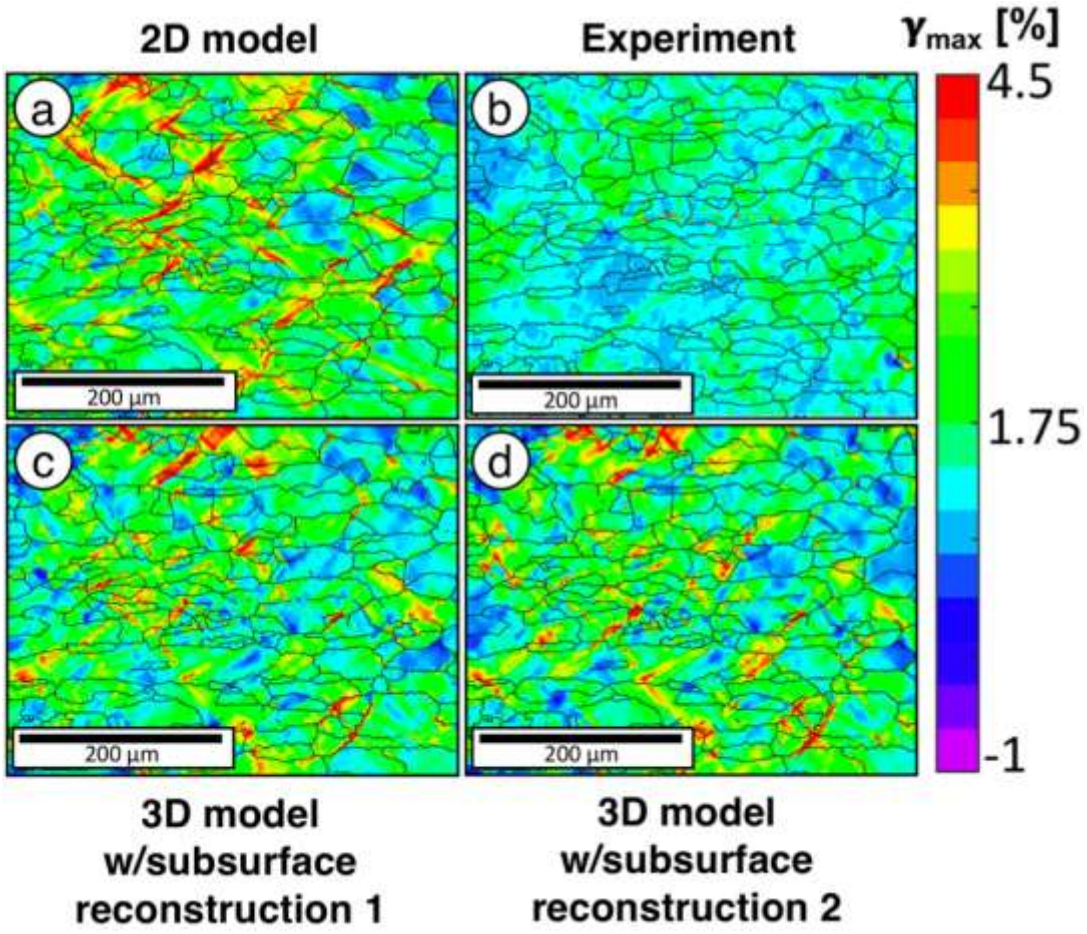

Fig 5.4 Simulated (a,c,d) and experimental DIC (b) residual principal shear strain field maps for an AA7050 specimen in the TS orientation of the rolled plate after applying 3% strain and unloading. Simulation (a) is modeled without the subsurface microstructure and simulations (c,d) are modeled with subsurface reconstructions.

Fig 5.4 shows the in-plane resolved shear strain maps for a specimen extracted from the rolled plate of AA7050 in the TS orientation obtained from experimental DIC, one 2D simulation without subsurface reconstruction, and two 3D simulations with statistical subsurface reconstructions. Each subsurface reconstruction has different subsurface morphologies and orientations, yet are statistically representative of the characterized microstructure. The 2D model shows high strain values localized over fairly large regions, especially when compared with the 3D models with a subsurface reconstruction, which show better distributed strains with sparse strain localizations.

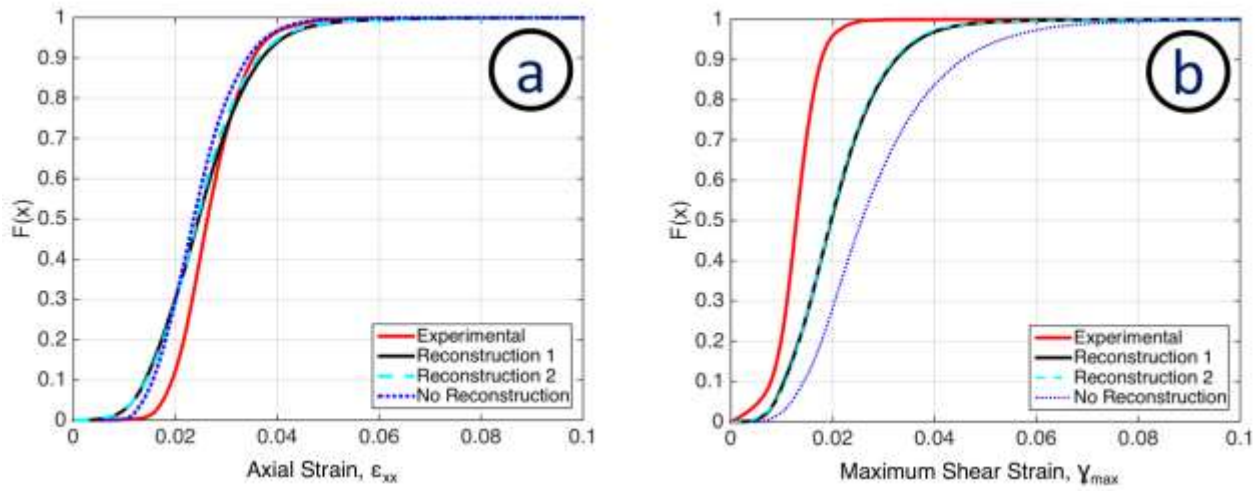

Fig 5.5 Cumulative distribution function plots for (a) the axial strains, ε_{xx}, and (b) the maximum in-plane shear strains, γ_{max}. While all models capture the observed uniaxial strain, when analyzing the worst-case deformation scenario via the in-plane principal shear strains, the addition of a subsurface reconstruction improves the predictions.

Fig 5.5 shows a statistical comparison between modeled and experimental strains. The models are shown to properly capture uniaxial strains, which is reasonable since the EVP-FFT results were calibrated to match the macroscopic uniaxial deformation. On the other hand, the maximum in-plane shear strain, an important metric for the local deformation in the material, is heavily over-predicted by the 2D model. The prediction only improves when a 3D subsurface reconstruction is added to the model.

Therefore, as a conservative approach, the maximum in-plane shear strain is further studied spatially. A good prediction of this metric ensures that the overall deformation of the material has been properly captured, which includes the axial strains. To perform a spatial comparison between experiments and simulations, the maximum in-plane shear strain field was tracked grain by grain and the grain average values were plotted for each simulation. The centers of the ellipses represent the average strain and the size of the horizontal and vertical axes for each ellipse represents the standard deviation inside the grain for the experimental and simulation strain values, respectively.

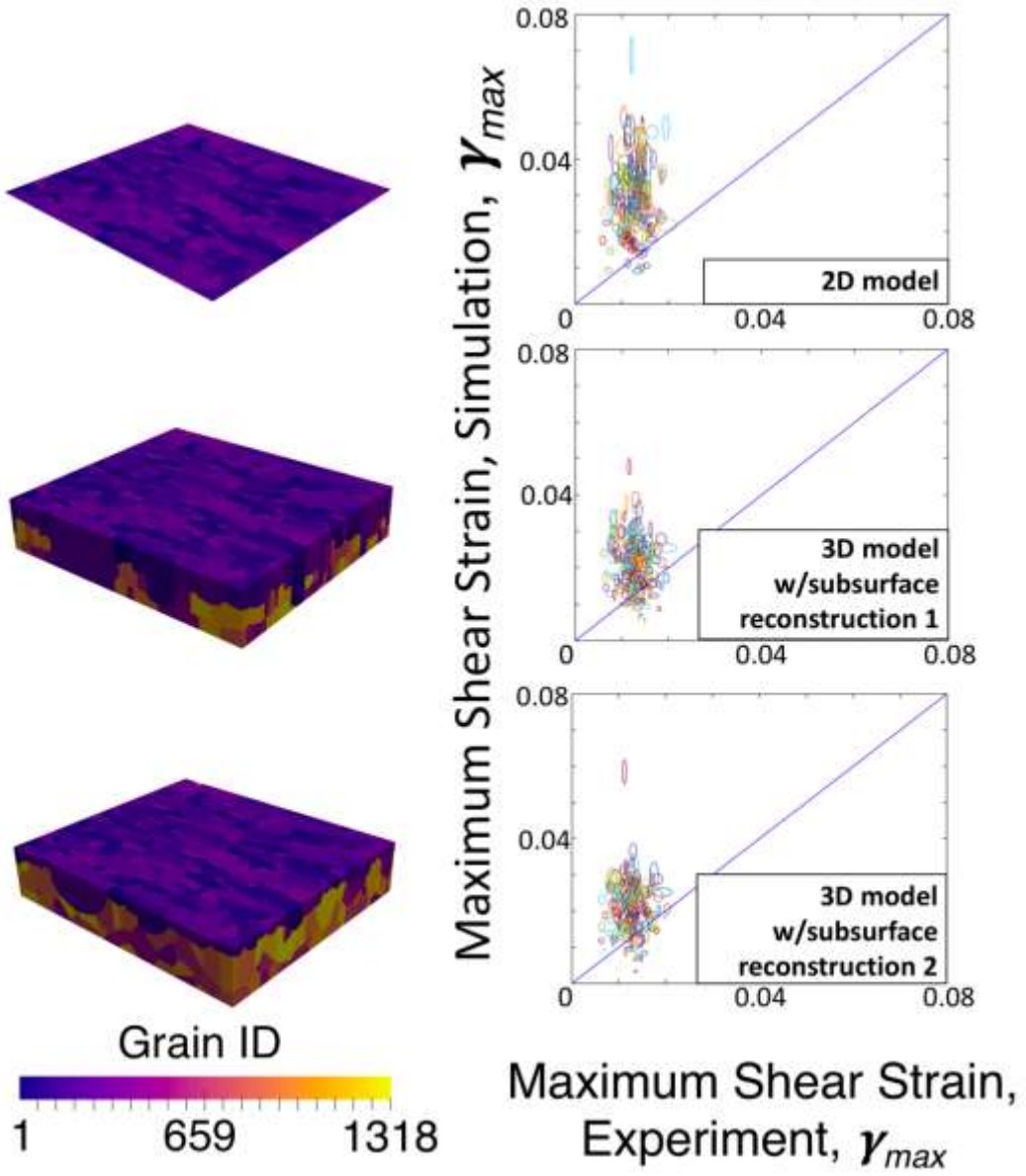

Fig 5.6 Maximum in-plane shear strain grain-by-grain comparison between experiment and simulations with subsurface reconstructions (second and third rows). The 2D model case in the first row assumes a purely elongated structure.

Fig 5.6 shows a grain-by-grain comparison of the experimental and simulated maximum shear strains, as well as the geometry of the models with and without subsurface reconstructions. The grain-by-grain analysis reveals an over-prediction of the maximum in-plane strains for the 2D model (row 1) and a closer prediction of surface strains from the 3D models with subsurface reconstruction (row 2 and row 3).

When measuring the goodness-of-fit, R^2 [111], of the plotted average maximum in-plane shear strain values relative to the $f(x) = x$ line for the specimen from the TS orientation of the rolled AA7050 plate, the 2D model exhibits an R^2 = 0.62. On the other hand, the 3D models with subsurface reconstruction show a value of R^2 = 0.76 for reconstruction 1 and of R^2 = 0.75 for reconstruction 2. In this work, a good fitness of value R is considered to be anything above 0.75, meaning that 75% of the variance is related. The goodness-of-fit values show that the addition of a statistically equivalent subsurface microstructure noticeably improves the prediction of the strain distributions on the grain scale.

5.4 Discussion

The results show that minimizing the subsurface uncertainty is indeed playing a key part in bridging the gap between the strain results for the experiments and simulations, even for the highly elongated microstructures indicative of rolled materials in which the 2D microstructures and plane strain assumptions are usually deemed to be a reasonable assumption given the highly elongated grains. It should be noted that the plane strain results converge towards the models of an extruded grain morphology with a free surface. We further discuss the degree of agreement in the model strain response, as well as the mechanisms behind this behavior. **Fig 5.5** and **Fig 5.6** show a significant improvement of strain predictions for the models with a subsurface reconstruction. While there is still some over-prediction of the in-plane shear strains, it is significantly less than the case for the 2D model without any subsurface reconstruction. This is possibly due to the role of the subsurface microstructure in providing additional degrees of freedom that can help the grains at the surface to accommodate deformation.

Also, the subsurface grain morphology is relatively insensitive to the degree of match between the simulations and the experiment at the surface. Reconstruction 2 underwent an additional level of grain boundary smoothing, as compared with Reconstruction 1, yet both simulations with subsurface reconstructions exhibit evenly distributed strains and equally matched the strain magnitudes to those of the experiment, as both have an R^2 value of roughly 0.75. It seems that as long as the subsurface is accounted for, the EVP-FFT simulation yields improved results, both spatially and statistically, when compared to the experimental strain field obtained from DIC.

To further understand the role of the subsurface uncertainty, a material with minimized subsurface uncertainty was developed, in which the specimens exhibited a through thickness grain structure. This material, further described as through-thickness cast AA7050, was then analyzed as a case study in the same manner as the rolled TS AA7050 specimen. Two specimens were manufactured from standard AA7050 using a directional casting methodology, please refer to **Appendix A** for the processing and characterization details. The through thickness grain structure was verified via EBSD characterization of the front and back surfaces of the specimens. When modeling the cast AA7050 material, only the EBSD scans of the front faces of the specimens were used to construct the EVP-FFT simulation models. Similarly, to the 2D model, without subsurface reconstruction, each cast specimen is modeled as a 2D extrusion, where in this case the highly elongated nature of the grains is no longer an assumption but a verified characteristic of the material morphology. The material parameters were obtained from the macroscopic stress-strain curve, which exhibited the same elastic response of rolled AA7050 but a different plastic response due to the limited degrees of freedom of perfectly elongated grains. The elastic parameters were the same ones used to model rolled AA7050 (**Table 3.1**), and the Voce hardening parameters changed to $\boldsymbol{\tau_0}$ = 142.5 MPa, $\boldsymbol{\tau_1}$ = 12 MPa, $\boldsymbol{\theta_0}$ = 30, and $\boldsymbol{\theta_1}$ = 5 to comply with the macroscopic response.

When analyzing the maximum in-plane shear strain in the material (Eq. 5) after deformation and subsequently unloading the sample, the model of the casting is observed to accurately predict the shear distributions and magnitudes, as seen in **Fig 5.7** and in **Fig 5.8**. The grain-by-grain analysis shows a R^2 = 0.88 for specimen 1 and a R^2 = 0.78 for specimen 2. For such a material, the movement of the through-thickness grains is very limited in the out-of-plane direction and therefore the 2D model is better for capturing the actual response of the material. The constraints of a through-thickness grain structure also explain the high levels of shear strains localization compared to that of the rolled microstructure, as there are no additional subsurface grains in the cast materials that allows for strain redistribution. This has an important implication, since it means that as long as the subsurface is properly accounted for either by reconstruction or by a full knowledge of the subsurface microstructure, simulations can inexpensively provide a description of localized strain and potentially define the sites of crack initiation. Finally, to analyze the effect of the grain morphology and the texture of the material on the surface strains, additional

reconstruction instances of the rolled AA7050 specimen were generated, with some reconstructions containing the same grain morphology but different grain orientations, and some reconstructions containing the same grain orientations but different grain morphologies. All reconstructions yielded similar results to the ones observed in **Fig 5.4**, **Fig 5.5** and **Fig 5.6**, with no appreciable difference arising from the grain morphology or texture. Therefore, it can be surmised that the main mechanism behind the improvement of mechanical predictions is the additional degrees of freedom that the subsurface provides to the surface grains, even if said grains are known to be elongated.

The results confirm that the subsurface uncertainty is a strong factor affecting the strain distributions of not only equiaxed microstructures [59][60][61] but also heavily elongated and textured microstructures, and therefore needs to be taken into account for improved reliability of simulation results. Furthermore, the proposed subsurface reconstruction methodology provided a reasonable method for minimizing the subsurface uncertainties and improving the predictions of the mapped surface strain fields on standard materials, with the advantage of allowing direct spatial comparisons between the observed strains in the material and the model instantiation.

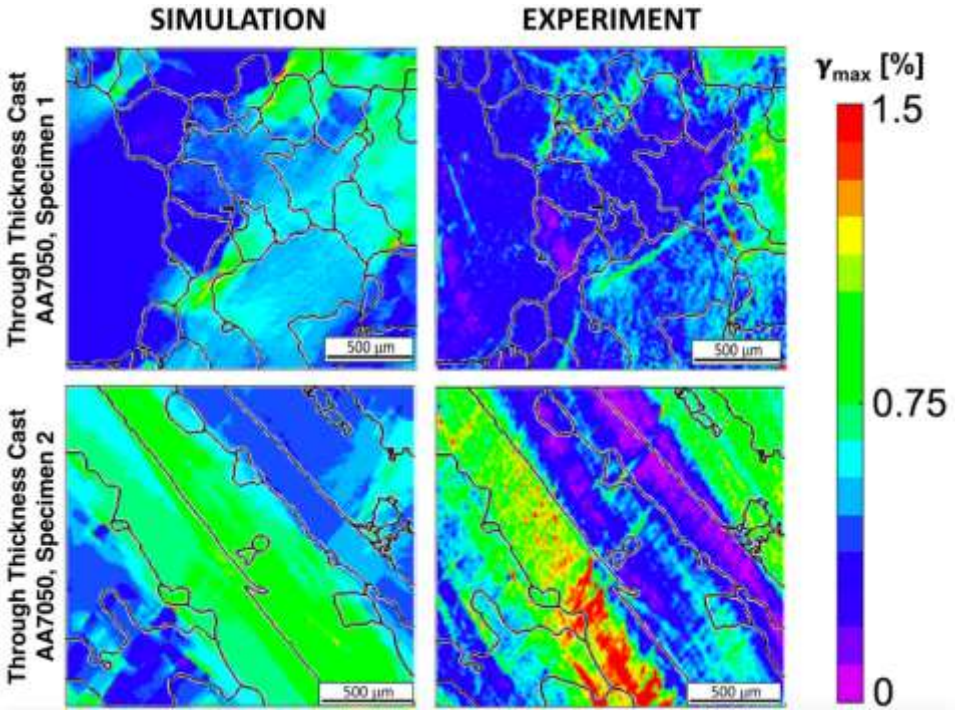

Fig 5.7 Simulated and experimental (DIC) residual principal shear strain γ_{max} field maps for the AA7050 cast samples with through thickness grain structure, specimen 1 (row 1) and specimen 2 (row 2) after 1% strain.

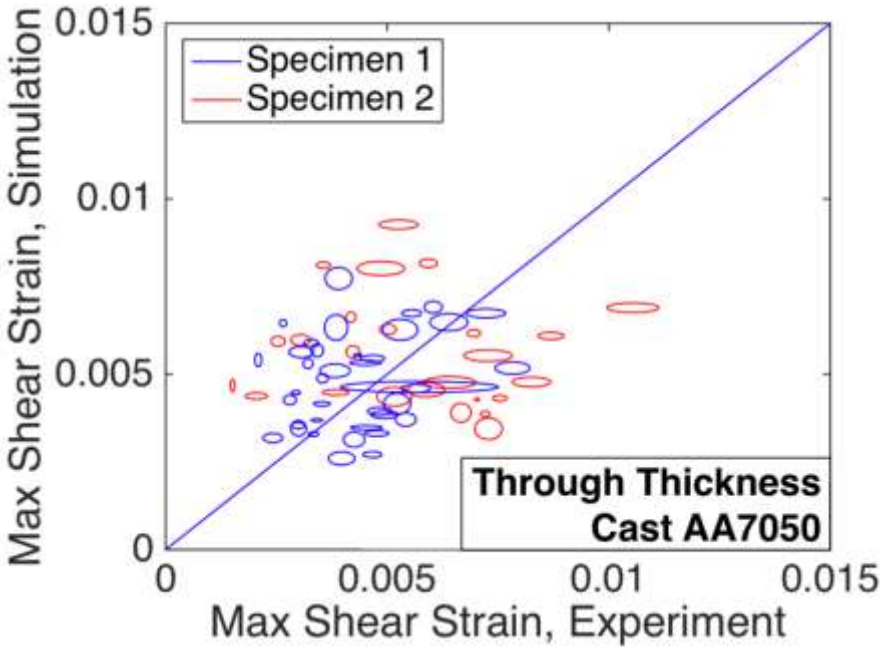

Fig 5.8 Maximum in-plane shear strain grain-by-grain comparison between experiment and simulation for AA7050 cast samples with through-thickness grains.

5.5 Conclusion

The subsurface uncertainty of materials plays an important role in the discrepancy observed between the surface strain results from DIC experiments and simulations for which only the surface microstructure is known. However, it is usually assumed to play a less significant effect for materials with elongated grain morphologies. To investigate the extent to which the subsurface uncertainty of rolled materials affects the predictive capabilities of their respective computer models, two materials have been characterized and simulated: rolled plate of AA7050 with specimens taken from the TS orientation for which only the statistics of the subsurface morphology are known and cast specimens AA7050 material exhibiting a through thickness grain structure with minimized subsurface uncertainty. All computer models were done with a high voxel resolution and sufficient material padding to prevent any effects from the periodic boundary conditions. The experimental strain characterizations were performed with high resolution patterning and a distortion correction protocol to minimize characterization errors. Given the results from the characterizations and simulations of these two sets of specimens, the significant contributions of this study are summarized as follows:

- The EVP-FFT simulation of a 2D representation for the TS orientation from rolled plate of AA7050 material, without subsurface reconstruction, over-predicts the maximum in-plane shear strains at the surface. However, when adding a 3D statistically representative subsurface reconstruction to the model, the prediction of the shear strains is greatly improved. The improvement is due in part to a redistribution of strain and additional degrees of freedom to allow for out-of-plane movement of the surface grains. Hence, the addition of the statistically equivalent subsurface reconstruction effectively reduces the subsurface uncertainty in the surface strain response by ensuring that a minimum of 75% of the strains are replicated by the model.
- A full subsurface reconstruction methodology has been developed, in which the main source of information is based on information provided by the EBSD surface characterization. This reconstruction methodology not only creates a reasonable microstructure both in terms of grain morphology and orientation, but also allows for a one-to-one spatial comparison between surface strain characterization and the results from the reconstructed model.

- The EVP-FFT simulation of AA7050 samples fabricated with a through thickness grain structure, thereby minimizing the subsurface uncertainty, predicts the strain distributions at the surface reasonably well. From the results of the set of simulations in this study, the experimental strain distributions are more accurate from models with more reliable instantiations of the true subsurface microstructure of the material.

6. EFFECT OF RESIDUAL STRAIN LOCALIZATION ON CORROSION

6.1 Introduction

AA7050-T7451 is commonly used in airframe applications where high tension and compressive loads are present [112] and its life is conditioned by corrosion pitting that develops on saline environments, as pits are the main source of cracks [27]. As a result, there is an interest to understand the mechanisms behind corrosion pitting and its eventual transition to cracking [113][114][26]. For aluminum alloys, particularly the 7xxx series, pitting originates at the cathodic Al_7Cu_2Fe particles that are [115], due to the galvanic coupling with the anodic matrix [116][21]. The anisotropy of the rolled material aligns these particles with the rolling direction (L), thus causing pitting on the transverse short (TS) plane [22], therefore making the TS orientation the one of interest [25].

Since crack initiation occurs at pits as small as ~ 50 μm [4], it is important to study corrosion during its early stages before it reaches a critical size. From a mechanical perspective, the residual loads affect the corrosion behavior as they either encourage pit growth [9] or retardation [10]. However, most studies spatially relating mechanical deformation with localized corrosion only measure the response of the material at the macroscale level [11][12], and the few cases studying localized deformation use x-ray for zones of ~4 μm [13], or electron microscopy for zones under ~ 1 μm [14], both of which yield small fields of view, with larger windows requiring low-resolution techniques that prevent the mechanical study of cathodic particles with diameters of ~10 μm [15].

As a result, little is known regarding the effect that the deformation and the microstructure have on corrosion at the mesoscale level. There is a need to examine large areas spanning several particles by characterizing the microstructure, the micromechanical fields, and the galvanic corrosion of a large ROI with known particle locations using high-resolution methods [43][117]. To capture the early stages of corrosion, the surface topology is measured every day for a total of 20 days of saline solution exposure. Using the quantitative results from these characterization procedures, the driving mechanisms behind galvanic corrosion are also investigated.

The experimental DIC and EDS characterization in this chapter was performed by Dr. Alberto Mello, whereas the EBSD and CLSM characterizations, as well as all the data analysis were performed by the author. A complete description of this chapter can be found in*: A. Nicolas, A. Mello, M. Sangid, The effect of strain localization on galvanic corrosion pitting in AA7050, CORROSION. (2018). doi:10.5006/2729.*

6.2 Materials and Methods

6.2.1 Specimen Characterization

A tensile specimen with the geometry described in **Chapter 4** was machined in the TS direction from a rolled AA7050 plate. The microstructure, the particles, the residual strain fields, and the corroded surface were characterized over a 300 µm x 400 µm ROI at the center of the sample. The TS specimen was polished down to a mirror-like surface and the ROI was delimited via fiducial marking with two larger marks added on the lower left as visual aid. EBSD was done on the ROI using 25 kV and a spot size of 5, and the resulting IPF map in **Fig 6.1a** yielded an average grain diameter of 35 µm. The characterization of the Al_7Cu_2Fe particles was done via EDS, yielding the resulting map in **Fig 6.1b** was in agreement with both SEM maps at the ROI and literature [15][117]. The mean and maximum particle diameter were 2.56 µm and 9.34 µm, respectively.

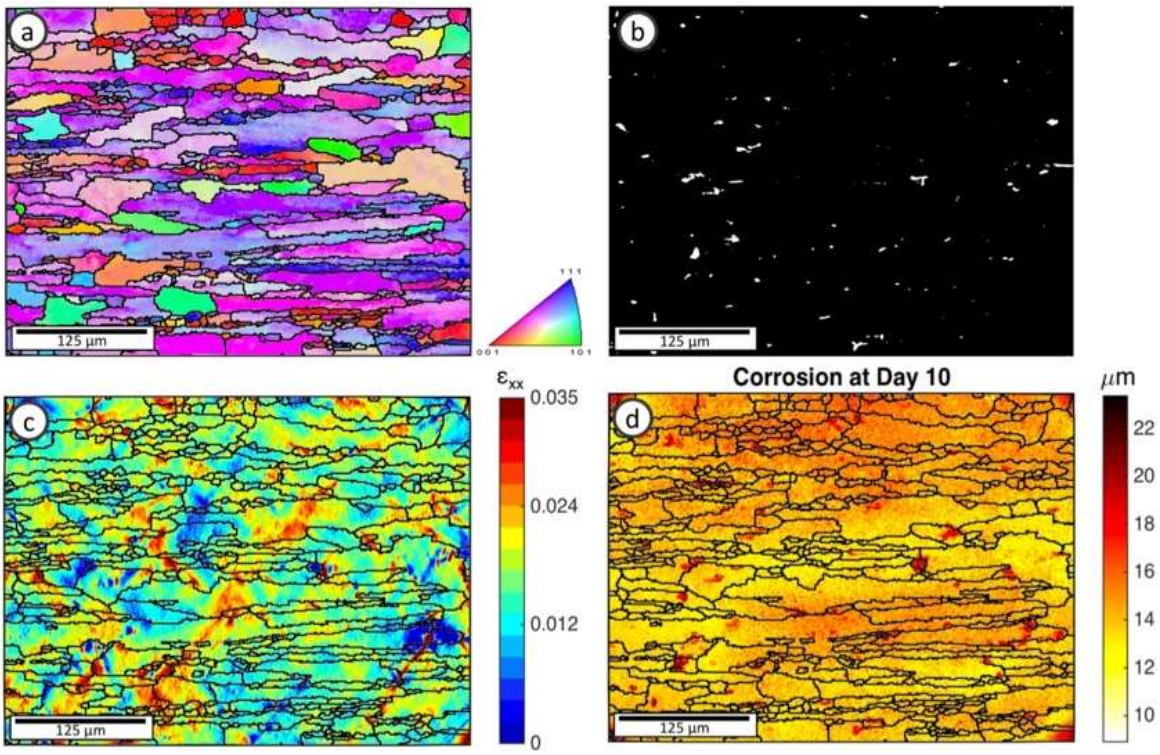

Fig 6.1 Characterization of a) the microstructure, b) the cathodic Al_7Cu_2Fe particles, c) the residual strain response and d) the surface roughness from corrosion (displayed for 10 days of corrosion on 3.5% NaCl solution).

To resolve sub-micron strains, a titanium nano-particle patterning methodology [46] was used to track deformation after a 2% tensile load with a residual strain of 1.56%. As with previous experiments, the loading rate was 2 mm/min and an extensometer was. The ROI was divided into 9 regions and separately scanned via SEM before and after deformation using 10 kV and a spot size of 4. The distortion correction protocol was used [89] and DIC was performed for each section with a subset size of 6.8 μm (111 pixels) and a step of 0.2 μm (3 pixels). The DIC outputs were stitched together for a full strain field view of the ROI, as shown in **Fig 6.1c** for ε_{xx}.

6.2.2 Galvanic Corrosion Assessment

After the strain field characterization, the specimen was gently polished to remove the titanium speckling. The specimen was then subjected to galvanic corrosion by coupling it to a SS316L cathode and submerging it in 0.6 M saline solution for 24 h periods, for a total duration of 20 days (480h). After each 24 h period, the sample was taken out of the solution, submerged in nitric acid (HNO_3) for ~10s to remove any corrosion product, cleaned with water, isopropyl alcohol, acetone, and methanol, and characterized for spatial pitting via CLSM (561 nm laser, 1μm z-step size, a 10x/0.45 objective) and SEM imaging (5.0 kV and a spot size of 3.0). To ensure a high resolution characterization of the surface roughness via CLSM, the pinhole size was adjusted to maximize the signal-to-noise ratio and the ROI was segmented into 20 areas. The characterized surface is shown in **Fig 6.1d** and exhibits localized pitting after 10 days of corrosion. All surface maps reconstructions of the corroded surface were quantitatively verified via lower-resolution optical profilometry and qualitatively verified using higher-resolution SEM imaging. Proper storage in-between characterizations ensured that the specimen remained dry and mechanically unaffected, therefore preventing any changes on the local electrochemistry and the local mechanics. Immediately prior to subsequent corrosion submersions, the specimen was cleaned a second time using the procedure described previously.

6.3 Results

The SEM scans in **Fig 6.2** show the evolution of corrosion every 5 days. Since the fiducial marks can still be seen after 20 days of corrosion, the surface seems to experience diffusion-controlled dissolution of the surface. Intergranular corrosion is not observed, and pitting is noticeable very early in the experiment with some areas corroding faster and wider than others.

The CLSM characterization in **Fig 6.3** shows that corrosion becomes significant at Day 10 with pits being about 10 µm deeper than the surface, with a pit near the center exhibiting a sizable growth at Day 15 onwards.

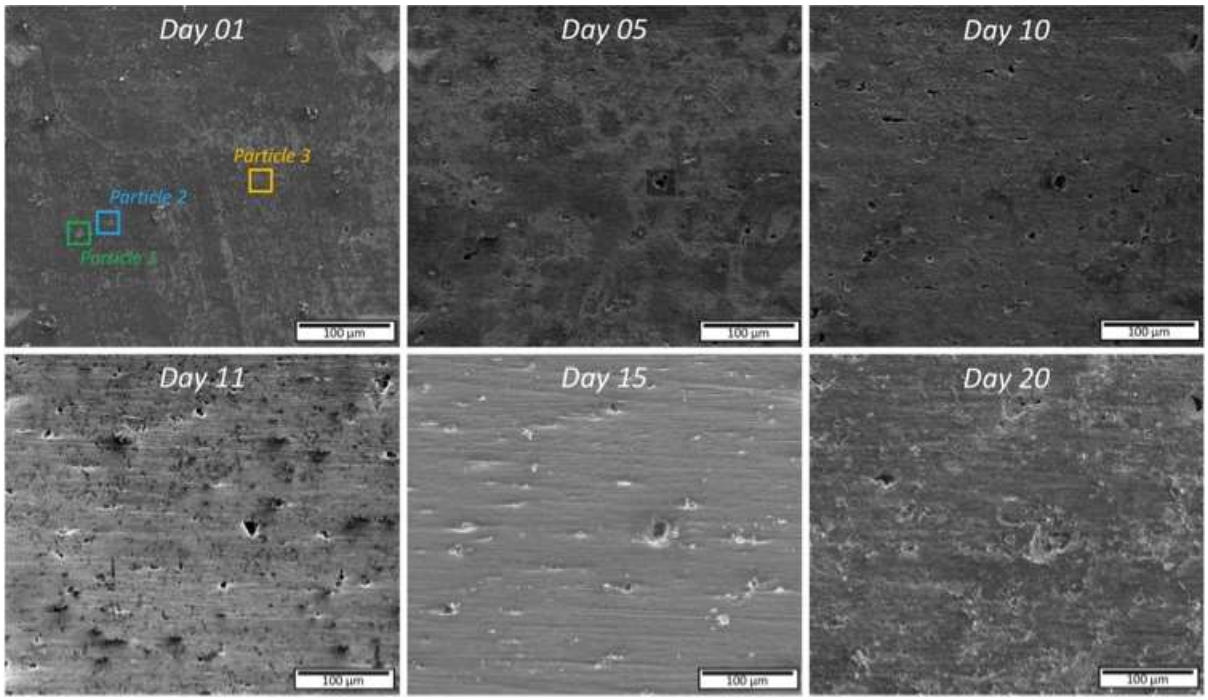

Fig 6.2 Overview of corrosion evolution within the ROI via SEM imaging, every 5 days.

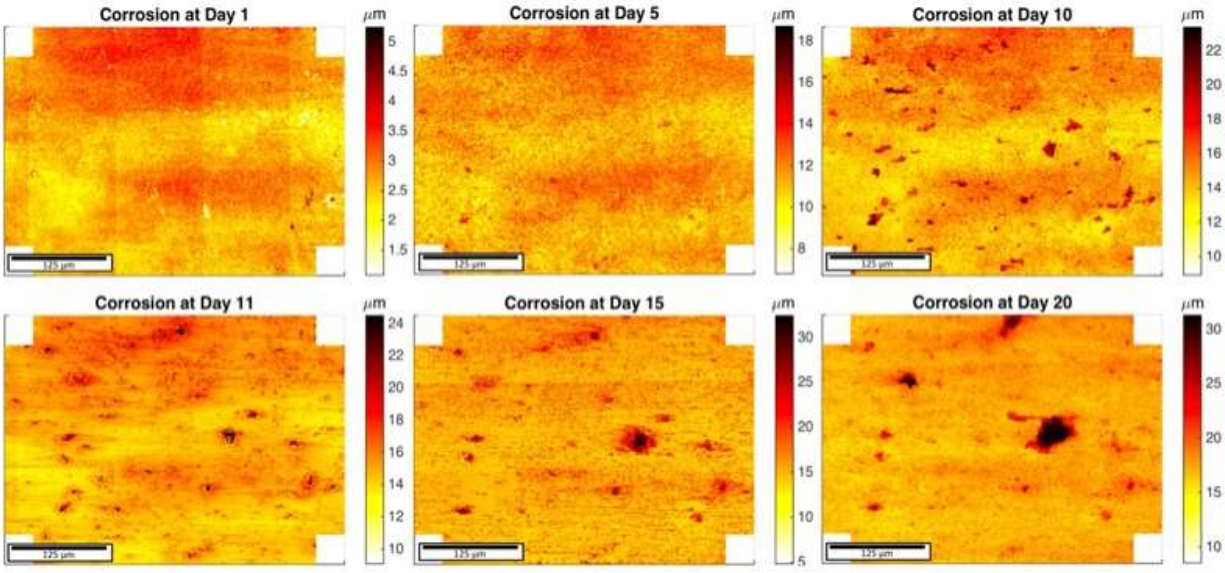

Fig 6.3 Overview of surface roughness evolution within the ROI via CLSM, every 5 days.

To track the behavior of areas affected by the local galvanic coupling, the ROI was segmented into particles and matrix using the EDX map seen in **Fig 6.2b** as a baseline segmentation mask. To ensure the proper separation of the areas affected by the local electrochemistry, the mask was dilated outwardly from the perimeter of the particles into the matrix with a threshold radius equal to the mean particle radius, 1.28 µm, based on a sensitivity analysis. This new mask was used to segment the axial strain map seen in Fig. 24c. The CDF in **Fig 6.4** indicates that particles have a low average strain but higher localized strains than the matrix. This is because the particles barely deform and instead transfer loads to the surrounding matrix.

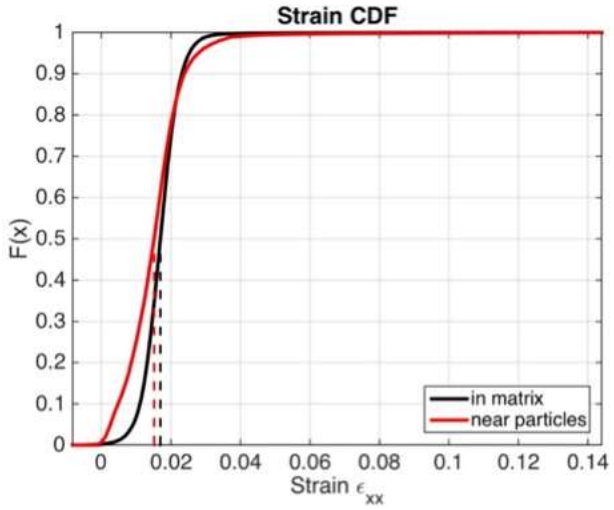

Fig 6.4 CDF comparison of the axial strain in the matrix (black) versus the axial strain at the particles (red).

Particles 1, 2, and 3 with an equivalent diameter of 7.46 µm, 8.34 µm, and 8.10 µm and a maximum local strain of 3%, 4%, and 7%, respectively, were tracked via SEM every day to pinpoint particle fallout, thus delimiting the days when the local electrochemical reaction between the particle and the matrix contributes to corrosion. **Fig 6.5**, **Fig 6.6**, and **Fig 6.7** show the evolution of particle 1, 2 and 3, with fallout occurring at Day 09, Day 08, and Day 05. These figures also show that corrosion on particle 1 and 2 does not significantly evolve after fallout, unlike particle 3 which evolves into a giant pit dominating the corrosion profile.

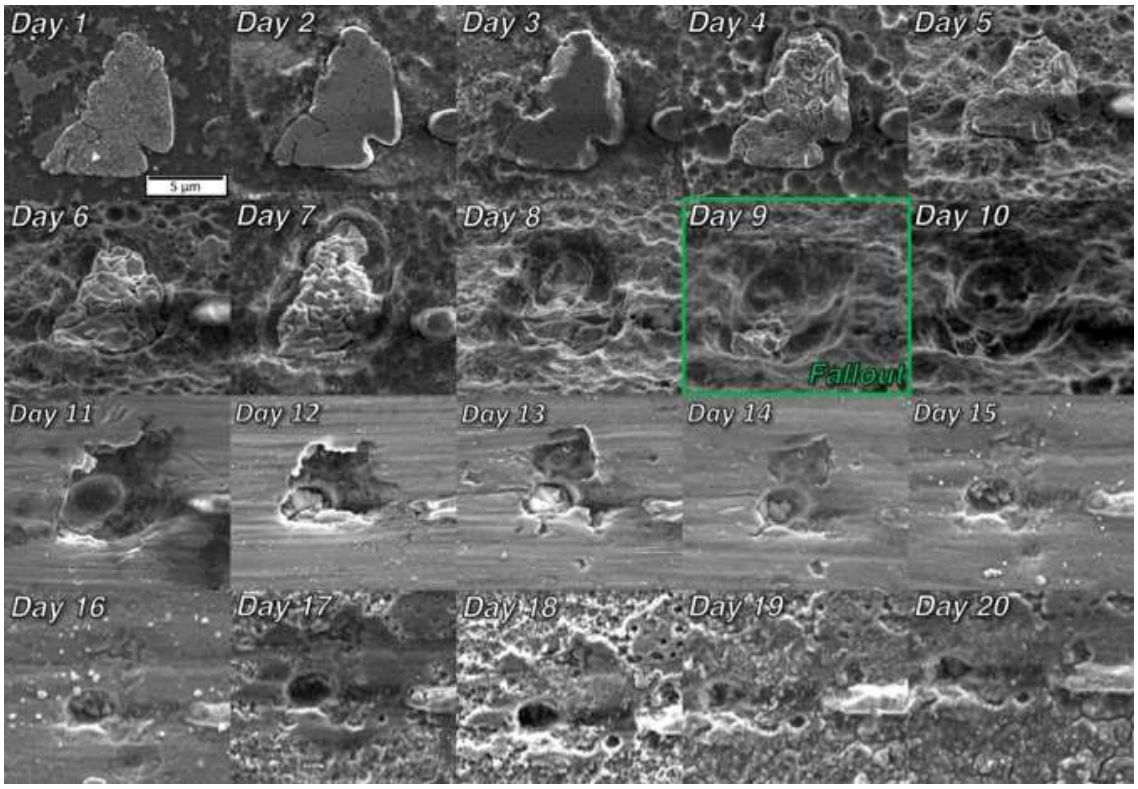

Fig 6.5 Corrosion evolution of particle 1 during 20 days of corrosion.

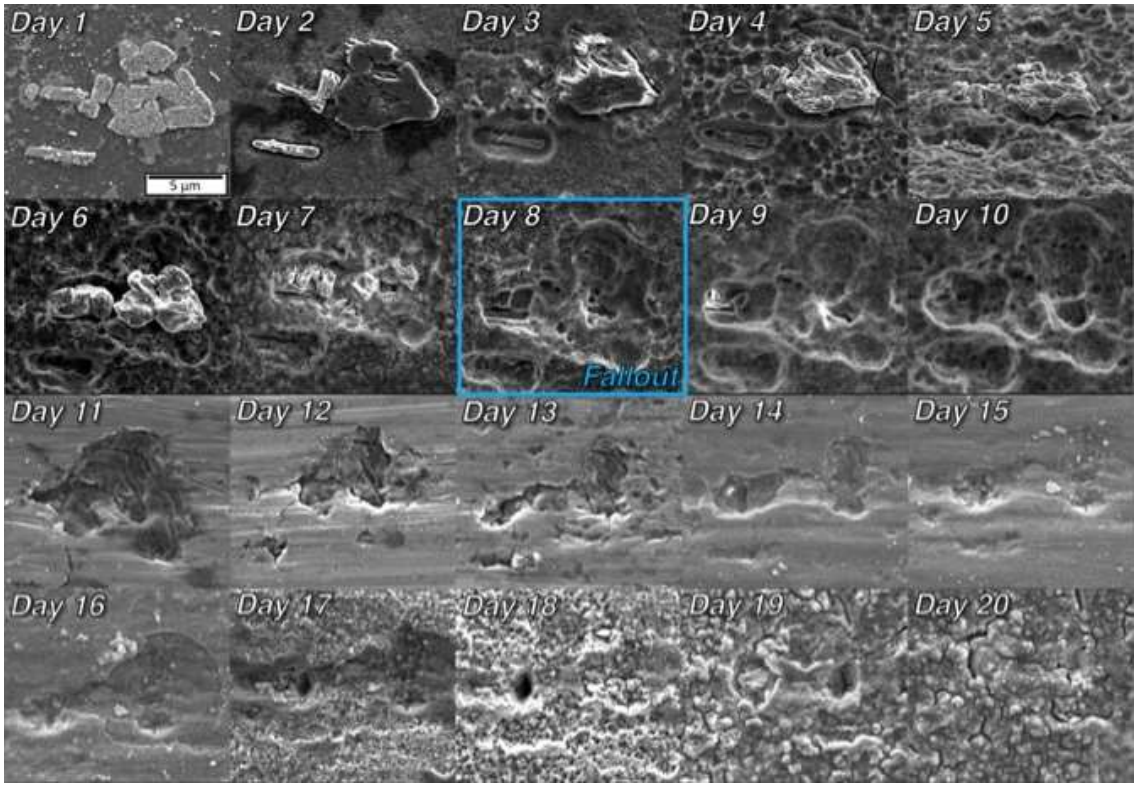

Fig 6.6 Corrosion evolution of particle 2 during 20 days of corrosion.

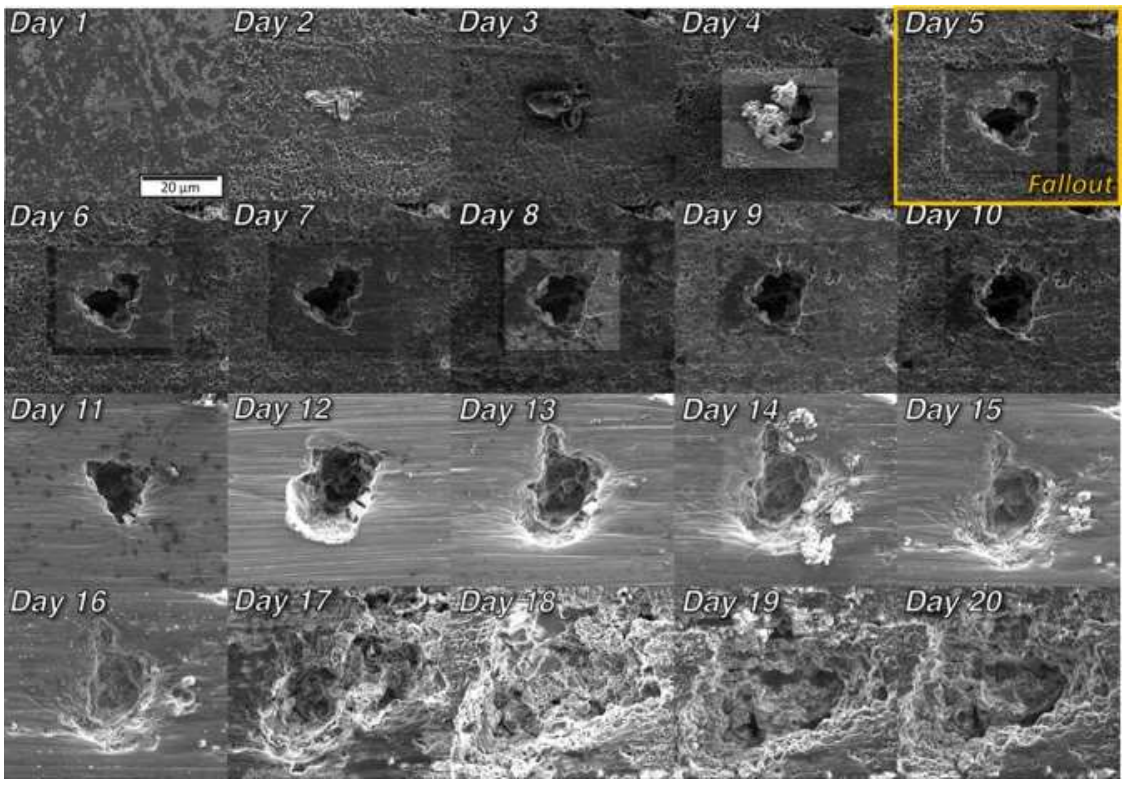

Fig 6.7 Corrosion evolution of particle 3 during 20 days of corrosion.

6.4 Discussion

As shown in

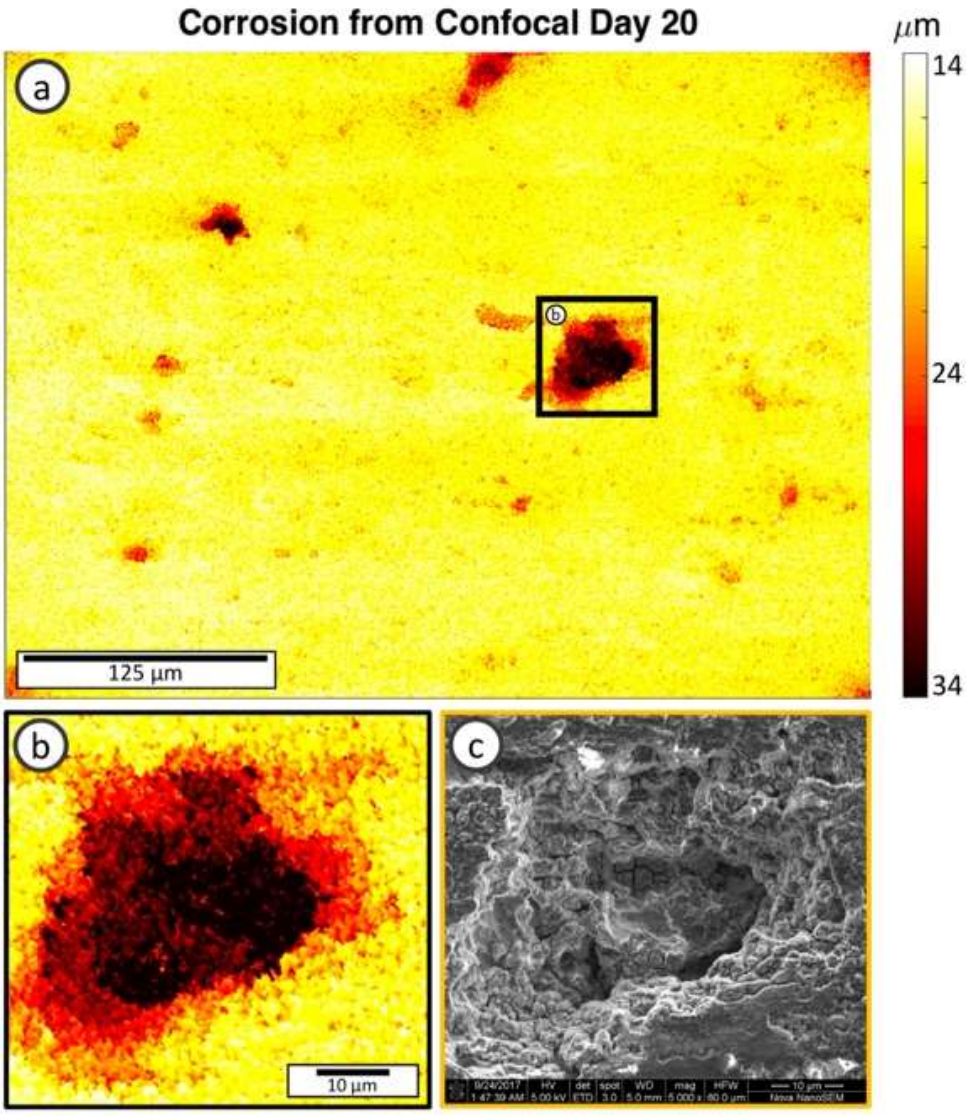

Fig 6.8, the pit at particle 3 that dominates the corrosion profile originally exhibited heavily localized strains as seen in **Fig 6.9**. This particle exhibits a maximum strain of 14% at the crack due to particle cracking (Fig. 32c), which diminishes down to 6% moving away from the crack. This localized strain is ~4x higher than the 1.6% macroscopic average residual strain of the specimen. The corrosion pit shows a final depth of ~34 μm on Day 20.

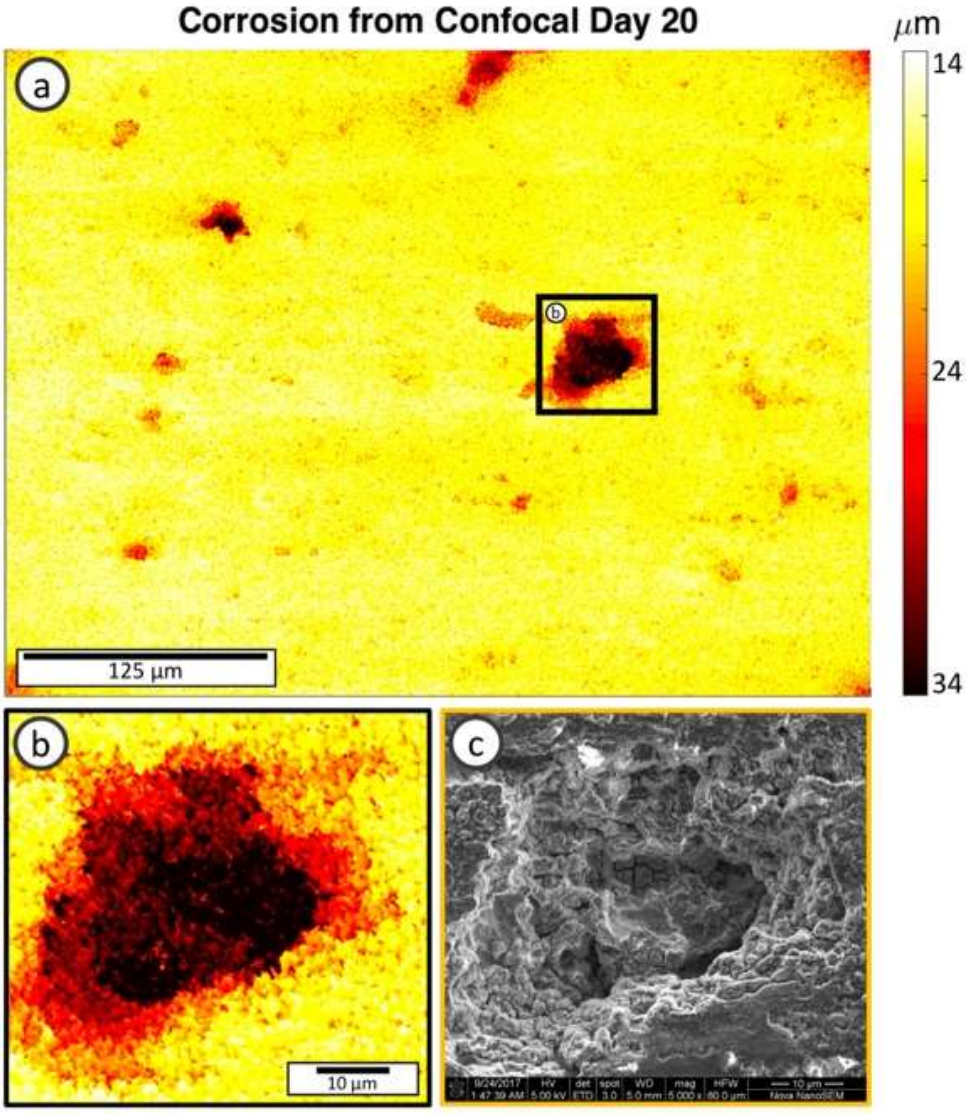

Fig 6.8 Overview of the worst pit after 20 days of corrosion, relative to a) the overall ROI, b) the surface topology (zoom-in region from (a)), and c) SEM imaging.

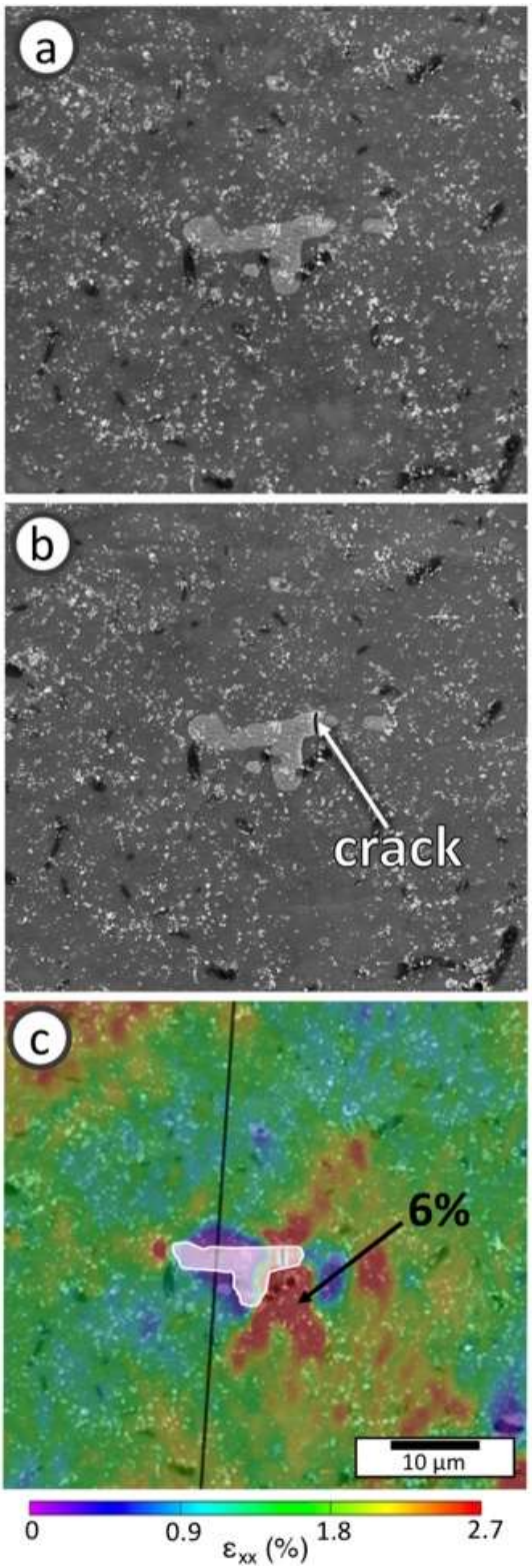

Fig 6.9 Overview of heavy pitting particle a) before loading, b) after loading (w/crack), and c) with localized strain.

To investigate how strain correlates to corrosion, the residual strains obtained from DIC for the entire ROI, shown in **Fig 6.1c,** were spatially compared to the surface topology maps for the entire ROI via a point-by-point statistical analysis to outline any trends between both parameters. Both maps contained a resolution of 0.12 µm over the 300 µm x 400 µm ROI. A principal component analysis (PCA) was performed using R [118] to determine the most representative variables from all the in-plane residual strains present in the material after loading to 2% strain and unloading, ε_{xx}, ε_{yy}, ε_{xy}, ε_1, ε_2 and the failure-prediction strains ε_{vm} and γ_{max} [96] The PCA analysis found that the longitudinal strain, ε_{xx}, and the shear strain, ε_{xy}, jointly covered ~86% of the data variation, thus capturing the shape and distribution of the data cloud. Therefore, only ε_{xx} and ε_{xy} are necessary during correlations.

Gaussian Process (GP) modeling [119] was used to infer a surface response of corrosion given localized strains, such that corrosion=f(ε_{xx},ε_{xy}). GP modeling takes into account spatial cross-correlations (the effect that the neighbors have on a point) by using covariance function kernels, which is of paramount importance for studying heavily localized data, like pitting. Since the characterization maps each contain over 9 million points, a special GP model utilizing Stochastic Variational Inferences (SVI) specifically designed for big datasets was used [120] alongside dataset batching and parallel solving. Any values beyond ±3σ were removed (~1000 points) to ensure a normal distribution and keep the allowable data ranges reasonable during fitting iterations. A Matérn 5/2 covariance kernel was used, along with a learning step rate of 0.2, 100 inducing inputs, and a batch size of 20,000. The GP-SVI results are shown in **Fig 6.10**.

The GP fitted response shows that high corrosion levels occur at the mean values of strain, ε_{xx} and ε_{xy}, with values of 1.6% and 0%, respectively, meaning that pure axial strain coupled with no shear strain exhibits higher corrosion. The GP response also shows that in general high strains do not translate into high corrosion levels and that their relationship does not change over time. Even high strains arising from a particle does not translate to any enhanced corrosion, as seen during the evolution study of particles 1 and 2 in **Fig 6.5** and **Fig 6.6**, both of which contained high strains in the periphery, yet they did not evolve into a significant pit. On the other hand, the axial strain at the particle that generated the dominating pit seen in

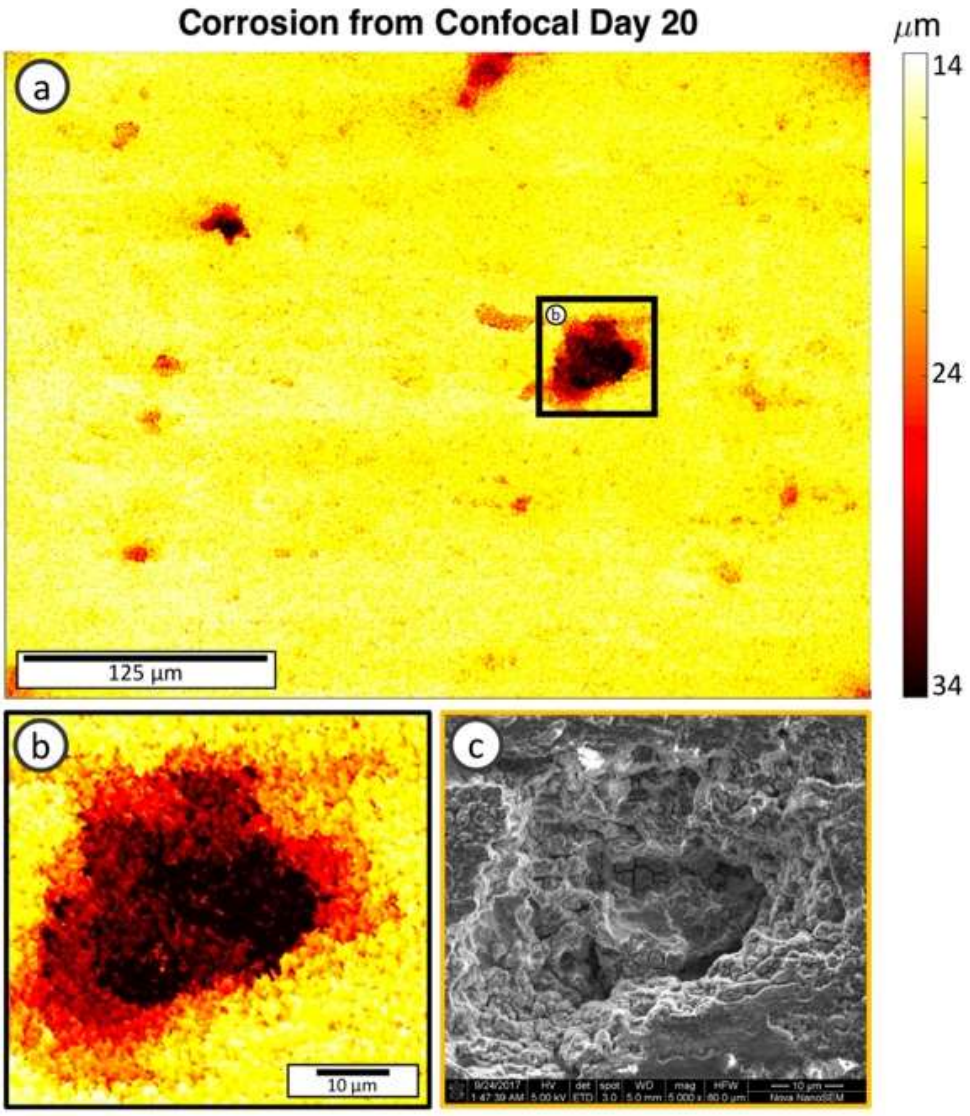

Fig 6.8 was ≥6%, almost twice the +3σ strain (3.5%) which meant its exclusion from the GP modeling. It should be noted that GP studies that included the information from this particle showed no difference from the results plotted in **Fig 6.10**, albeit they required more computational power. This was the only particle excluded since the rest had strains within ±3σ. It is also likely that the cracking is the source of the localized pitting seen during the early corrosion days.

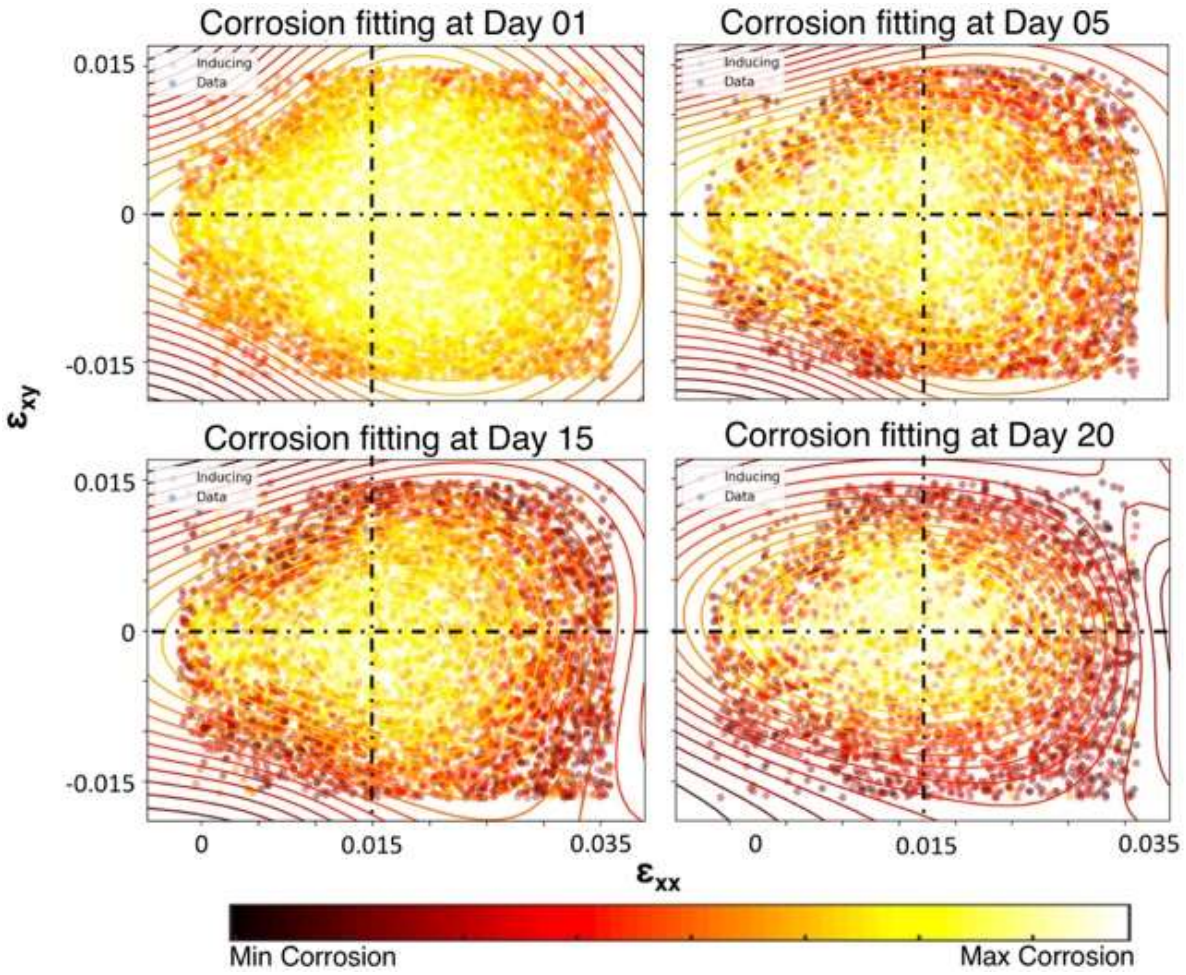

Fig 6.10 Corrosion trends relative to the longitudinal strain, ε_{xx}, and the shear strain, ε_{xy}, fit using Gaussian process modeling. The maximum corrosion values converge around the average strain values.

Particles 2 and 3 were part of the GP modeling and did not exhibit significant pitting. They developed pit growth when present, which slowed down after fallout. Since their cavities seem to blend with the matrix, a study of the difference between corrosion at the matrix and the particles is necessary. **Fig 6.11** shows a comparison of corrosion at the matrix (black) and the particles (red), using the segmentation procedure described previously during the strain study shown in **Fig 6.4**. It can be seen that at Day 03 both zones exhibit similar corrosion values, with corrosion at the particles growing deeper until all particles have fallen out (Day 09). After fallout the difference diminishes but corrosion at the particles remains deeper than the matrix, as seen in Day 12, Day 15, and Day 18. In other words, the particles leave cavities that corrode deeper than the average

matrix; however, the rate at which each grows varies, thus making necessary to identify the mechanisms behind the variations.

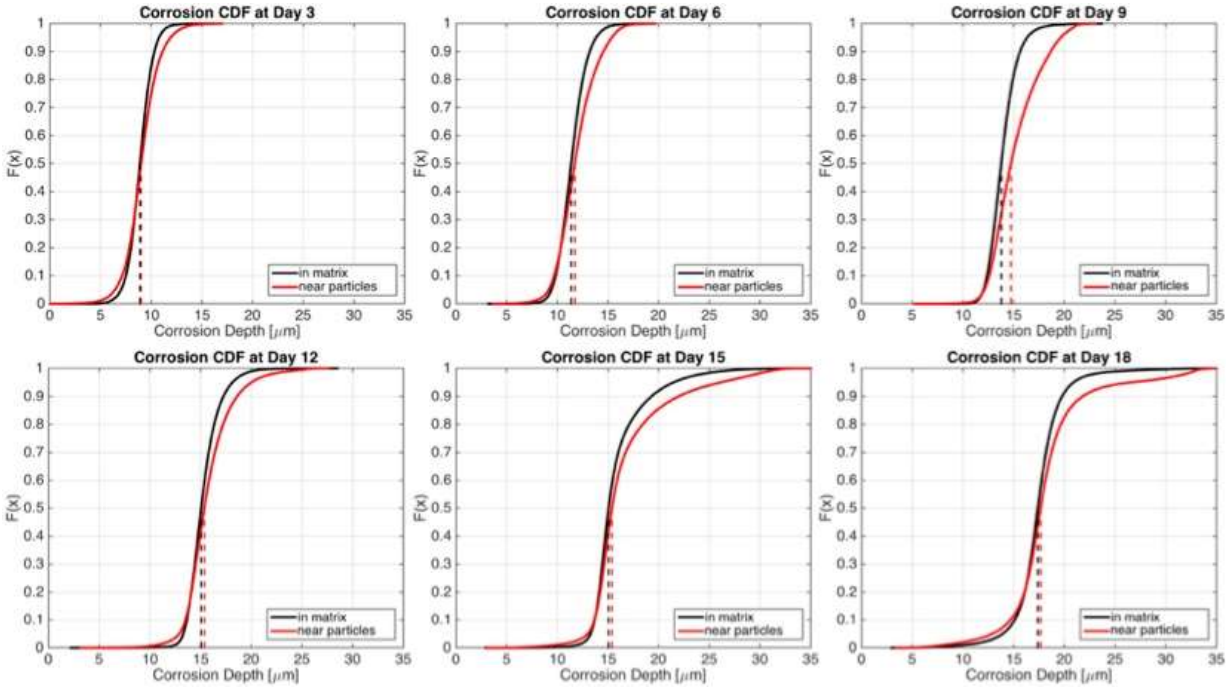

Fig 6.11 CDF comparisons of the corrosion on the matrix (black) versus corrosion at the particles (red). The mean corrosion near the intermetallic particles is deeper than at the matrix, especially after the particles fallout (day 09).

One postulated mechanism behind the rate of corrosion is the available surface area exposed to the electrolytes [121], which can be investigated by looking at the preexisting large voids on the lower right of the ROI (Figs. 25 and 26). These voids show slow corrosion, especially when compared to the particles, showing that although the exposed surface area affects corrosion, it has a slower corrosion rate relative to other mechanisms. Therefore, pitting happens at particles with accelerated growth up to particle fallout. Without the local electrochemical coupling between the cathodic particles and the matrix, the surface roughness and the high residual strains from cracking are the mechanisms driving localized corrosion. It is also possible that the interruption of the experiment may be affecting the rate of corrosion pitting, therefore on Chapter 7 and additional analysis of the effect that the interruption has on the corrosion response is performed.

6.5 Conclusion

- For strain values within ±3σ, the localized corrosion is independent from localized strains, and higher levels of strain do not translate into deeper corrosion pits. This has been verified by the surface response from GP modeling.
- A region with maximum strain caused by a particle that was cracked during loading exhibited accelerated pit growth, which eventually dominated the corrosion profile of the ROI. At this location, the strain values were much greater than +3σ.
- Cathodic particles have been verified to be the main source of corrosion pitting, which is statistically significant compared to the corrosion at the matrix. The evolution of pits is initially driven by the electrochemical interaction between the particle and the matrix and after particle fallout, corrosion is driven by both the diffusion-driven dissolution of the surface and the extreme residual strains from the cracking of the particle.

7. EFFECT OF STRESS CONCENTRATION RELATIVE TO THE MICROSTRUCTURE ON CORROSION

7.1 Introduction

The role of preexisting stresses on corrosion has also been studied macroscopically, however, given the varied results observed in literature [35], a properly controlled experiment is needed to ascertain the role of plastic deformation and the associated stress state at the appropriate scale, to avoid gross homogenization. As seen in **Chapter 4**, for 2.5D simulations of different orientations of rolled AA7050 material, the TS direction yielded more accurate results relative to experimental measurements due to the minimized subsurface uncertainty. In **Chapter 6** it was found that the evolution of pitting is initially driven by the electrochemical interaction between the cathodic particles and the matrix, and once all particles experience fallout, pitting is driven by both the dissolution of the surface and the extreme values of the residual strains from particle cracking. The quantitative comparisons of the local residual strains and the corrosion morphology demonstrated that, for the material in general, the corrosion mechanism is not directly related with the local stored residual strains. However, it is well known that an actively loaded component may be subject to stress-enhanced corrosion, which leads to the question if corrosion pitting could be a stress-driven mechanism. In other words, galvanic corrosion may be affected by the active dislocation accumulation in the material instead of just the residual plasticity.

This chapter investigates stress-driven corrosion on a AA7050-T7451 specimen under constant loading at different corrosion exposure periods. The different exposure times as well as the cleanup protocols are designed to give a full understanding of the effect that both particle fallout and passive layer disruption have on pitting. Before corrosion, the microstructure, strains, and particles are characterized via EBSD, DIC, and EDS, respectively. To obtain the stresses an EVP-FFT model is generated from the EBSD characterizations, where the subsurface uncertainty is minimized as described in **Chapter 5**. This chapter will provide a more complete view of the effect that the local microstructure and mechanical behavior of the material has on corrosion.

The mechanical testing in this chapter as well as the EBSD scans were performed by Dr. Alberto Mello, with the rest of the characterizations, modeling, and data analyses being performed by the author. A complete description of this chapter can be found in: *A. Nicolas, A.W. Mello, M.D. Sangid, Relationships between microstructure and micromechanical stresses on local pitting during galvanic corrosion in AA7050, Corr. Sci. (2019). Accepted.*

7.2 Materials and Methods

7.2.1 Materials

Three specimens 1.25 mm thick were cut in the TS direction via electro-discharge machining (EDM) and polished down to 800 grit using SiC paper to prevent any stress concentrations from an uneven surface. A new geometry was designed according to ASTM E8 [100] tensile standards with a gauge size of 20 x 5 x 1.25 mm and an overall specimen length of 90 mm. A 300 μm x 400 μm ROI was delimited at the center of the specimen via fiducial marking. As a visual orientation aid, two larger marks were placed at the lower left corner of the ROI. The microstructural characterization of the ROI was performed via EBSD. Additional specimen preparation was performed immediately before EBSD scanning. First, the specimens were slightly polished for an extra 30 s with 0.05 μm colloidal silica to remove the oxide layer. Afterwards, the surface was cleaned with distilled water on a NAPPAD cloth to remove the leftover silica.

7.2.2 Microstructure and Particle Characterization

Once the specimen was cleaned and placed inside the SEM chamber, the ROI was located via the fiducial markings and EBSD scanning was performed. The final Inverse Pole Figure (IPF) maps along with the grain boundaries are shown in **Fig 7.1** for each of the three specimens. EDS was used to spatially locate the Al_7Cu_2Fe cathodic particles in the ROI. The mean and maximum particle diameters for all three specimens were 1.66 μm and 12.1 μm, respectively.

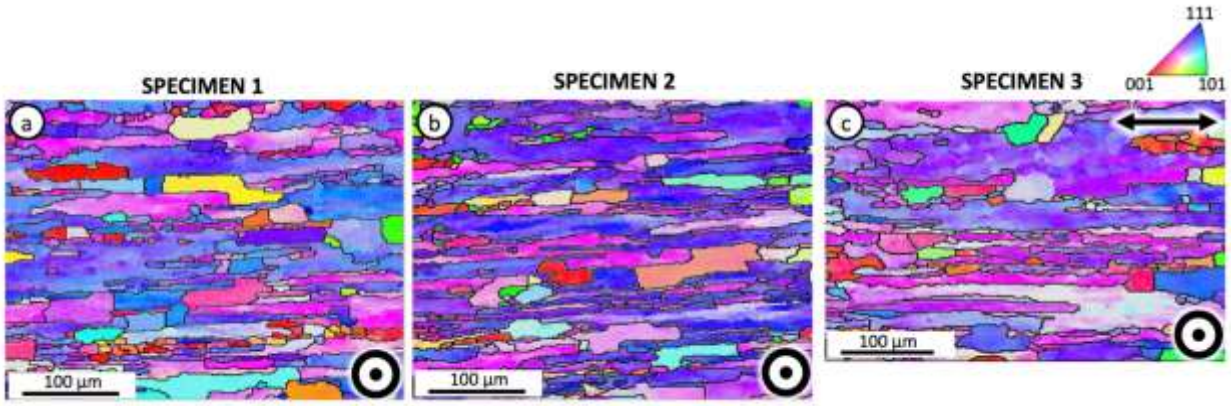

Fig 7.1 Inverse Pole Figure (IPF) orientation maps for a) Specimen 1, b) Specimen 2, and c) Specimen 3 on the TS direction, with the rolling direction being perpendicular to the page. The upper right arrow shows the loading direction.

7.2.3 Experimental Procedures

7.2.3.1 Mechanical Procedures

DIC was performed using gold nanoparticle (AuNP) speckling of the surface with an average diameter of 100 nm, following the procedure in [88]. SEM imaging of the ROI with AuNP speckling was performed with a 5 kV accelerating voltage, a spot size of 2, and a 5 mm working distance. Three cathodic particles per specimen inside the ROI were scanned at 10,000x magnification, with an extra (fourth) particle being scanned within Specimen 2 at 4,000x magnification, since the particle partially fell out of the matrix and is surrounded by a larger cavity. A total of 10 particles were studied overall. Each ROI was segmented into 9 separate subsections with a 20% overlap and scanned at 1,500x. Stitching of the 9 speckled subsections was manually performed twice for each specimen: from left to right, and from right to left to improve DIC at the edges of the subsections.

All specimens were loaded to 2.5% total strain at a rate of 0.15 mm/min and elastically unloaded to nominally zero applied load, using a servo-hydraulic load frame with MTS 647 hydraulic wedge grips. The macroscopic strain was measured with an Epsilon extensometer Model 3542. **Fig 7.2** shows the resulting macroscopic stress-strain curves for all three TS specimens. The deformed AuNP speckle patterns of all 10 cathodic particles and 3 full ROIs were scanned ex-situ via SEM using the same scanning settings discussed above and were used for DIC using a window subset of 35 pixels (1.2 μm) and a step size of 2 pixels (70 nm) for the particles, and a subset of 71 pixels (5 μm) and a step size of 2 pixels (140 μm) for the ROI subsections. Afterwards the distortion correction protocol described in [89] was applied. The final corrected strain field maps for the ROI and particles of each Specimens 1, 2, and 3 can be seen in **Fig 7.3**, **Fig 7.4**, and **Fig 7.5**, respectively.

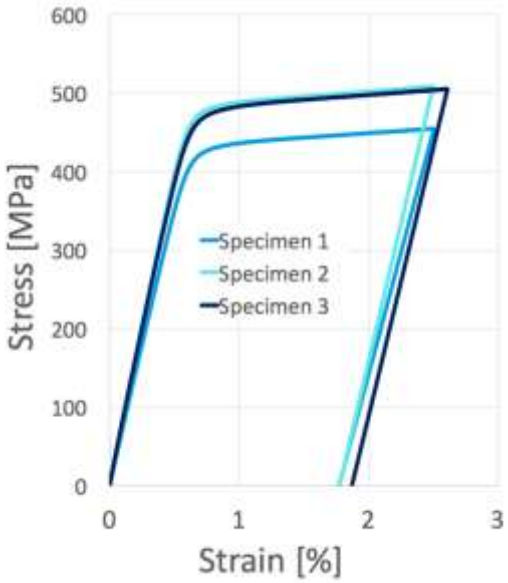

Fig 7.2 Macroscopic stress-strain curves for all three TS specimens after being loaded to 2.5% total strain and unloaded with 1.8% macroscopic residual strain.

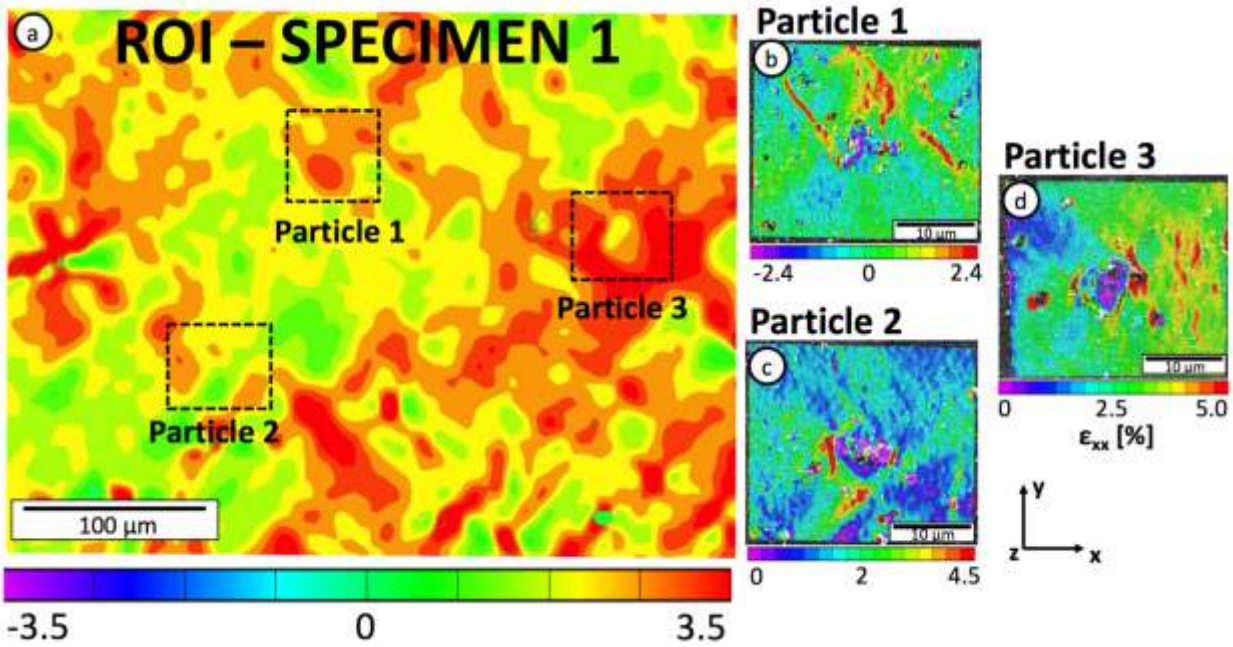

Fig 7.3 Experimental residual strains for the axial direction (ε_{xx} [%]) for Specimen 1 obtained via DIC at 1,000x. The ROI (a) averages to 1.8% strain, which is the macroscopic residual strain of the specimen. The smaller speckle pattern at 15,000x allows higher resolution analysis of strains around the particles (b, c, and d).

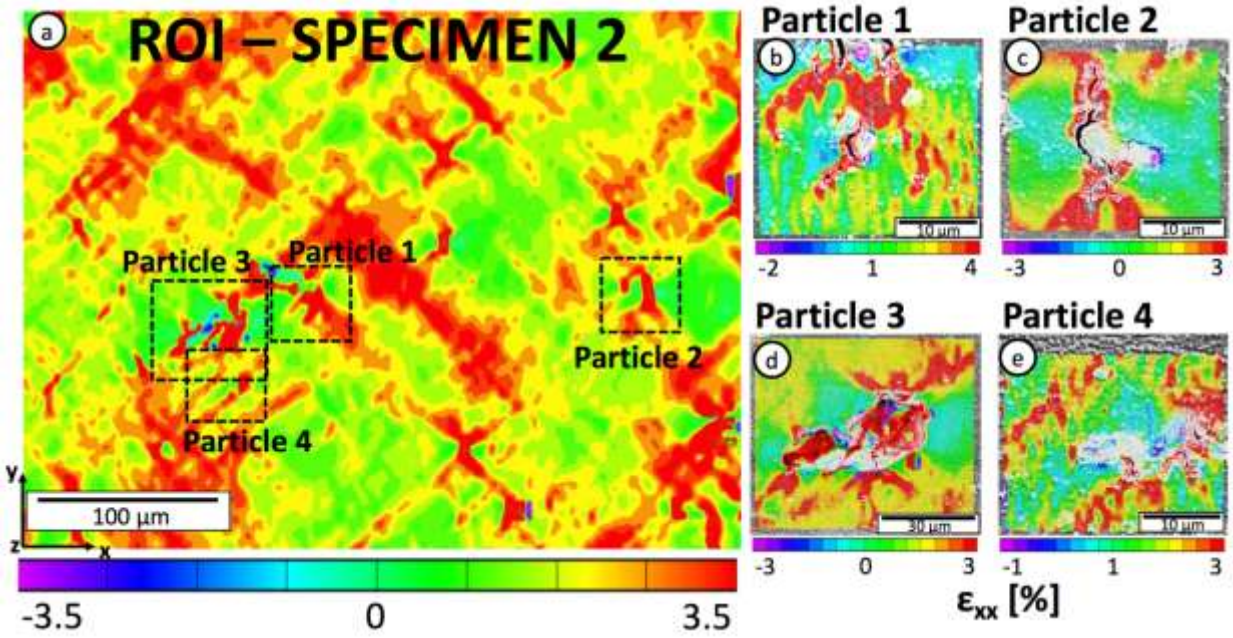

Fig 7.4 Experimental residual strains for the axial direction (ε_{xx} [%]) for Specimen 2 obtained via DIC at 1,500x. The ROI (a) averages to 1.8% strain. Due to polishing before speckling (necessary to remove the oxide layer), Particle 2 (c) experienced partial fallout, hence the cavity observed.

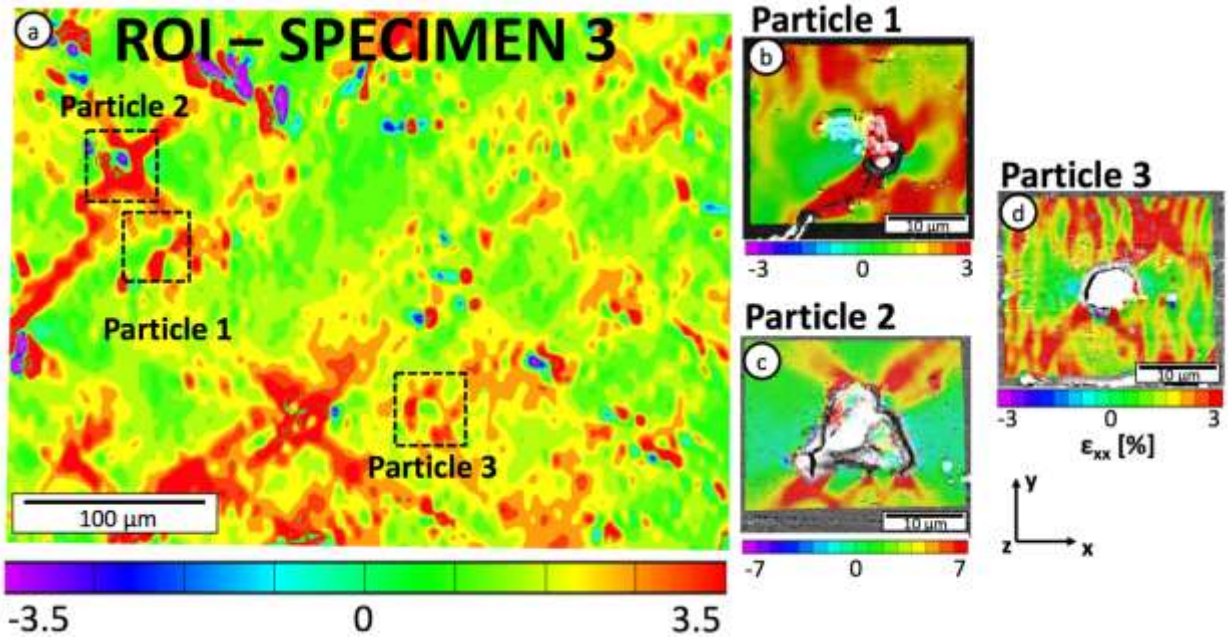

Fig 7.5 Experimental residual strains for the axial direction (ε_{xx} [%]) for Specimen 3 obtained via DIC at 1,500x. The ROI (a) averages to 1.9% strain which is the macroscopic residual strain of the specimen. Particle 2 (c) exhibits cracking at the neighboring matrix along with slip system activation emanating from said cracks.

To ensure that during corrosion only the cathodic particles and the matrix are interacting with the corroding environment, the AuNP particles were removed from the surface by polishing the surface of each specimen with 0.05 μm colloidal silica for 1 minute and rinsing them with distilled water. The complete removal of the gold speckling was confirmed with optical microscopy at 20x.

7.2.3.2 Electrochemical Analysis

To study stress-mediated localized corrosion of the pre-strained and mapped specimens, it was necessary to corrode the material under maximum loading, which required designing a special chamber that allowed for corrosion of only the gauge section while applying an external load on the specimen. This chamber was limited by two factors: i) fitting a piece of stainless steel inside the chamber to act as a cathode in the closed system with the anodic aluminum, covering only the gauge section of the specimen and ii) the need to measure the current/voltage daily without interrupting the corrosion experiment. The final design utilized a 0.51 mm diameter SS316L wire protruding out of one wall of an 8 mm x 12.8 mm x 9 mm plastic chamber, while connected to a SS316L, M6 screw inside the chamber with a surface area of ~12.57 mm. The design of this chamber permitted an externally couple of the AA7050 specimen to the steel screw via the steel wire, while measuring the current/voltage of the specimen, where the multimeter closes the loop by being in constant contact with both the steel wire and the AA7050 specimen. The chamber was filled with aerated 3.5 wt.% (0.6 M) NaCl solution at 5.6 pH, which remained at that constant pH since the chamber was continuously filled with fresh saline solution at all times. It should be noted that the stainless steel cathode is not required for corrosion to occur; however, it is necessary for a realistic representation of the environmental exposure usually encountered in AA7050 frames.

To statically load the specimens for long periods of time, a 6.7 kN electromechanical Mark-10 ESM-1500 force test stand was used. This force indicator has a ±0.1% accuracy with a resolution of 5 N. Each sample was reloaded to their peak stress, as observed in **Fig 7.2** (455 MPa for Specimen 1, 508 MPa for Specimen 2, and 506 MPa for Specimen 3). Once the material was reloaded back to peak stress, the sample was held in displacement control. Slight stress relaxation was observed during the hold time, which was nominally 5% load drop throughout the corrosion schedule. The load was monitored throughout the test and, if the stress dropped below the initial

yield point of the material of 443 MPa (as seen in the mean yield stress TS values found in [110]) the experiment was reloaded back to the target stress by a control system. The final assembly of the chamber and the specimen can be seen in **Fig 7.6**.

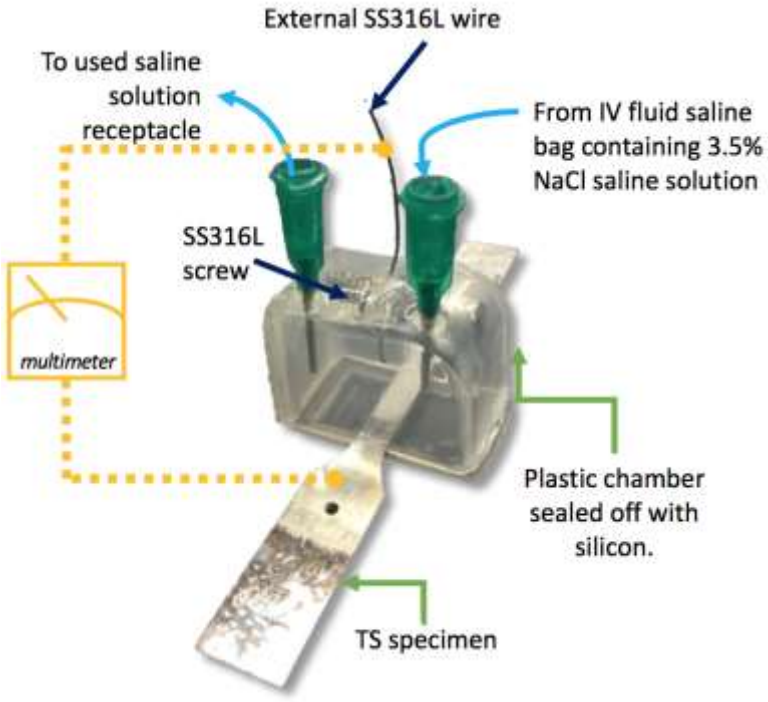

Fig 7.6 Overview of the corrosion chamber used to corrode the gauge section of the TS specimens. A multimeter was used at the beginning and end of the experiment to measure current/voltage.

Chapter 6 displayed particle fallout occurring around day 8 of corrosion, which corresponded to a highly localized corrosion morphology. Therefore, to investigate the corrosion of AA7050 around particle fallout, three different specimens were subjected to different corrosion intervals that revealed the behavior of the material up to particle fallout at Day 8. To investigate the effect that the removal of both the corrosion products and the passive layer have on the evolution of corrosion, two specimens were cleaned after reaching their targeted interruption schedule of the corrosion experiment with nitric acid (HNO_3) for 10s, followed by an ultrasonic cleaner using distilled water, isopropyl alcohol, acetone, and methanol to reset any built up passive layer/corrosion product, whereas one specimen was left to corrode uninterruptedly for the entire corrosion experiment. All specimens experienced ultrasonic cleaning twice: once before any surface characterization, and again immediately prior to being loaded in the corroding chamber.

A total of three specimens, Specimen 1, 2 and 3, were corroded for a total of 6, 7, and 8 days, respectively, with Specimen 1 experiencing an interruption at Day 2 and Specimen 2 experiencing an interruption at Day 5. That is, Specimen 1 was corroded without interruption under constant loading for 2 days (aiming for analysis before particle fallout), Specimen 2 was corroded without interruption for 5 days (aiming for an imminent particle fallout), and Specimen 3 was corroded without interruption for 8 days (aiming for analysis after particle fallout) which was the day when material failure occurred on Specimen 3. To investigate the differences between interrupted and uninterrupted corrosion of AA7050, Specimens 1 and 2 were reloaded and exposed to corrosion for a second time until material failure occurred, which happened at Day 6 for Specimen 1 and at Day 7 for Specimen 2. It should be noted that all specimens failed in the corroded region inside the chamber but outside the ROI, thus not affecting the subsequent characterization. A summary of the corrosion lengths per specimen can be seen in **Fig 7.7**.

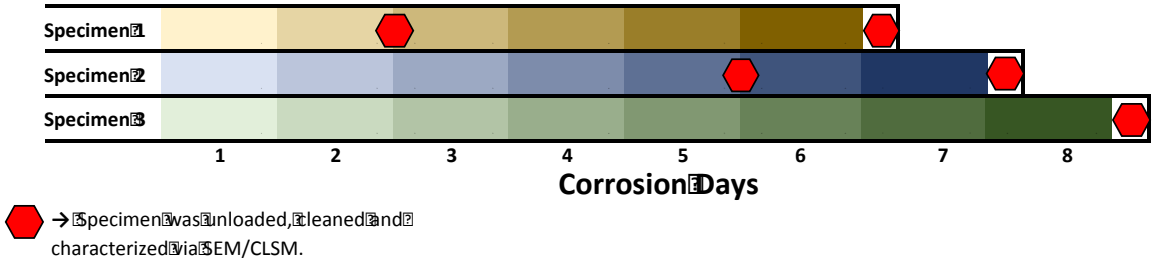

Fig 7.7 Summary of corrosion lengths per specimen, showing interrupted corrosion for Specimen 1 and Specimen 2, and uninterrupted corrosion for Specimen 3. Particle fallout tends to occur around Day 5, as seen in Chapter 6.

After each corrosion period, the surface was cleaned via sonicating and its morphology was characterized both qualitatively and quantitatively via SEM and CLSM [122]. For the qualitative characterization, SEM was performed using a FEI Nova NanoSEM 630 microscope with a 15 kV accelerating voltage, a spot size of 3, 5 mm working distance, no tilt, a 700x magnification for the ROI and a 15,000x magnification for the particles (except the particle that had experienced fallout prior to loading corrosion within Specimen 2, which was scanned under 10,000x magnification). For the quantitative characterization, CLSM was performed using a Zeiss LSM 880 upright Confocal Microscope with a 561 nm laser wavelength, a Plan Apochromatic

10x/0.45 objective, a step size of 1 μm in the z-direction, and a resolution of 0.10 μm in the x-y directions.

7.2.4 Simulation Procedures

The surface orientation files obtained via EBSD, along with the constituent particles characterized via EDS were used as input to create analogous EVP-FFT models for all three specimens. The gridification and the matching of the grain orientation coordinate system and spatial coordinate systems of the EBSD data was performed using DREAM3D [107], where the grain orientation coordinate system was rotated 90° about the <001> direction to match the spatial frame. The spacing between data points in the computer models was delimited by the EBSD scan step size of 1.5 μm. The final surface data containing the grains, the different phases, and the Euler angles was exported into a single h5 file per specimen.

An equivalent 3D subsurface microstructure with elongated grains was statistically reconstructed with the methodology described previously in **Chapter 5**. Statistically equivalent 3D particles are randomly added to the subsurface reconstruction, both within the grains and at the grain boundaries, following their aspect ratios, major axis dimension, and space distributions, where the particles have a tendency to cluster in the rolling direction [22], based on an experimental dataset of particles in AA7050 measured from an XCT study [80]. Following the aspect ratios in [80], where the space distributions were delimited by enforcing distances between the ellipsoid centroids, the surface particles characterized via EDS were allowed to grow into the material in an elongated manner. The final particle volume fraction of both the EDS elongated particles and the statistically reconstructed particles was ~0.7% of the full reconstruction, which was enforced to match the experimentally observed volume fraction of XCT. A full view of a 3D microstructure with statistically reconstructed subsurface grains and particles can be observed in **Fig 7.8**.

Finally, a dummy gas phase was added to all surfaces not subjected to macroscopic loading to decouple the material from the periodic boundary condition. The surfaces onto which the loading conditions were applied had extra solid material added to comply with the periodicity

requirements. The entire microstructure was then modeled via EVP-FFT following the loading history of the experiments, where specimens were macroscopically loaded to 2.5% strain, unloaded to near zero macroscopic stress corresponding to ~1.8% strain, and reloaded back up to ~2.5% strain. The AA7050 matrix was modeled elasto-plastically and the particles were modeled as purely elastic using the isotropic material properties from [117], since the Al_7Cu_2Fe particles are brittle. A summary of the elastic and plastic material parameters for both the matrix and the particles can be seen in **Table 3.1** and **Table 3.2**. Each virtual microstructure was defined by a 512 x 512 x 64 voxel (1 voxel = 1.5 μm) computer model and simulated using the EVP-FFT parallelization method.

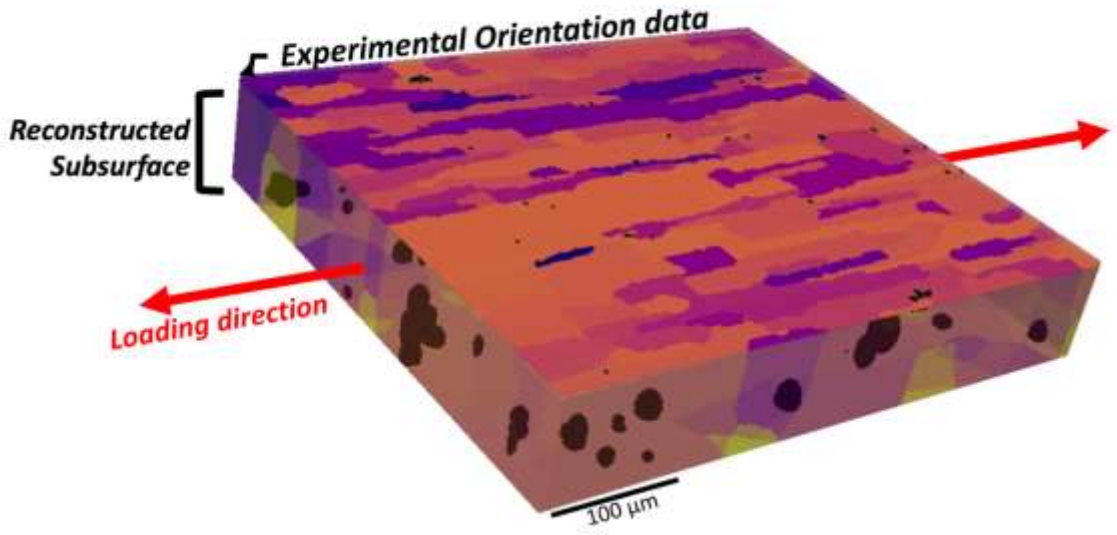

Fig 7.8 EVP-FFT reconstruction for Specimen 1, with statistically equivalent subsurface grains reconstructed from the original experimental orientation map (unique colored 1102 grains total) [123] and statistically equivalent cathodic particles (plotted in black) reconstructed from the microtomography data from [80].

7.3 Results

7.3.1 Corrosion Morphology Results

The SEM scans shown in **Fig 7.9, Fig 7.10**, and **Fig 7.11** depict the evolution of corrosion at the tracked particles for Specimens 1, 2 and 3, respectively, alongside the initial microstructure and the types of grain boundaries (in terms of misorientation angle) present near the particles before they were exposed to a corrosive environment. Although each specimen experiences

different corrosion periods, all specimens exhibit corrosion at grain boundaries as well as electrochemical attack at the cathodic particles. This is in contrast with previous results showing that no significant grain boundary corrosion was present when a pre-strained specimen was corroded in unloaded condition [123].

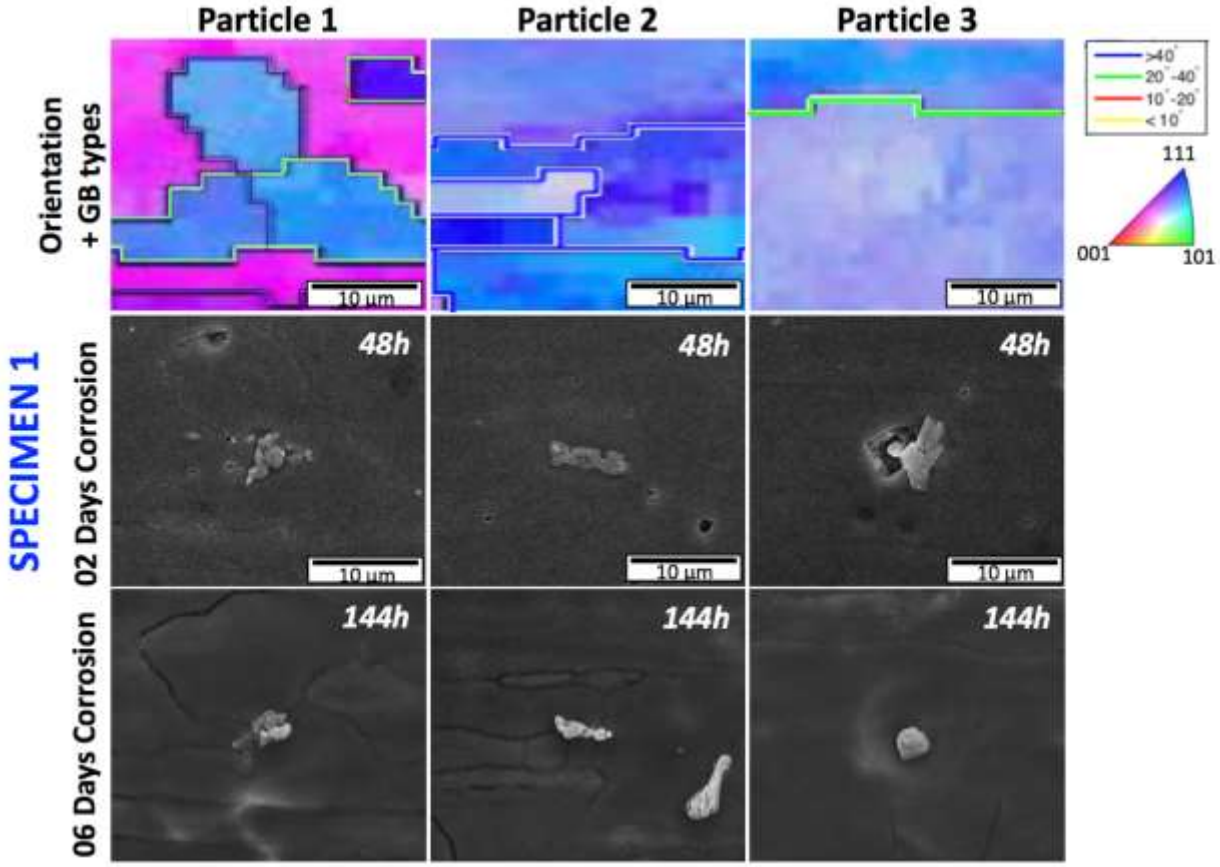

Fig 7.9 Corrosion overview of particles studied for Specimen 1. Intergranular corrosion and incomplete fallout is observed.

Specimen 1 in **Fig 7.9**, which was corroded initially for 2 days, shows slight intergranular corrosive attack, which becomes severely pronounced after another 4 days of corrosion. The matrix also shows signs of localized attack from the cathodic particles after only 2 days of corrosion. However, once the specimen was subjected to an additional 4 days of corrosion, not only are the particles exhibiting degradation thus revealing lower portions of their elongated geometry, but also the surface recession of the matrix starts to reveal underlying cathodic particles, which can be observed by the sudden appearance of a new particle located on the lower right section of the

image for Particle 2. Since the particles are still present in the material, localized corrosion is still taking place after 6 days of corrosion, as can be seen in the image for Particle 3. It should be noted that Particles 1 and 2 are located at a grain boundary, and Particle 3 is located inside a large grain. None of these particles, however, were located at or near low-angle or coincident site lattice boundaries.

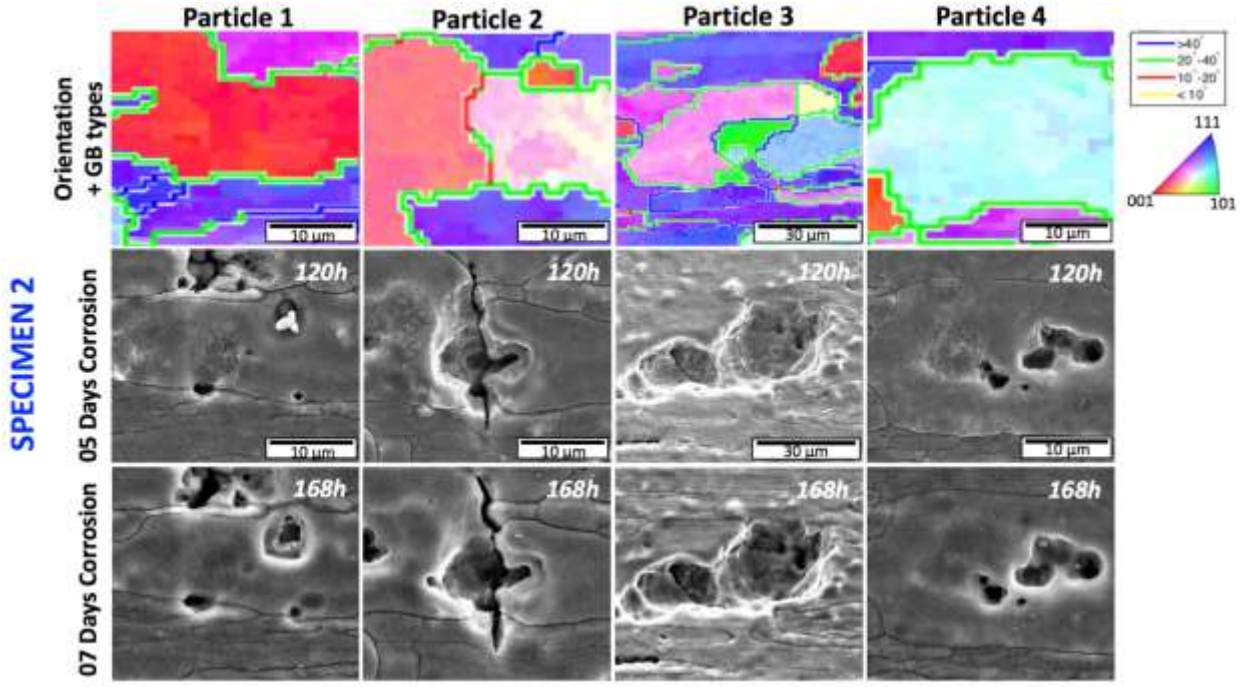

Fig 7.10 Corrosion overview of particles studied for Specimen 2. Intergranular corrosion is observed, along with a smoother corrosion and complete particle fallout.

Specimen 2 in **Fig 7.10,** which was corroded initially for 5 days, shows significant intergranular corrosion attack with very slight increases in depth after being exposed to another 2 days of corrosion. After 5 days of uninterrupted corrosion, all the studied particles have experienced fallout, leaving localized corrosion features of varying depths. The former location of Particle 1 and Particle 3, which were located inside fairly large grains, can be pinpointed by the shallow cavities in the center of each image, both of which exhibit slight roughness in their inner surface. After 2 more days of corrosion, the only appreciable difference observed is the smoothing of these inner surfaces, as well as the slight growth of the small cavities in the vicinity of the particles. Particle 3, which had experienced partial fallout even before exposure to corrosion, due

to the polishing and cleaning of the material, shows a complete disappearance of any leftover particle fragments after 5 days of corrosion, leaving behind a large cavity with a complex morphology. After being exposed to another 2 days of corrosion, the cavity shows slight growth as well as smoothing of its inner surface. It is interesting to observe that the intergranular corrosion near or inside this cavity becomes much more pronounced and would potentially aid in the degradation of their respective grains. Particle 2, which was located on a low-angle grain boundary (<15° misorientation), not only evolves into a deep corrosion pit after 5 days of corrosion, but also develops intragranular cracking of the adjacent grains. After 2 additional corrosion days, the pit from this particle is observed to significantly grow both in depth and in width, with erosion of the grain boundary becoming clearly distinguishable.

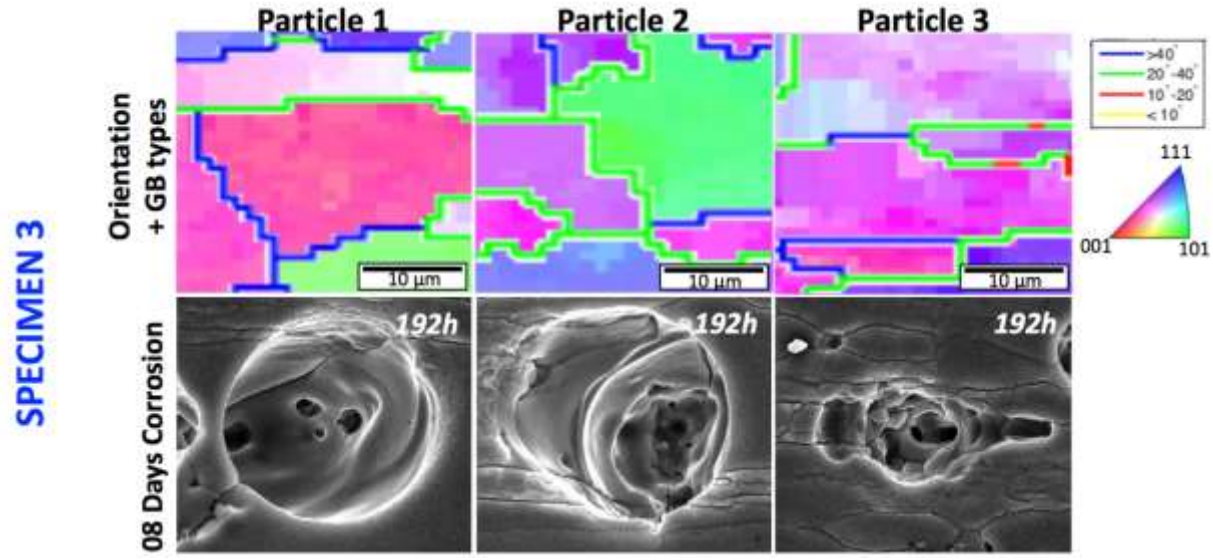

Fig 7.11 Corrosion overview of particles studied for Specimen 3. Not only is complete fallout observed but, also heavy pitting and grain degradation is observed on all particles.

Finally, Specimen 3 in **Fig 7.11**, which was corroded continuously for 8 days, exhibits pitting from the cathodic particles as the dominating corrosion mechanism, as well as intergranular corrosion attack. All three particles have evolved into very large pits, with Particle 3 even showing grain degradation arising from the original pit where its corrosion morphology matches the length of the large center grain observed in the IPF orientation map. The pit from Particle 1 also has indications of coalescence with another pit on its left, which is shown by a black localized cavity elongating under the left edge of the pit. Particle 1 was located inside a large grain whereas

Particles 2 and 3 were located at a grain boundary. Only high-angle grain boundaries were observed at the studied particles. It should be noted that the corrosion damage arising from these particles span several grains and is shown to have a different type of morphology relative to the other two specimens.

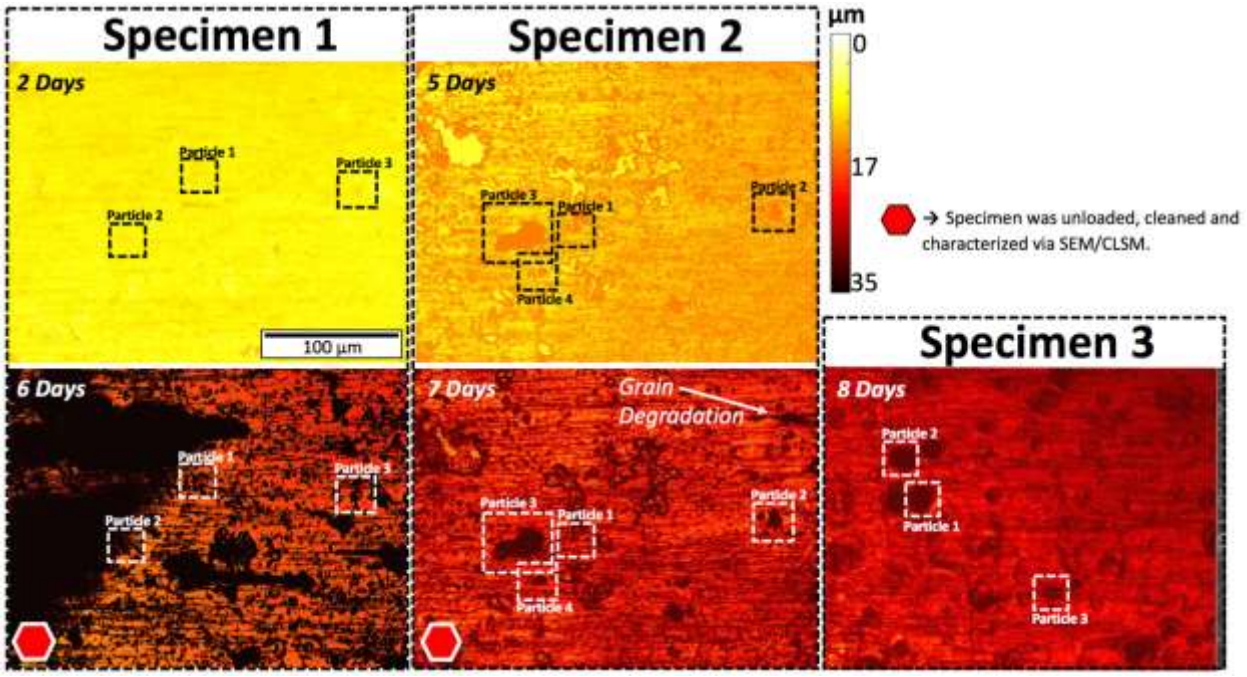

Fig 7.12 Corrosion surface morphology characterization using CLSM for each specimen's ROI after the specified corrosion length. The early destruction of the oxide layer enables more extensive grain degradation (Specimens 1 and 2).

When analyzing the entire ROI for each specimen, different types of corrosion morphologies are observed. **Fig 7.12** shows the corrosion morphologies characterized via CLSM after each corrosion period, with each corrosion schedule having been chosen to identify the differences in interrupted and uninterrupted corrosion. The largest contrast observed is that after 6 days of interrupted corrosion, Specimen 1, asides from showing moderate pitting from the cathodic particles, exhibits large sections of grain degradation, where fallout of grain fragments have led to large zones with a sizeable amount of material removed. In contrast, for 8 days of uninterrupted corrosion, Specimen 3 shows deep localized pitting from the cathodic particles, with no observable grain degradation at the ROI. Although both specimens show corrosion depths beyond 30 µm, the morphologies look markedly different. Similarly, for 7 days of interrupted corrosion, Specimen 2

shows mostly pitting-based corrosion, albeit there are some regions that start to exhibit grain degradation on the upper right of the ROI. This marked difference in corrosion morphology may have been affected by the removal of the protective passive layer and corrosion products for Specimen 1 and Specimen 2 due to the cleanup of the material in-between interrupted corrosion schedule, which is in contrast with the unaffected passive layer and corrosion products that Specimen 3 developed during its uninterrupted corrosion time.

7.3.2 Mechanical Results

To ensure that the stresses obtained via EVP-FFT modeling reasonably represent the mechanical behavior of the material under constant loading, the strains need to be calculated and validated with the actual experimental results. **Fig 7.13** shows such validation of the residual strain characterizations after each specimen was loaded up to 2.5% and unloaded, with the final results from the SEM-DIC characterization being observed on the left column and the analogous EVP-FFT model results being observed on the right column of **Fig 7.13**. The simulated strain distributions, not only show similar magnitudes when compared to the experimental strain maps, but also exhibit spatial matching of the regions of strain localization.

The EVP-FFT strain results for Specimen 1 shows the strain accumulation is concentrated on the lower right of the ROI, which is validated by the experimental SEM-DIC strain map, albeit at a slightly lower resolution due to the lower magnification used during SEM image acquisition for Specimen 1. The EVP-FFT strain results for Specimen 2 capture the diagonal strain localization across the ROI from the upper left to the lower right. Similarly, the EVP-FFT strain results for Specimen 3 capture the diagonal lower left to upper right strain, along with the large strain concentrations on the upper right corner of the ROI. In each of the specimens, the 45° banding is conducive to the macroscopic plane of maximum shear, based on uniaxial loading, while displaying localization around distinct microstructural features. With an acceptable accuracy, where both the distribution, the spatial trends, and the magnitudes are captured by the model, these strain field maps validate that the mechanical heterogeneity of the material is properly captured by the 3D EVP-FFT modeling based on the grain orientation maps used as input.

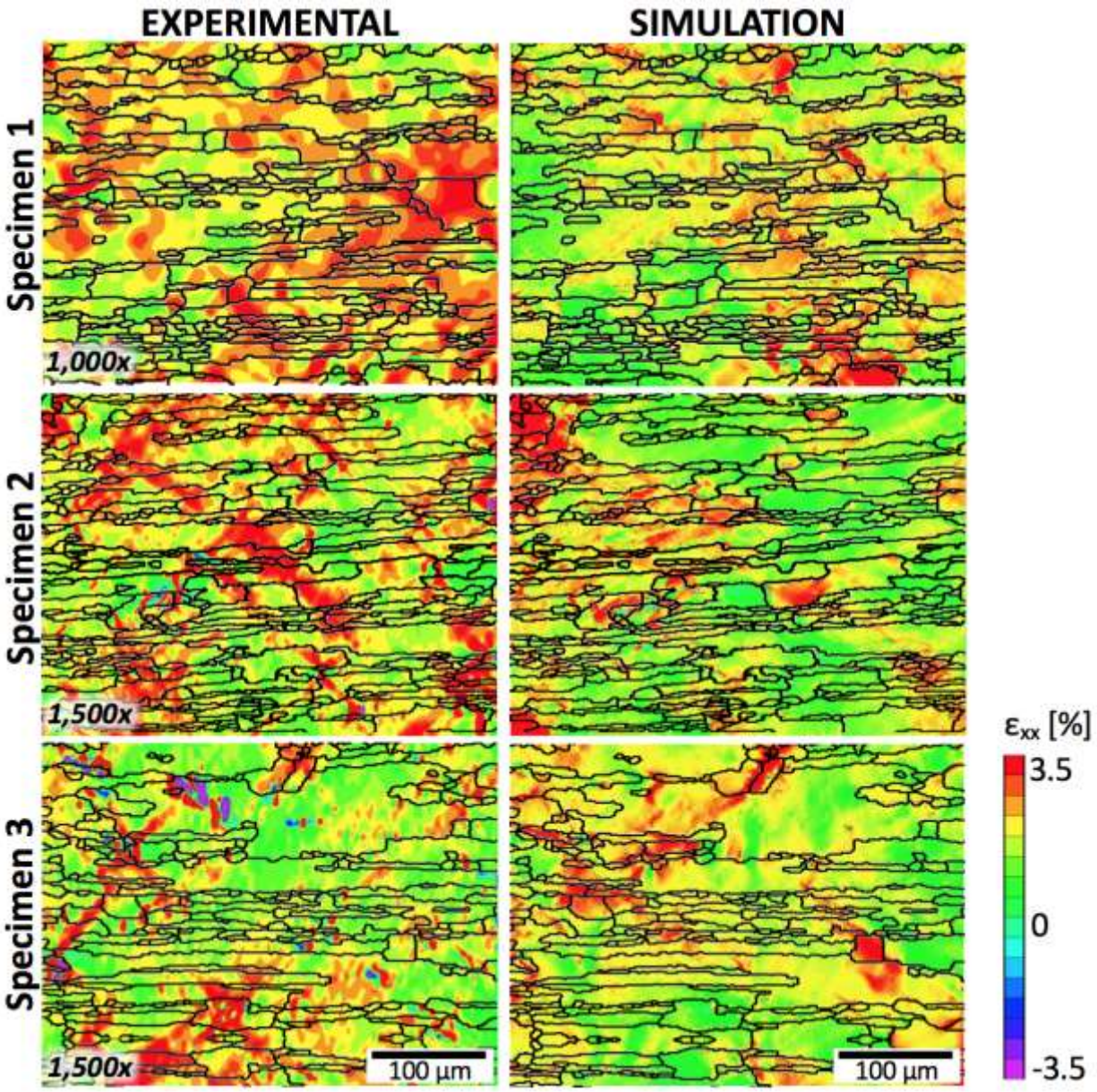

Fig 7.13 Comparison of the experimental and simulated residual strain distributions for each specimen after loading to 2.5% strain and subsequent unloading to ~1.8% strain. All models capture the strain patterning, thus validating their ability to capture localized mechanical behavior.

The stress results from modeling the material under constant loading, where each virtual microstructure is reloaded back to 2.5% strain, can be seen in **Figure 14**. At this state, Specimen 1, 2, and 3 have an average macroscopic axial stress of 451 MPa, 463 MPa, and 439 MPa, respectively, with localized axial stresses being as low as ~300 MPa or as high as ~600MPa. The

regions with highly concentrated stresses are zones in the material that may be more prone to failure and therefore considered as potential “hotspots”. All stress field maps show heterogeneity around the cathodic particles, which are modeled as an elastic, brittle medium. Heterogeneity can also be observed at the grain boundaries, to the point that the microstructure morphology can be discerned by the steep gradients throughout the stress field maps. Finally, larger grains without particles present exhibit intragranular stress heterogeneity, due to the surrounding microstructure specifically the anisotropic, adjacent grains.

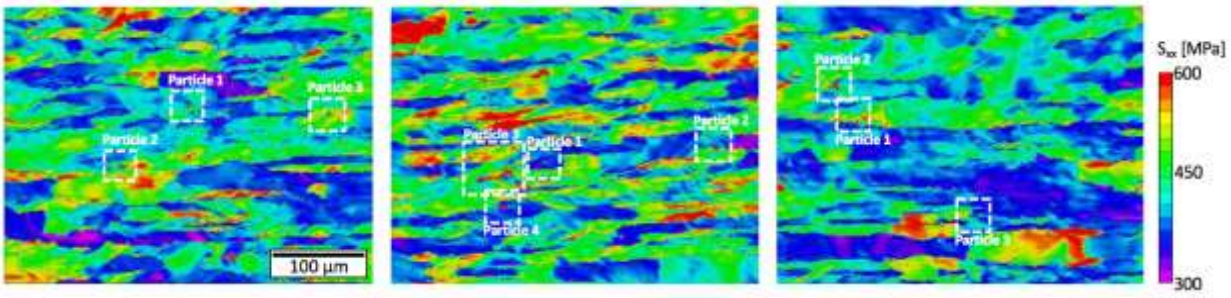

Fig 7.14 Simulated stress distributions for all specimens after loading to 2.5% strain, unloading to 1.8% strain, and reloaded again to 2.5% strain. The stresses tend to cluster within the grains. The particles are modeled under a purely elastic condition, thus redistributing loads on the surrounding matrix.

7.4 Discussion

Three different mechanisms were observed in the corrosion evolution of the specimens: intergranular corrosion, corrosion from cathodic particles, and grain degradation. Looking at the final depths of intergranular corrosion for all three specimens (**Fig 7.12**), it seems that the mechanism of intergranular corrosion behaves similarly for both interrupted and uninterrupted corrosion under constant stress. However, the other two mechanisms exhibit different severities depending on the corrosion duration and the interruption schedule of the experiment. The fact that the specimens with interrupted corrosion show a mixed corrosion morphology, whereas the uninterrupted specimen shows clear localized pitting, indicates that the interaction between these two mechanisms are affected by the presence, or absence thereof, of protective layers like corrosion product buildup or a thicker passive layer.

To better understand the interaction of these mechanisms, it is necessary to examine the evolution of corrosion with and without the removal of the passive layer. Specimen 1, after two days, shows that localized corrosion initiated at the cathodic particles and was on par with the depths of intergranular corrosion. Specimen 2, after 5 days, exhibits marked intergranular corrosion as well as localized pitting with varying depths, all of which originate from the cathodic particles. Specimen 3, after 8 days, shows a morphology entirely dominated by localized pitting from the particles, with the intergranular corrosion still being discernible. It is reasonable to surmise that pitting corrosion is the leading mechanism when the material develops a passive layer at the surface. This could be possibly explained by the fact that, whereas the passive layer (and possibly some slight corrosion product buildup) is protecting the majority of the matrix, at the particle interface exposed to saline solution, the passive layer is chemically broken by the particle itself and offers no protection from the localized reaction taking place, which is in agreement with studies of the change in corrosion morphologies due to passive layer breakdown at the particle [124][125] and accumulation of corrosion product [34]. This would result in the sharp pitting corrosion morphology observed after 8 uninterrupted days of corrosion.

When studying the morphologies captured after interruption of the corrosion experiments, an entirely different corrosion evolution occurs. For the examined ROIs for Specimen 1 and Specimen 2, not only is the intergranular corrosion more prominent after being subjected to corrosion for the second time, but also grain degradation is observed to take place. Interestingly, although Specimen 1 was exposed to a shorter corrosion period (6 days) than Specimen 2 (7 days), the degradation observed was more severe for Specimen 1. It is likely that, whereas Specimen 2 had 5 days to develop a more resistant and thicker layer of both passive alumina and corrosion product, Specimen 1 barely developed a layer on the first 2 days of uninterrupted corrosion. Therefore, the earlier destruction of the layer may have allowed for the full interaction between intergranular corrosion and cathodic corrosion to drive the material degradation and weaken it sufficiently for grain fragmentation and fallout to occur. This could be confirmed by the fact that Specimen 2, albeit shows initial stages of grain degradation on the upper right region of the ROI, has not yet experienced grain fallout at a larger scale. Therefore, a high likelihood exists that Specimen 2 would show more severe grain degradation similarly to Specimen 1, if it were left to corrode under constant loading for a longer period of time.

It is also of interest to analyze the mechanical behavior of the material at the cathodic Al_7Cu_2Fe particles. **Fig 7.3**, **Fig 7.4**, and **Fig 7.5**, show that Al_7Cu_2Fe cathodic particles exhibit a very stiff behavior, with no deformation occurring within the particle and with mechanical heterogeneities being observed in the surrounding matrix, due in part to the load partitioning between the particle and matrix. It can also be observed that the mechanical heterogeneity surrounding the particles complies with both the near 45° banding corresponding with the macroscopic shear plane and with the surrounding microstructure. Therefore, it was confirmed that the analogous EVP-FFT stress distributions accurately describe the mechanical behavior of the particles and thus properly capture the mechanical heterogeneities around the particles, as seen in **Fig 7.14**.

The actual values as well as their location relative to each other can be used to pinpoint any trends between the local mechanical state and the local corrosion in the material that may further provide understanding of the effect that both the stresses and strains have on corrosion. To locate the most representative variables of the mechanical condition of the material, a Principal Component Analysis (PCA) was performed using R [118] for the in-plane laboratory frame coordinate system (CSYS) stress components under constant loading S_{xx}, S_{yy}, and S_{xy}. Additionally, some laboratory CSYS stresses typically used in literature as failure indicators were used, namely the principal components S_I, S_{II}, the Von Mises component S_{vm}, and the in-plane max shear component S_{max} [96]. PCA revealed that the most representative variables that best capture the mechanical condition of the material are limited to two: the axial stress S_{xx} and the shear stress S_{xy}, which map onto the 1^{st} and 2^{nd} axis of the data cloud, respectively. The cumulative projected inertia was 70%, which means that the 1^{st} and 2^{nd} axes of the PCA jointly capture 70% of the variance in the data cloud. These two variables will be further used to find trends between the micromechanical behavior of the material and the localized corrosion.

To locate trends between the datasets, Gaussian Process (GP) modeling [119] was used to fit a surface response of corrosion given the localized stresses or strains, such that corrosion = $f(S_{xx}, S_{xy})$. Covariance function kernels were used to perform multivariate spatial correlations such that the correlation analysis not only compares values that are superimposed on an exact location, but

also compares values in the near vicinity of the queried location. This spatial cross-correlation is necessary to be included during GP fitting because both the corrosion morphology studied as well as the mechanical heterogeneity has been shown to be heavily localized in clusters.

To ensure a one-to-one comparison between datasets, all available data were resized to have the same resolution. Therefore, all other datasets were resized via bilinear interpolation such that each 300 x 400 μm map had a resolution of 0.1 μm, matching the resolution of CLSM. This resulted in each dataset containing ~12 million points, which in turn required specialized Gaussian Process methods capable to process large data under reasonable computational times. GP-SVI [120] was therefore used to fit a response surface of the datasets, an explanation of its fast computational abilities described in [123]. For the stress versus corrosion surface fittings, a Matérn 5/2 covariance function kernel was used, with a learning step rate of 0.15, a learning momentum of 0.59, 50 inducing inputs, and a mini-batch size of 20,000, and a local kernel noise variance of 1 Pa.

Fig 7.15 shows the fit surface response of corrosion = $f(S_{xx}, S_{xy})$ for the entire ROIs at different corrosion durations, where about 1500 datapoints beyond 3σ were filtered as outliers to improve the data ranges onto which GP-SVI will attempt to fit the surface response. The contour lines correspond to the fit surface and the multicolored scatter corresponds to the input data. GP-SVI provides evidence of a good correlation, which is indicated in this case when the fit surface highlights areas of high stress corresponding to locations with high response values. That is, if the surface fits high corrosion values to stresses above the mean macroscopic stress, then it is concluded that corrosion is a function of stress. Since **Fig 7.15** shows all fit surfaces converging towards the mean macroscopic stresses, it can be concluded that for the material in general (for the full ROI), there is no correlation between mechanical stress and corrosion depths at any point during the evolution of corrosion. However, this may not be the case for zones where the cathodic particles affect the material.

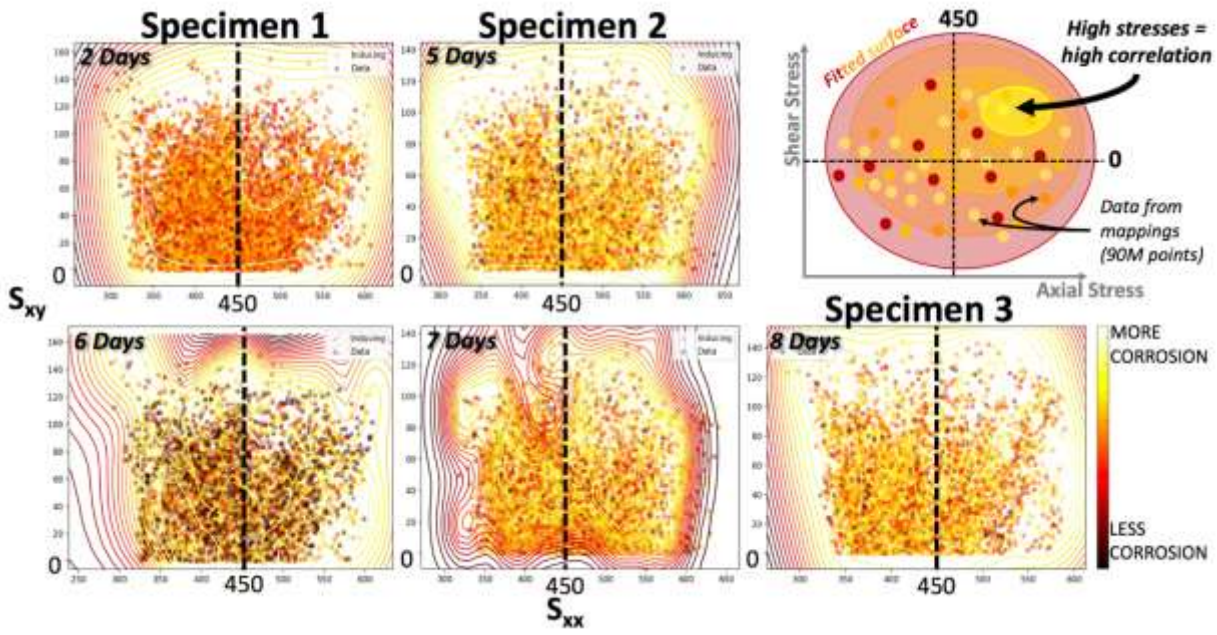

Fig 7.15 Gaussian Process (GP) fitting for the ROI. To find correlations between computed stress (axial and shear) and corrosion, a surface is fitted (contour plot) to locate trends. No correlation between high stresses and corrosion is observed.

To evaluate the joint chemical and mechanical effect that the cathodic particles have on the corrosion evolution of the material, GP-SVI fitting was performed in the vicinity near each of the particles studied. A visual description of the data thresholding procedure around the particles can be observed in **Fig 7.16**.

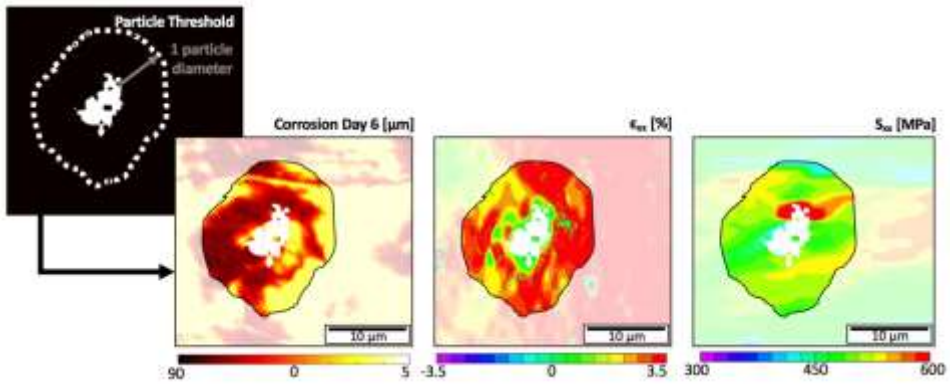

Fig 7.16 Thresholding metric at the particles, showing Particle 3 of Specimen 1 as an example. The maximum particle diameter is used (12.1 μm) to threshold the data surrounding the particles.

These thresholded datasets in the vicinity of the cathodic particles yield the fit response surfaces observed in **Fig 7.17**, which show fitting of high corrosion values onto high stresses well above the mean macroscopic stress for all stages of corrosion. Particle 2 of Specimen 1 shows that high levels of axial and shear stress correlate with the localized corrosion developed before particle fallout, regardless of passive layer removal. Particle 2 of Specimen 2, which experienced particularly deep localized corrosion from the joint effect of the particle and the low-angle grain boundary, shows that only high axial stresses correlate to corrosion with no significant change after the removal of the passive layer corresponding to the interrupted corrosion schedule. Particle 3 of Specimen 3, which shows the final stages of localized corrosion where grain fragmentation and fallout occurs even with an unaffected passive layer, sharply exhibits both high axial and shear stresses correlating with high corrosion values. Since all 10 particles exhibited such a trend with varying degrees of sharpness, as can be seen in **Fig 7.18**, it can be concluded that the localized corrosion at particles is affected by the local mechanical state of the material, which means that the electrochemical degradation of the matrix is further enhanced by high stresses in the material.

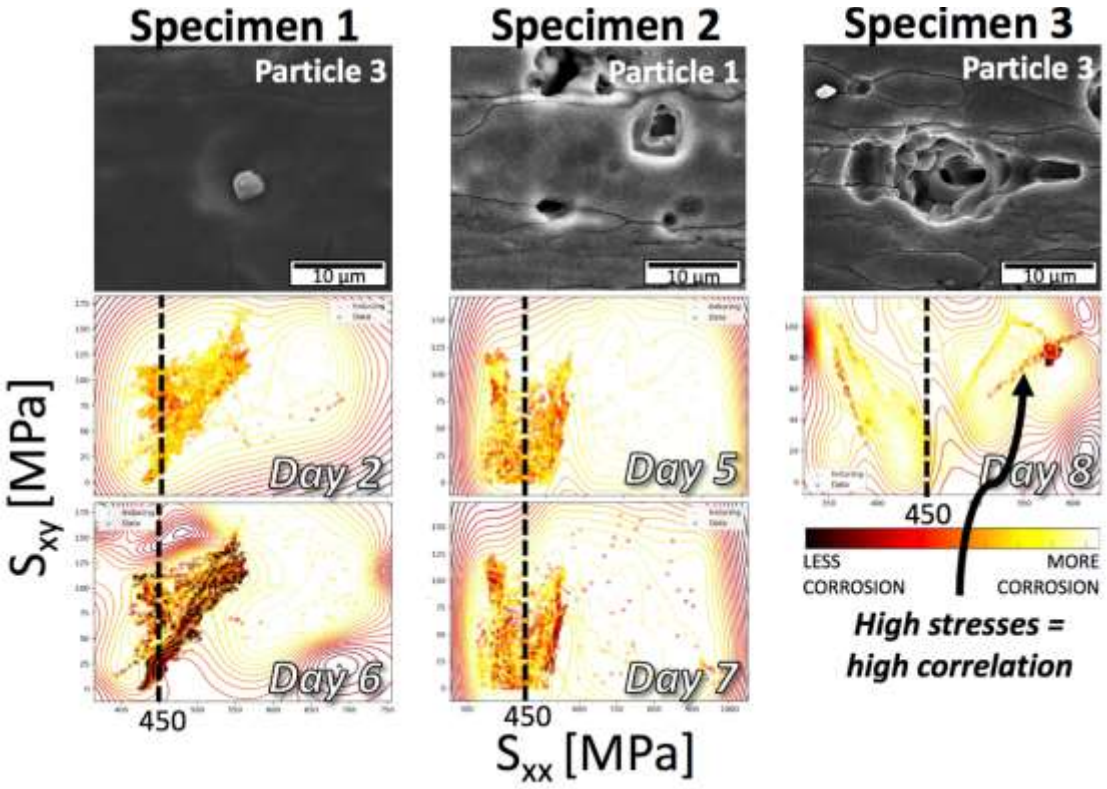

Fig 7.17 GP fitting was performed on the data surrounding the particles, and a clear trend between high axial stresses and corrosion was observed for each particle.

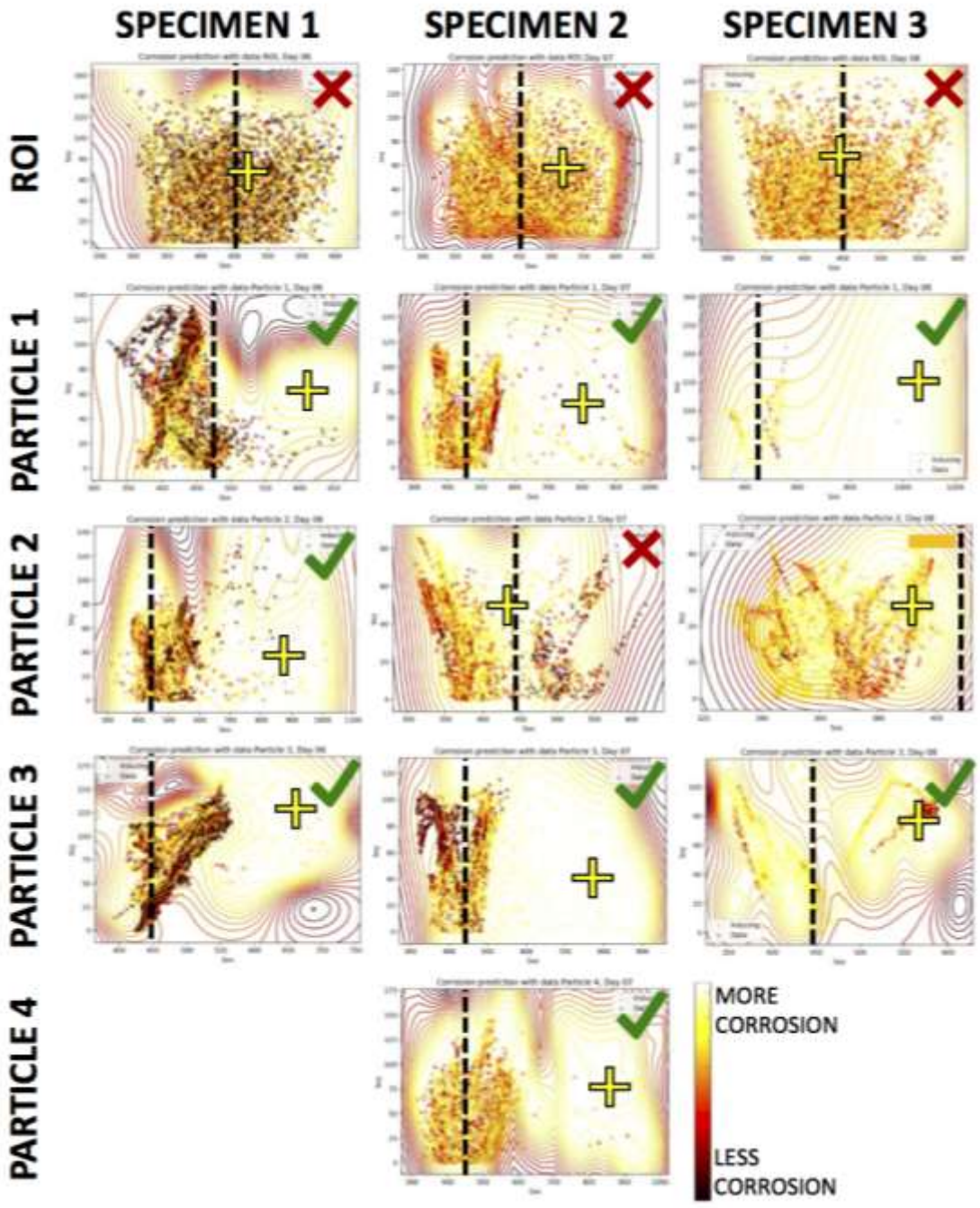

Fig 7.18 Gaussian Process (GP) fitting response showing corrosion trends relative to the axial stress S_{xx} and the shear stress S_{xy}. For all but two particles and none of the ROIs, the maximum values (depicted by a + symbol) converge around high stress values, thus showing a statistically significant correlation between high strains and deeper corrosion profiles on regions affected by the local electrochemistry.

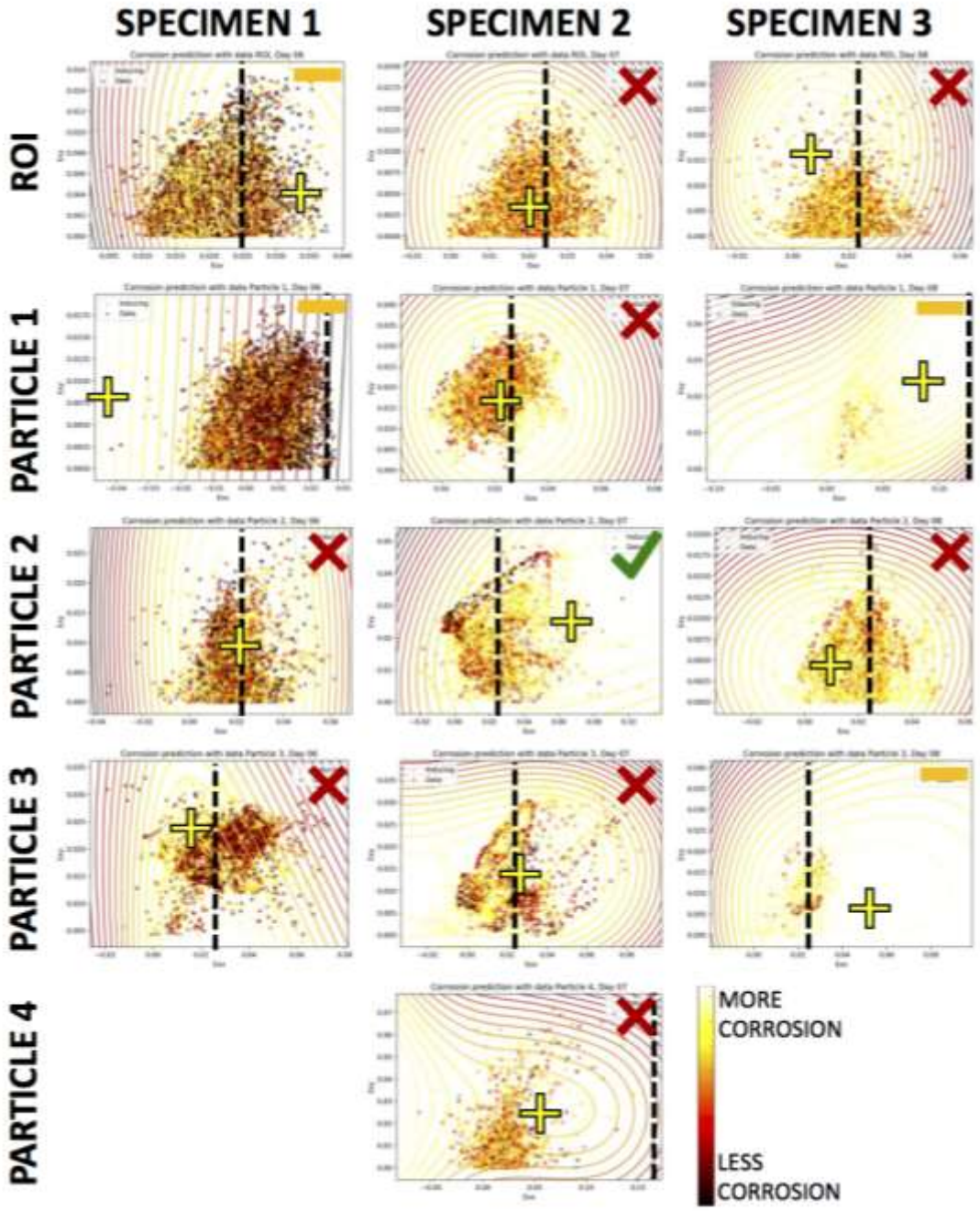

Fig 7.19 Gaussian Process (GP) fitting response showing corrosion trends relative to the axial strain ε_{xx} and the shear strain ε_{xy}. For all particles and all ROIs, the maximum values (depicted by a + symbol) converge around the average strain values, thus showing no statistically significant correlation between high strains and deeper corrosion profiles.

Finally, to investigate whether the residual strains are now able to predict localized corrosion under constant loading, especially when compared to the previous study where the residual strains did not correlate to the depth of corrosion for an unloaded material [123], GP-SVI modeling was performed on experimental residual strains captured in the laboratory CSYS via SEM-DIC such that corrosion = f(E_{xx}, E_{xy}). The same parameters used for the stress versus corrosion surface fittings described previously were used, with a new learning step rate of 0.015 and a new local kernel noise variance of 1e-6 to fit the smaller strain magnitudes. No correlations between strain values and corrosion depths were observed for the full ROI analyses, nor at the cathodic particles, as seen in **Fig 7.19**. It should be noted that no particles exhibited cracking in any of the three specimens. This therefore cements the idea that localized corrosion is not a residual strain-driven mechanism but rather an active stress-driven mechanism accelerating corrosion at the cathodic particles.

7.5 Conclusion

This work presents a thorough investigation of the joint effect that the mechanical and chemical behavior of the material had on the evolution of its corrosion morphology relative to the microstructural features prior to its transition into crack formation. Given previous studies, it was hypothesized that corrosion may be a stress-driven mechanism, i.e. local pitting is accelerated by heterogeneous stresses forming relative to microstructural features. Therefore, three TS AA7050-T7451 specimens had their microstructure, chemical composition, and residual strains spatially characterized and then subjected to corrosion under constant loading. After various periods of corrosion, the specimens were unloaded and their corrosion morphology was characterized both quantitatively and qualitatively for the entire ROIs and 10 individual particles. The corrosion arising from the cathodic particles, the grain boundaries, and the degradation of grains were captured. These corrosion morphology maps were then spatially cross-correlated with computed stresses, obtained from analogous 3D EVP-FFT models, via GP-SVI modeling. From these procedures, the following conclusions were obtained:

- Localized pitting corrosion was dictated by the presence of cathodic particles. Further, grain boundaries, especially at low-angle grain boundaries, adjacent to the particles are more prone to localized pitting corrosion. On the other hand, most pits generated from particles inside

grains (exposed on the free surface during surface characterization) do not experience significant growth after particle fallout.

- High levels of axial, tensile stresses near the cathodic particles accelerated localized corrosion. These heterogeneous stresses developed due to the anisotropic behavior of the grains within the polycrystalline aggregate.
- Concentrated stresses above the mean macroscopic stress magnitude are an indicator of localized corrosion at the cathodic particles but are not an indicator of corrosion of the overall material. On the other hand, localized strains are not an indicator of corrosion neither for the overall material nor for the cathodic particles. Strain is not a state variable to indicate the degree of plasticity, and thus cannot be used as a descriptor for the susceptibility of corrosion.
- For similar corrosion periods, uninterrupted corrosion exhibits significant pitting, whereas interrupted corrosion exhibits grain degradation. The removal of the passive layer and corrosion products during interrupted corrosion due to surface cleanup allowed for earlier interactions of the mechanical and electrochemical behavior of the material that jointly enhanced corrosion.

8. FATIGUE CRACK INITIATION FROM CORROSION

8.1 Introduction

Since the maintenance of aging aircraft subjected to environmental degradation is limited by the understanding of the mechanisms driving the pit-to-crack transition, the development of digital twins has great potential of reducing costs given its surgical approach towards the maintenance and repair needs of each component [126], where the environmental history, the loading history, and the microstructure can be used as input for the proper prediction of damage.

In this chapter, our main goal is to couple the experimental crack initiation and the microstructure features into the CP models of corroded materials. The joint effect that the corrosion topology, the constituent particles, and the microstructure has on the crack initiation of pre-corroded AA7050 is studied by instantiating a full 3D EVP-FFT model from experimental XCT and EBSD characterizations. The resulting micromechanical field is used to calculate FIPs, which are used to predict the crack initiation location in the material. This chapter has five main goals:

1. Develop a procedure for building an equivalent multivariable computer model that can account for the multiple variables driving cracking and can be used for digital twins.
2. Evaluate the different FIPs available in the literature and determine the metric that best represents the driving force for fatigue crack initiation from corrosion damage.
3. Evaluate the overall distribution of the FIPs in the reconstructed model as well as their ability to predict the location of crack initiation.
4. Determine the level of significance of the different factors contributing onto the predictive capabilities of FIP distributions (microstructure vs geometry vs particles).

This chapter gives a better insight of the driving mechanisms behind environmentally assisted crack initiation and improves the current approach on the fracture mechanics of corroded materials. The experimental characterization in this chapter as well the post-mortem location of crack initiation was performed by Dr. Noelle Co and Dr. James Burns at University of Virginia, while the data post processing, 3D microstructure instantiations of the material, EVP-FFT modeling, and data analyses were performed by the author. A complete description of the chapter can be found in: *A. Nicolas, N.E.C. Co, J.T. Burns, M.D. Sangid, Predicting Crack Initiation from Coupled Microstructure and Corrosion Morphology Effects, Submitted to Engineering Fracture Mechanics (2019).*

8.2 Materials and Methods

8.2.1 Material and corrosion protocols

The material and corrosion protocols were performed by our collaborators Prof. James T. Burns and Dr. Noelle E. Co at University of Virginia in Charlottesville, VA. Four AA7050 specimens were machined parallel to the rolling direction of the plate (LT) and centered at a through-thickness (t) location of t/8. The specimens had a 7.6 mm thickness, uniform gage length of 20.96 mm, and reduced gage width of 7.60 mm, and were polished down to a 600 grit finish. To investigate the effect of corrosion morphology on crack initiation, two different corrosion protocols were applied on the LS surface of the specimens. The first protocol aimed to achieve a discrete pitting (DP) morphology with isolated small pits, while the second protocol aimed to create a fissure (FIS) morphology with larger coalesced pits. For DP two specimens, named as D1 and D2, were held at -700 mVSCE using a potentiostat and exposed to 0.5M NaCl +$NaAlO_2$ solution for 1.5h where the pH was adjusted to 8 by adding NaAlO2. For FIS two specimens, named as F1 and F2, were exposed to 1M NaCl + 0.022M $AlCl_3$ + 0.05M $K_2S_2O_8$ solution for 168h (7 days) while inside a relative humidity chamber. A full description of the corrosion chamber setup and the chemistry behind the electrolytes can be found in [26] and [127]. Once the specimens were corroded, their surfaces were cleaned with HNO_3 and ultrasonic cleaning using deionized water, acetone, and methanol.

All specimens were subjected to fatigue cycling after being exposed to corrosion. The maximum stress applied was 200MPa with a frequency of 20 Hz and a fatigue loading ratio R of 0.5. All fatigue tests were performed in a high relative humidity RH of 90% up to failure. To characterize the location of crack initiation, fractography was performed on the post-mortem cracked surface of the lower section of each specimen using a FEI Quanta 650 Scanning Electron Microscope (SEM) with a working distance of 10-15 mm, accelerating voltage of 10 kV, spot size of 4, and a magnification of 100x-250x. Marker bands were also generated at the cracked surface by following the protocol developed in [17] and [128]. The first marker band, generated after ~5000 cycles, was located <10 μm away from the crack initiation point. This initial marker band, alongside with fractography, helped locate the crack initiation point in each specimen.

8.2.2 Experimental characterization

Similarly, the experimental characterization was performed by our collaborators Prof. James T. Burns and Dr. Noelle E. Co at University of Virginia in Charlottesville, VA. After fatigue testing, each section of the fractured specimens was subjected to XCT to characterize both the 3D corrosion geometry and the Al_7Cu_2Fe constituent particles. An Xradia MicroXCT-200 microscope was used with the following parameters: 80KV source voltage, 8 source power, 100μA current, 25-30 mm source-sample distance, and 17-25 mm detector-sample distance. Each section was rotated 180° around the L-direction. Based on the size of the region of interest (ROI) desired for each specimen, imaging was performed using a either 2x magnification with 2 μm pixel resolution or a 10x magnification with 0.7 μm pixel resolution. Additional details of the XCT scanning can be found in [129]. The final image stacks were post-processed to remove noise arising from center shift and beam hardening using the TXRM reconstruction program, sectioned to cover only a region of interest (ROI) around the known crack initiation points capable of covering the most significant corrosion features, and reconstructed into the final 3D geometry using the Avizo software [130]. The final solid 3D volumes had a resolution of 1.5μm for specimen D2, 1.6μm for specimens D1 and F2, and of 3μm for specimen F1.

To characterize the microstructure in each specimen, EBSD was performed on the cracked surface of the lower section by our collaborators at University of Virginia. To obtain the mirror-like finish necessary for EBSD, the surface was polished down to a 1200 grit, followed by a NAPPAD cloth with a sequence of diamond suspensions down to 0.25 μm. Afterwards the specimen was sonicated with acetone and methanol. An FEI Quanta 650 FE-SEM was used with the following acquisition settings: 20kV accelerating voltage, 10-15mm working distance, 250x magnification, spot size 4, step size 1μm, and 70° tilt. Only specimen F1 was scanned using a 100x magnification given its larger ROI. Any noise present in the EBSD scan was removed with standard filters available in the HKL Channel 5 Tango software. The final Inverse Pole Figure (IPF) map of the material in the TS direction is shown in **Fig 8.2b**. Given the elongated nature of the grains inside rolled materials, perfectly elongated grains were assumed for all specimen reconstructions.

8.2.3 Segmentation of microstructure and crack plane features

To properly characterize the Al_7Cu_2Fe constituent particles, the sectioned grayscale image stack was post-processed with an algorithm developed in-house at the ACME laboratory in Purdue University. This algorithm first blurs the 3D image stack sufficiently to remove all particles and leave just the grayscale background characterizing the matrix via pixel-wise adaptive low-pass Wiener filter [131]. Afterwards it subtracts the blurred 3D stack from the original 3D stack, thus leaving only pixels with intensity outliers. To ensure that only the brighter pixels are captured, only the pixels with intensity I higher than 1 standard deviation S ($I \geq \bar{I} + 1S_I$) are retained. Finally, slight erosion/dilation is performed on the 3D segmented particles to both remove single-pixel particles and improve the connectivity inside each particle. This algorithm also allows for verification of the matrix segmentation performed by Avizo by capturing the darker pixels characterizing the gas phase in the blurred 3D stack where $I \leq \bar{I} - 1S_I$.

Once both the AA7050 matrix and the Al_7Cu_2Fe particles were segmented, the lower and the upper sections of each specimen were aligned such that the overall distance between the cracked surfaces was minimized ($\sum\left(z_i^{upper} - z_i^{lower}\right) \rightarrow 0, \forall\, z_i^{upper} > z_i^{lower}$) where z is the height of each point i within the crack surface studied. Since the cracked surfaces experienced plasticity, elastic recovery, and other degradation during the cracking and final failure process [132], the cracked surfaces did not have a perfect fit with each other. Therefore, even after performing distance minimization between the cracked surfaces, gaps were present between the reconstructed sections, which needed to be filled appropriately with a solid phase, as seen in **Fig 8.1a**.

To ensure that the corrosion front was preserved and not inadequately filled by a solid phase, only the points in the upper surface that had a close neighbor with a point in the lower surface were allowed to be connected by a matrix phase: $dz_i = z_i^{upper} - z_i^{lower} \leq \overline{dz} + 3S_{dz}$. In this equation $\overline{dz}$ is the average of the height differences dz_i, and S_{dz} is the respective standard deviation. This allowed the sections to be properly connected by a solid phase while preserving the corrosion topography, as seen in **Fig 8.1b**. The geometry of the corrosion topography was further verified with optical microscopy images and white light interferometry images of the corroded surface prior to fatigue loading [132]. Afterwards, an equivalent crack plane was calculated by averaging the lower and upper cracked surfaces, such that the points in the crack

plane were always in the middle of the cracked surfaces, such that $z_i^{CrackPlane} = (z_i^{upper} + z_i^{lower})/2$. Finally, to ensure a proper representation of the material, the filled mid-section was further populated with statistically reconstructed particles, as seen in **Fig 8.1c**, where the statistics of both particle sizes and volume were directly obtained from the experimentally obtained XCT particles in the lower and upper sections of the specimen.

The particle volume fraction observed in both the lower and upper sections was enforced in the statistically reconstructed particles. To ensure that the crack plane properly represented the corrosion geometry, the corrosion front profile observed via fractography was enforced on the crack plane, as seen in **Fig 8.2a**. This ensured the minimization of geometric uncertainty in the material reconstruction in this critical plane of interest.

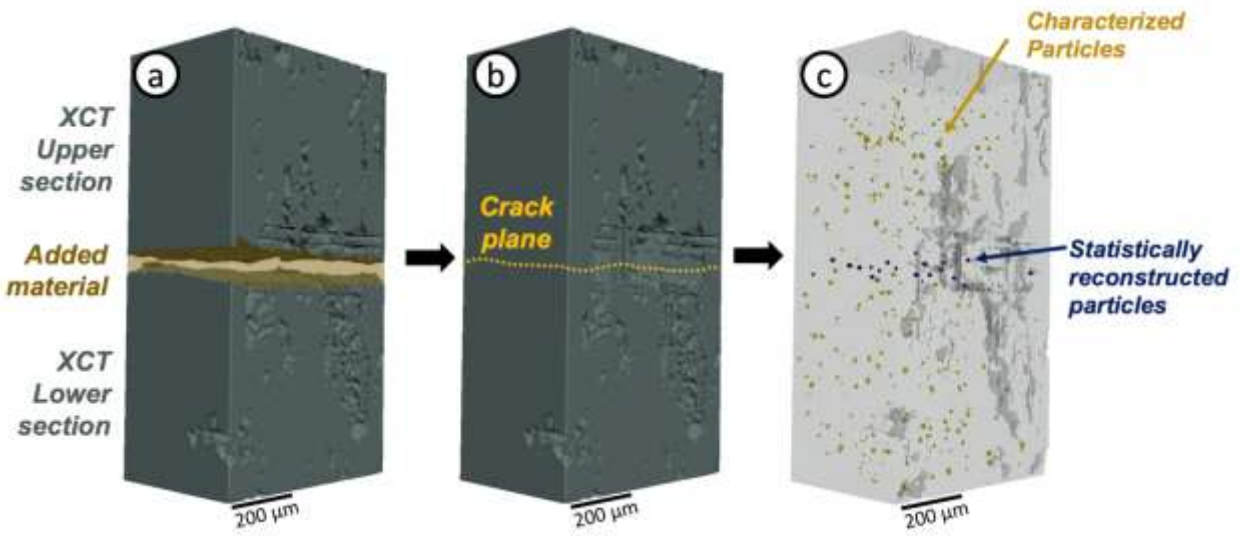

Fig 8.1 Geometry reconstruction from the post0mortem XCT specimen scans. (a) The specimen halves were aligned to minimize their vertical separation and according to the corrosion front, after which (b) the middle section was filled and the crack plane was calculated. (c) The middle section was further populated with cathodic particles statistically reconstructed from the experimental characterization.

The microstructural data inside each 3D reconstruction consisted of grain orientations extruded in the L direction, as seen in **Fig 8.2c**. The final IPF maps for all specimens can be observed in **Fig 8.3**, for which the average grain sizes were as follows: 35.73 µm for D1, 36.61 µm for D2, 52.04 µm for F1, and 55.4 µm for F2. All specimens exhibited an aspect ratio of 2 – 2.5 in

the TS plane. It should be noted that the EBSD scans plotted in this figure are just the subsection covering the ROI reconstructed from XCT.

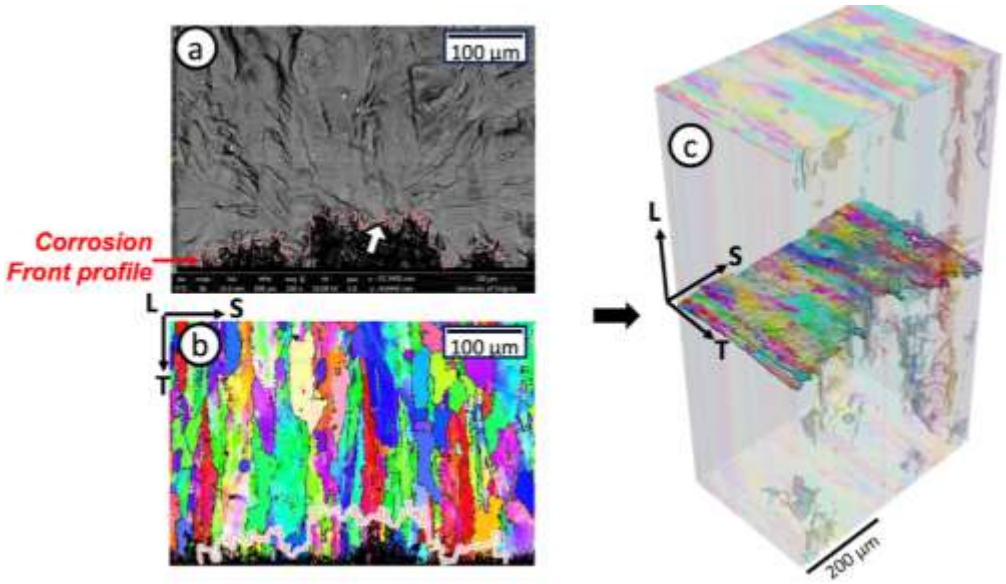

Fig 8.2 Post-mortem characterizations of (a) the corrosion front profile, and (b) the grain orientations at the crack plane. Both (a) and (b) are needed to create (c) the final 3D reconstruction containing both the corrosion topography and the local grain structure. The experimentally observed crack initiation point is signaled by a white arrow.

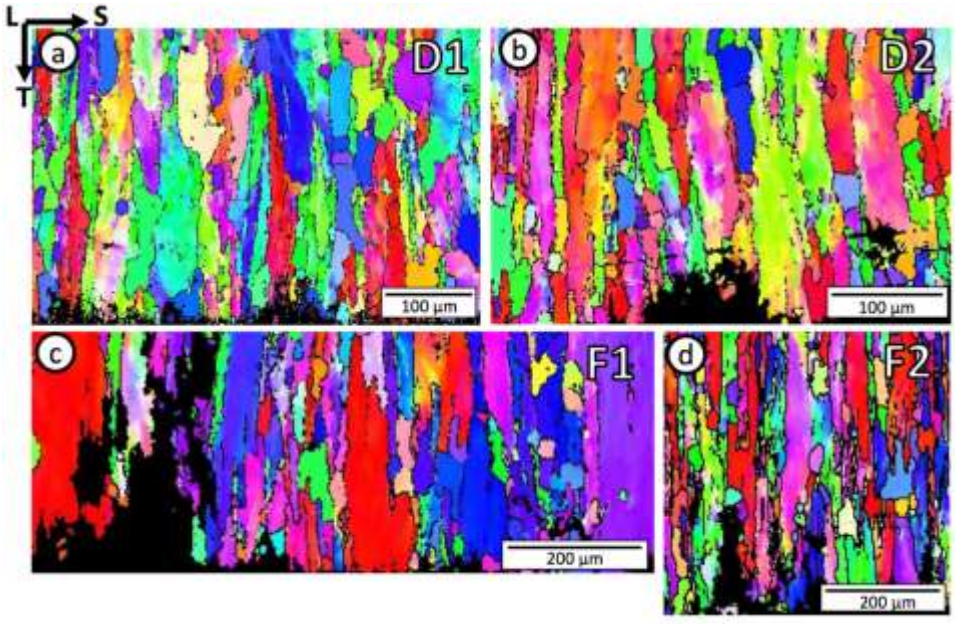

Fig 8.3 EBSD orientation scans for discrete pitting specimens (a) D1, (b) D2, and for fissure corrosion specimens (c) F1 and (d) F2.

8.2.4 Models and simulation

The 3D reconstructions from XCT and EBSD were input into one single data structure that contained both the corrosion geometry and the microstructure, as seen in **Fig 8.4**, with the resolution of all structures being limited by the XCT reconstructions. Each reconstruction was used as input for EVP-FFT, where each simulation was loaded up to 3% strain (530 MPa), past the yielding point in the material, to ensure the activation of plasticity in the microstructure. Only macroscopic strain along the L-direction was enforced.

To ensure periodicity the material was padded on the L direction until a size of 2^q was reached, where q is a positive integer. To prevent both any artificial stress concentrations from the periodic boundary condition, as well as preventing corrosion features from acting as artificial corner notches, each reconstruction was padded with a solid phase on all sides, except for the corroded surface, which was padded with a dummy gas phase. A sensitivity analysis indicated that a minimum padding of 32 voxels was necessary. The final sizes of each EVP-FFT model were as follows: 340 x 240 x 640 voxels for specimen D1 (1 voxel = 1.6 μm), 368 x 256 x 640 voxels for specimen D2 (1 voxel = 1.5 μm), 392 x 176 x 256 voxels for specimen F1 (1 voxel = 3 μm), and 368 x 368 x 640 voxels for specimen F2 (1 voxel = 1.6 μm). All models were run via parallelization to achieve convergence under reasonable computational times [91]. Each specimen required 7-10 h of runtime using 6 HP nodes with two 10-core Intel Xeon-E5 processors and 64 GB of memory.

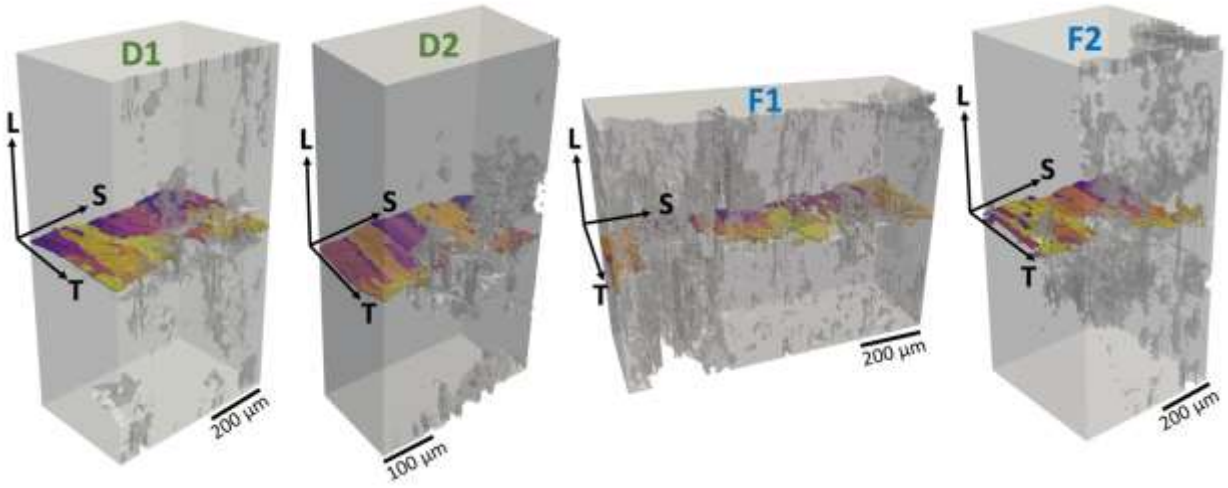

Fig 8.4 Full 3D reconstructions and mean crack planes for discrete pitting (D1, D2) and fissure corrosion (F1, F2) specimens. Unique grain IDs colors are plotted on each crack plane.

8.2.5 Crack Nucleation from Corrosion

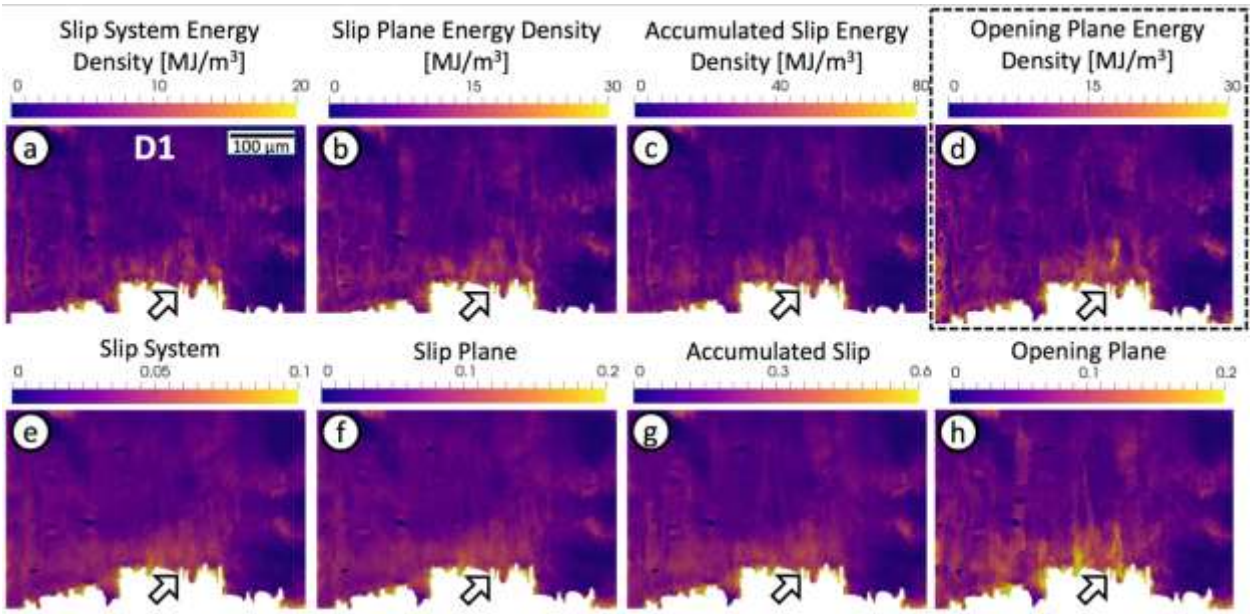

Fig 8.5 Comparison of the eight different Fatigue Indicator Parameters (FIP) in the crack plane of discrete pitting specimen D1. The (d) opening plane energy density FIP is used in further evaluations as a predictor of crack initiation. The experimentally observed crack initiation point is signaled by a white arrow.

The FIPs described in the Methodology section were analyzed. As seen in **Fig 8.5**, there are no significant differences between all eight FIPs. Therefore, a single FIP was sufficient to analyze the crack nucleation event on pre-corroded materials. Now, given that energy dissipation metrics are more sensitive to the crystallographic behavior in the material [133] and that the OPED parameter has been shown to contain the highest amount of mutual information between all FIPs **Error! Reference source not found.**, all subsequent crack initiation studies were performed using the energy-based OPED parameter.

To properly capture the length-scale of the micromechanical fields driving crack initiation and to remove any artificially high values from the calculated FIPs due to the Gibb's effect, several non-local regularization schemes were performed in the FIP voxel values. As seen in **Fig 8.6**, three non-local averaging schemes were used: averaging around each point (**Fig 8.6a**), averaging per slip band (**Fig 8.6b**) and averaging per grain (**Fig 8.6c**). The latter two, averaging per slip band and averaging per grain, have been used previously in literature [134] to perform microstructurally

sensitive averaging on equiaxed grains. The more refined metric, averaging around each point, is known to adequately smooth out extreme values while at the same time preserving slip-based heterogeneity [72].

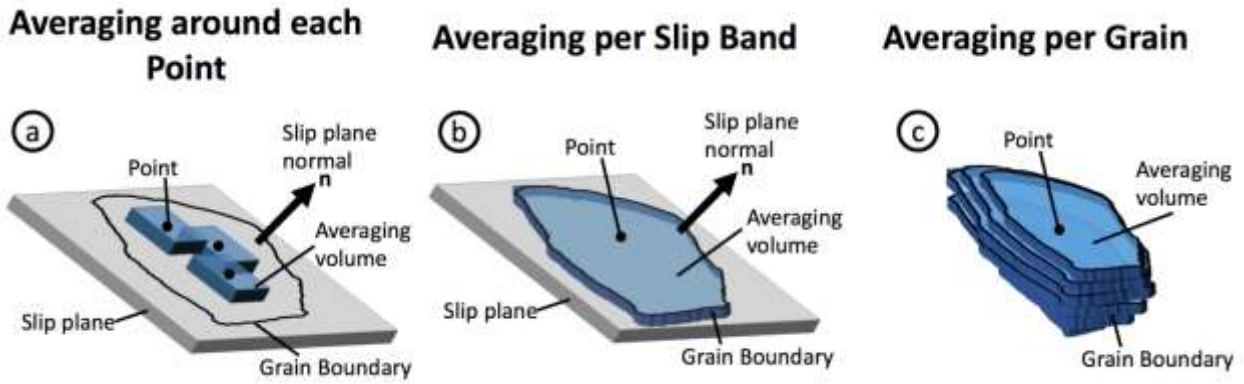

Fig 8.6 Schematic of different averaging metrics: (a) averaging around each point with subsections being set irrespective of the average grain size (b) averaging per slip bands with the slip band length being the average grain diameter, and (c) averaging by grain. All averaging methods are done per voxel, where the value of the selected voxel is the average between itself and the neighbors per grain/band/point region.

When analyzing the averaged FIP distributions at the corrosion front, the averaging around each point metric was the most suitable for preserving the hotspots that may indicate crack nucleation zones since it preserves the length-scale of the micromechanical fields within the grains, as seen in **Fig 8.7**. Sensitivity analyses performed on each specimen allowed to obtain the optimal averaging volume necessary when averaging around each point: 16 x 16 x 2 voxels for D1, 8 x 8 x 2 voxels for D2, 20 x 20 x 2 voxels for F1, and 8 x 8 x 2 voxels for F2.

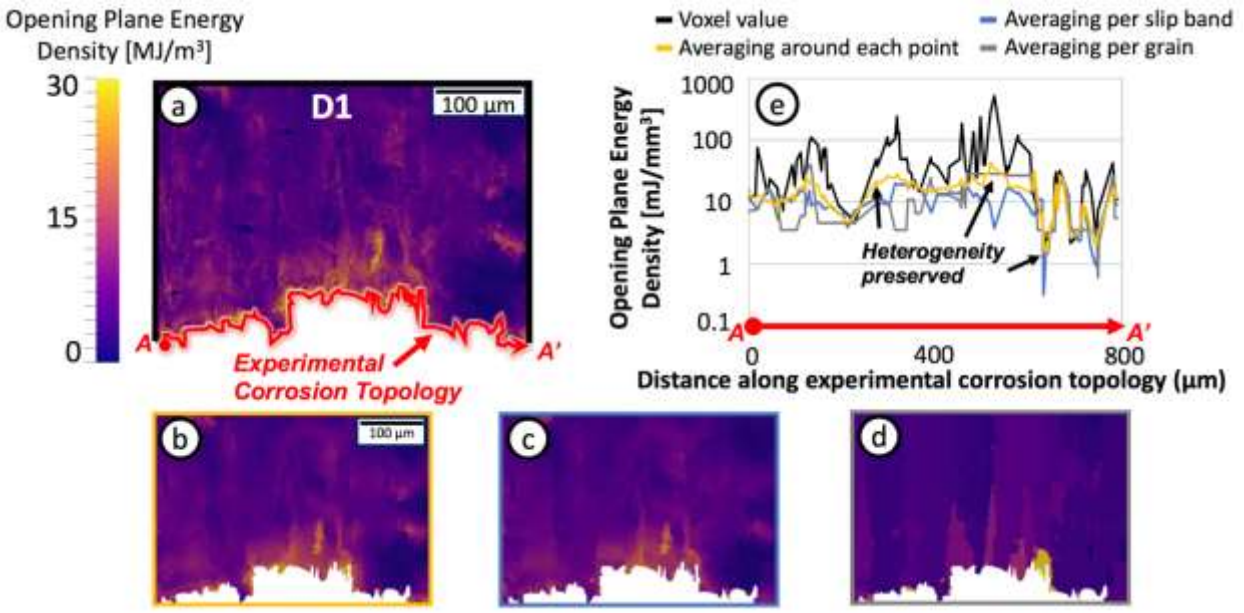

Fig 8.7 Comparison of the Opening Plane Energy Density distributions, before and after averaging, in the crack plane of discrete pitting specimen D1. The distributions of (a) the voxel value are averaged (b) around each point, (c) per slip band, and (d) per grain. (e) shows a quantitative comparison of the distributions (a, c, d, e) along the experimental corrosion topology A-A'.

8.3 Results and Discussion

The highest values of the non-local averaged FIP were used to evaluate the locations with the highest likelihood to nucleate a crack, in both the 3D corrosion geometry and the 2D crack plane. **Fig 8.8** shows that, for the 3D corrosion geometry analysis, the location of crack initiation predicted by the highest FIP value does not coincide with the location experimentally observed during post-mortem fractography studies. In fact, for each specimen reconstruction, the maximum FIP value places the crack initiation point at regions away from the middle section of the material. However, when analyzing other regions with relatively high FIPs, it was found that all crack initiation points are located within the five highest FIP values in each reconstruction. For the crack initiation points in the discrete pitting specimens, D1 was predicted by the third highest value (129 MJ/m^3) and D2 was predicted by the fifth highest value (55 MJ/m^3). For the crack initiation points in the fissure corrosion specimens, F1 was predicted by the fourth highest value (89 MJ/m^3) and F2 was predicted by the third highest value (153 MJ/m^3). All of these values, while not being the absolute hotspot, are statistical extremes lying outside 3 standard deviations of the FIP distributions, where the average FIP value across all specimens was found to be $\overline{OPED}$ = 22 MJ/m^3,

the standard deviation was S_{OPED} = 10 MJ/m^3, and consequently the $\pm 3S_{OPED}$ bounding values were between 0 and 52 MJ/m^3 across all specimens. For D1, F1, and F2, the calculated FIP value (OPED) corresponding to the location of experimentally observed crack initiation were +6 standard deviations beyond the average value ($6S_{OPED}$ = 82 MJ/m^3). It can be surmised that the FIPs statistically capture the regions with a higher probability of failure.

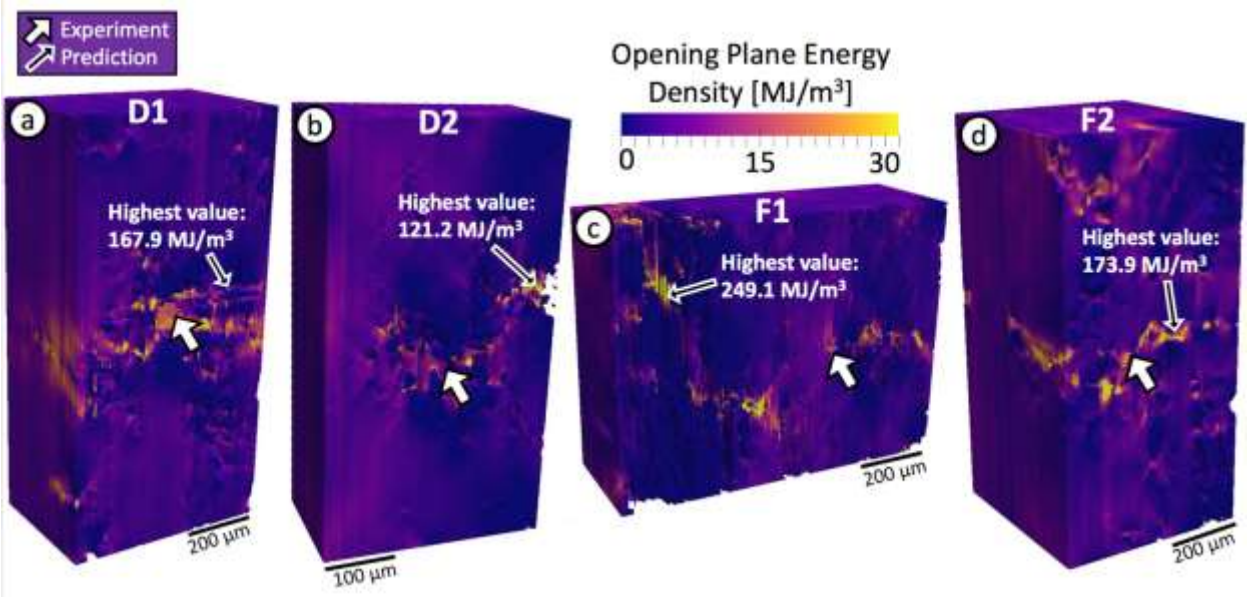

Fig 8.8 Crack initiation predictions in the entire morphology given the highest value of the opening plane energy density (averaged around points), for discrete pitting specimens (a) D1 (b) D2 , and for fissure corrosion specimens (c) F1 and (d) F2. The experimentally observed crack initiation point is signaled by a white arrow.

On the other hand, when analyzing the averaged FIPs at the 2D projection of the crack plane, **Fig 8.9** shows that the highest FIP values accurately predict the location of the experimentally observed crack initiation points for the fissured specimens F1 and F2, but not for the discrete pitting specimens D1 and D2.

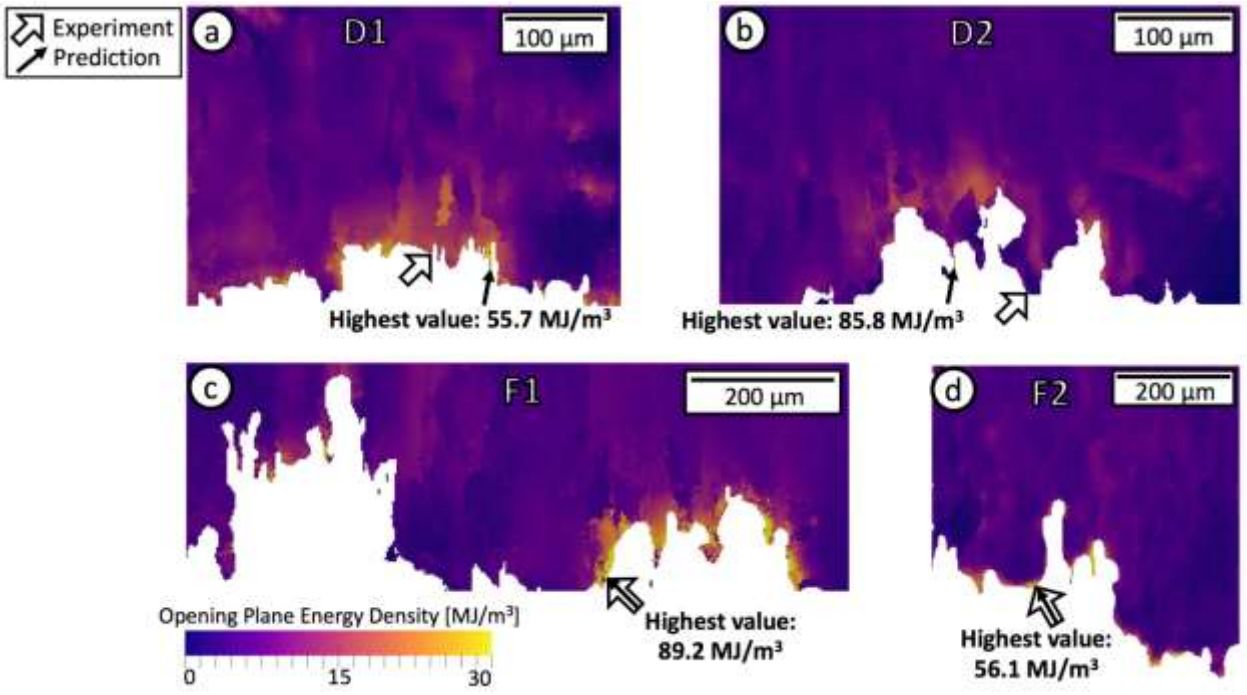

Fig 8.9 Crack initiation predictions in the crack planes given the highest value of the opening plane energy density (averaged around points), for the discrete pitting specimens (a) D1 (b) D2, and the fissure corrosion specimens (c) F1 and (d) F2. The experimentally observed crack initiation point is signaled by a white arrow.

The discrepancy in crack initiation predictions between the full 3D geometry analysis and the 2D crack plane analysis is mainly due to the increased level of microstructural uncertainty at the spatial points away from the crack plane. This increased uncertainty is due to the fact that the assumption of perfectly elongated grains is only suitable for spatial points close to the characterized crack plane [110]. In other words, the actual grain orientations away from the middle section have a larger degree of uncertainty, which in turn means that the calculated micromechanical response in the farther points have a higher degree of error than the points located at the crack plane. Conversely, the spatial points at the crack plane have the lowest level of microstructural uncertainty, thus becoming the region with the best capability of predicting crack initiation from calculated FIP values.

When analyzing the crack prediction results at the crack plane, it is noted that the FIPs are capable of predicting crack initiation at the heavily corroded FIS specimens, but not at the slightly corroded DP specimens. This may be due to the micromechanical effect that the Al_7Cu_2Fe

constituent particles may have on the less corroded DP specimens, for which pit coalescence and particle fallout has not significantly occurred, especially when compared to the fissured specimens, meaning that there may still be some particles present ahead of the corrosion front [17]. Therefore, to study the role of the constituent particles in the prediction of crack initiation, several large-sized particles were placed ahead of corrosion front on both a FIS specimen and a DP specimen. As seen in **Fig 8.10**, several particles with an average diameter size of 10 μm were placed ahead of the corrosion front of specimens D1 and F2. The crack prediction results from the modeling of particles ahead of the corrosion front were then compared with the results from the modeling of randomly instantiated particles.

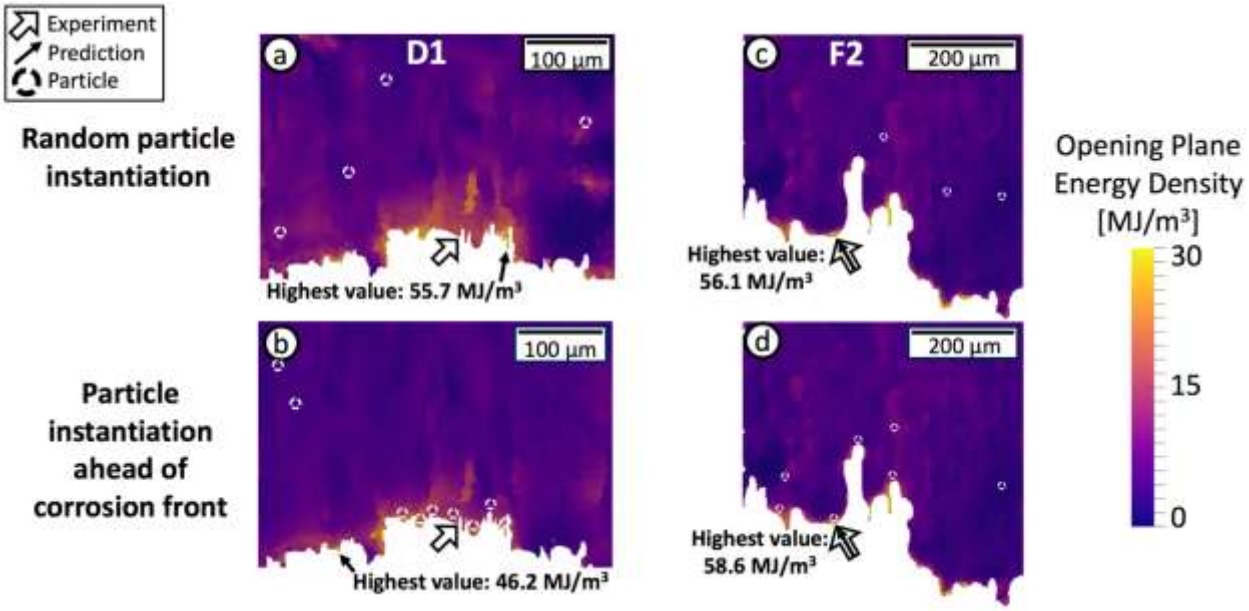

Fig 8.10 Crack initiation predictions given two types of particles locations: (a, c) random, and (b, d) ahead of the corrosion front, for (a, b) discrete pitting specimen D1 and (c, d) fissure corrosion specimen F2. The opening plane energy density distributions were averaged around each point. The experimentally observed crack initiation point is signaled by a white arrow.

It was observed in **Fig 8.10** that, while the presence of the particles has a slight effect on the local micromechanics of the material (slightly increasing the values, as seen in **Fig 8.10c** and **Fig 8.10d**, or changing altogether the predicted location of crack initiation, as seen in **Fig 8.10a** and **Fig 8.10b**), the placement of particles at the corrosion front does not improve the ability of FIPs to predict crack initiation.

This may be due to the smaller mechanical impact that the 10 μm Al_7Cu_2Fe particles may have relative to larger features such as the grains (30 – 120 μm) and the corroded geometry (30 – 150 μm), therefore making the particles a secondary mechanism behind the mechanical and geometric heterogeneity in the material. It should be noted that other studies have shown a much larger influence of the particles on the mechanical effect in corroded materials, for which the sizes are comparable to other micromechanical features in the material [135]. Additionally, the non-local regularization schemes further reduce the mechanical heterogeneity produced around the particles, especially since the radius of influence around the particles (10 μm = 6 voxels) has a similar or smaller size than the averaging volumes used. Furthermore, the resolution of the tomography reconstructions may have an effect on the modeling ability to predict crack initiation. Whereas for the fissured specimens the resolution is large enough the capture the tortuosity in the larger geometric features, this may not be the case for the lesser corroded discrete pitting specimens, for which the resolution may need to be higher for it to properly capture the smaller geometric features present in the corroded surface.

Finally, it should be noted that asides from the uncertainty that arises from the columnar microstructure assumption, there are additional sources of uncertainty that may affect the final modeling results in the material. One of the principal uncertainty sources is the relatively simple hardening law, e.g. the Voce hardening law, used in the CP modeling of the material, which isotropically hardens each slip system equally at a material point. However, the fact that there are only four parameters in this relatively simple hardening law lowers the uncertainty that may arise from the fitting of these parameters [136]. Another source of uncertainty is the uniform boundary condition applied to all EVP-FFT models. While the specimens themselves were exposed to a uniform load at the grips, the actual boundary conditions in the reconstruction are heterogeneous and are dictated by the unknown neighboring grains. Any improvement of the crystal plasticity models would require prior knowledge of the stresses that the neighboring grains apply on the studied grains [137]. However, while the addition of more realistic boundary conditions can improve the overall representation and accuracy of the crystal plasticity model, its effect is more pronounced on the individual voxel values near the applied boundary conditions [91]. The effect of the boundary conditions is minimized when the region of interest is located three grains away from the applied boundary conditions, meaning that if the material is sufficiently padded the results

will remain unaffected [91]. All in all, even though the uncertainty has been minimized for most of the variables affecting the modeling results in the reconstructed specimens, there will always be an innate amount of uncertainty that may have propagated through the various steps leading to the final micromechanical fields [136]. This therefore has an impact on the determination of a single critical FIP value that can be used as a threshold for determining the onset of crack initiation, as it relies heavily on the uncertainty present in the model. As such, the determination of a critical FIP value is unique for each reconstruction.

8.4 Conclusions

XCT and EBSD characterizations have been used as input for EVP-FFT simulations, in order to obtain the micromechanical fields at the corrosion topography and calculate the FIPs to predict crack initiation in the corroded material. It has been concluded that:

- It is possible to generate highly detailed crystal plasticity models of corroded materials that can take into account the multiple mechanisms driving crack initiation. These simulations provide a definitive step towards prognosis of the remaining life of corroded materials subjected mechanical loading.
- There is no marked difference between the various FIP metrics analyzed. Each of these FIP metrics benefited from the use of a non-local averaging schemes, to regularize spuriously high calculations at individual material points and provide a means of a characteristic length-scale for crack initiation
- Crack initiation is properly captured by extreme FIP values within the full 3D distribution of the material. In fact, all experimentally observed sites for crack initiation were at locations where the FIP values were, in general, at least six standard deviations greater than the average value. When analyzing the crack plane, which has the lowest microstructural uncertainty, the highest FIP value in the distribution is able to predict crack initiation for the fissured specimens.
- The prediction of crack initiation by FIPs coincides with the experimentally observed crack initiation points in the material, with the best results arising from the fissure corrosion specimens since the model instantiations were able to fully capture their pronounced corrosion tortuosity. the current results suggest that the FIP values are a reasonable metric for prognosis activities for the site of crack initiation.

- The microstructure and the corrosion topography play a vital role in the crack initiation of the material. The constituent particles play a lesser role.

9. CONCLUSIONS AND FUTURE WORK

9.1 Conclusion

The objective of this thesis was to identify the driving forces behind the galvanic corrosion process as well as its transition to cracking, by studying from both an experimental and computational perspective different mesoscale variables such as the microstructure, the local micromechanics, the presence of cathodic particles, as well as the corrosion morphology. To do so, several high-resolution experimental techniques such as DIC, EBSD, CLSM, EDS, and XCT were performed for the same regions of interest, which was large enough to cover a representative amount of the microstructure. To obtain the full description of the micromechanical fields, a parallel version of the EVP-FFT solver was implemented alongside with a subsurface minimization technique. This thesis was divided into four parts:

1. Investigated polycrystalline deformation for different orientations of AA7050.
2. Developed a subsurface reconstruction methodology capable of minimizing the subsurface uncertainty in crystal plasticity models of surface characterizations.
3. Analyzed the effect of different experimental and computed variables on corrosion growth such as strains, stresses, particles, and microstructure.
4. Studied the mechanisms behind crack initiation via modeling of pre-corroded materials, where FIP crack nucleation metrics were used to predict cracking.

The results from part 1 (**Chapter 4**) demonstrated that EVP-FFT was capable of statistically capturing the micromechanical heterogeneity experimentally observed in the material, with the spatial distribution being best captured by the TS orientation due to its low subsurface uncertainty. As a result, the TS orientation was studied on the subsequent parts, and the importance for a subsurface minimization methodology was highlighted. As a result, a subsurface reconstruction methodology was developed in part 2 (**Chapter 5**), where the statistics from surface characterizations are directly used to create a subsurface microstructure that complies with both the orientation distributions and the microstructural geometry present in anisotropic materials such

as rolled AA7050. This reconstruction methodology showed a marked improvement in capturing the spatial distributions of the micromechanical fields.

Given the new capability of spatially capturing stresses and strains, part 3 could be performed. In part 3, the driving forces behind corrosion were studied under both a strain mediated environment (**Chapter 6**) and a stress mediated environment (**Chapter 7**), where the stresses in **Chapter 7** were obtained via EVP-FFT modeling. In both cases, GP-SVI was utilized to locate the main variables driving corrosion. For strain mediated corrosion, the material has high residual strains and low residual stresses, whereas for stress mediated corrosion, the material has both high active strains and high active stresses, as seen in **Fig 9.1**.

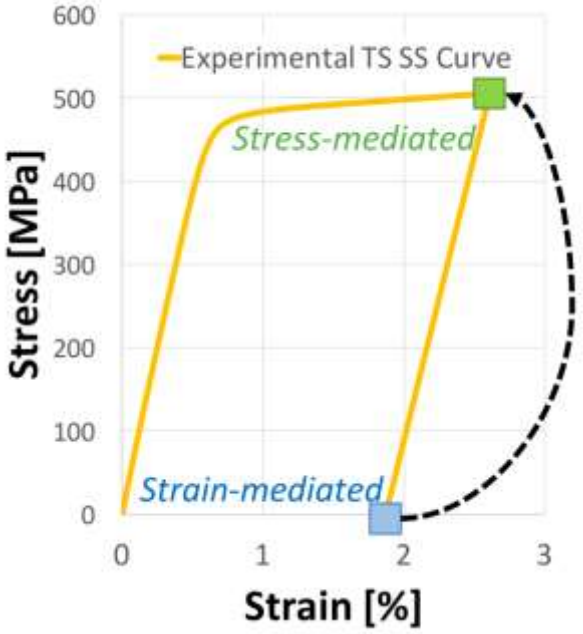

Fig 9.1 Loading description of strain-mediated corrosion, where only residual strains are present, and stress-mediated corrosion, where both strains and stresses are active in the material.

The results from strain mediated corrosion in **Chapter 6** showed that the early stages of corrosion growth are driven by the local electrochemistry between the particles and the matrix, and after particle fallout corrosion is driven by both the dissolution of the surface and the presence of extreme residual strains arising from particle cracking. When studying the overall material, the statistical analyses via GP-SVI showed that in general corrosion is independent from localized strains. The results from stress mediated corrosion in **Chapter 7** showed that localized stresses are

an indicator of localized corrosion at the cathodic particles but not at the overall material, with the early breakage of the protective layer formed by the passive alumina and the corrosion product buildup accelerating the degradation in the material. Therefore, it is concluded that corrosion is a multivariable mechanism driven by the local electrochemistry, the breakage of the protective layer, and the local stresses. Physically speaking, the stresses are an indicator of elongated atomic bonds that may facilitate electrochemical interactions with the environment, whereas strains are mainly an indicator of prior dislocation activity. It should be noted that strain is a relative term and not an internal state variable of the material. Hence, the high strain values do not translate in a facilitation of electrochemical interactions. While the residual strains are due to additional dislocation content, generally speaking, the continuum description of the stress field around dislocation (s) is(are) an order of magnitude lower that the stresses obtained from an actively loaded material. Hence, the residual strains do not play a significant role in the environmental degradation of the material.

For the study of fatigue crack initiation in part 4, a multivariable 3D reconstruction of pre-corroded materials containing information about the microstructure, the corrosion morphology, and the cathodic particles was generated from different types of corrosion morphologies, as seen in **Chapter 8**. EVP-FFT was used to model the multivariable reconstructions and the resulting micromechanical fields were used to calculate FIPs. High FIP values were capable of predicting crack initiation points, with the best crack initiation predictions occurring at the crack plane of the fissure corrosion specimens. Upon examination of the different mechanisms affecting crack initiation, it was concluded that the microstructure and the corrosion topography play a vital role in crack initiation with the constituent particles playing a less significant role, and that the predictions would improve if a) the characterization uncertainty away from the crack plane was minimized and b) if the resolution of the reconstructions was more refined so that the finer corrosion morphologies as well as the smaller cathodic particles could be better captured.

Overall, this thesis concludes that both corrosion growth and its transition to fatigue crack initiation are driven by mechanics that are acting simultaneously, where the local electrochemistry and micromechanics play a key role, and that there is a great opportunity for improving the design,

manufacturing, and repair processes in environmentally degraded materials by studying corrosion from a multivariable perspective.

9.2 Recommendations

Given the results obtained in the present document, the following recommendations are suggested for any related work:

1. The use of 3D microstructural characterizations of the material will not only expedite the ability to capture both statistically and spatially the micromechanical fields in crystal plasticity models, but also validate the effect that the subsurface uncertainty has on such an anisotropic material.
2. For stress mediated corrosion studies, in situ characterizations of the material when exposed to a corrosive environment may aid in more reliable characterizations of the evolution of corrosion as it will prevent the disruption of the acting chemistry that occurs when the specimens are removed from the corroding environment and cleaned.
3. An analysis of the effect that the corrosion intervals have on the evolution of localized corrosion may be useful in determining an optimal experimental schedule, such that the evolution of pitting can be properly captured without having to perform excessive characterization of the material which in turn requires additional specimen preparation and instrument availability.
4. For the analysis of pit-to-crack transition, the reconstructions may profit from XCT characterizations of the corrosion morphology prior to fatigue testing as well as full 3D microstructure characterizations such that the uncertainty arising from the reconstruction techniques are minimized. The location of crack initiation can be further located by early characterization of the crack when it is opened.

9.3 Future Work

For materials exposed to environmental degradation, crack growth is a mechanism of interest. The FIPs distributions calculated to study crack on pre-corroded materials can be further used to predict crack growth rates as well as its preferred direction by correlating FIP densities with the marker

bands that were experimentally generated at the cracked surface of each specimen. In partnership with the Burns Research Group at University of Virginia, the FIP distributions will be analyzed relative to the marker bands to elucidate the role of the microstructure, the geometry of the crack, and the presence of the cathodic particles, on the growth of a crack exposed to a corrosive environment.

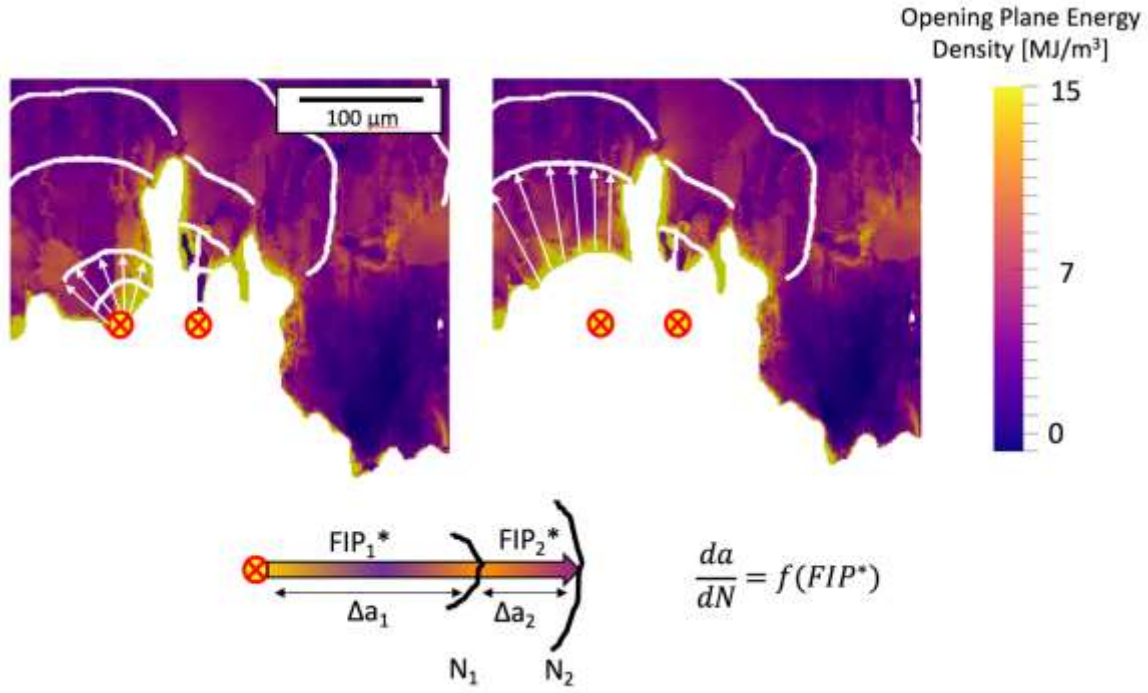

Fig 9.2 Future work: study of crack growth in AA7050 exposed to a corrosive environment using FIP densities and the location of marker bands.

APPENDIX A. FABRICATION OF SPECIMENS WITH THROUGH THICKNESS GRAIN STRUCTURE

To create specimens with a through thickness grain size to mimic columnarity, albeit in an approximate fashion, a plate of standard AA7050 material was melted to cast the material. The experimental setup used to obtain the directionally solidified microstructure is shown in **Fig. A1,** following the methodology discussed in [138][139]. An alumina crucible of 70 mm diameter was wrapped with a thermal insulator and the entire assembly was heated to 800 °C in a box furnace. The AA7050 stock was melted and heated to 850 °C (210 °C superheat) in a clay-graphite crucible using an open-air induction furnace. The heated mold assembly was then removed from the furnace and placed on a 40 mm thick copper chill plate. The molten aluminum was poured into the heated mold. The setup was designed to maximize the temperature gradient in the vertical direction between the cold plate and hot molten metal, and minimize the gradient in the transverse direction. Thus, the material would directionally solidify forming long dendrites vertically within the mold. The objective is to have specimens cut perpendicular to the dendrite formation to achieve specimens with through thickness grain structure.

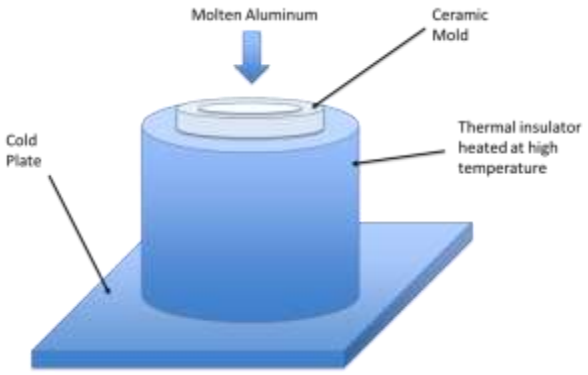

Fig A.3 Schematic for casting AA7050

The casting was removed from the mold. One side of the sectioned block was polished and etched, and the unidirectional preference of grains and dendrites was visually verified to be in the longitudinal direction. After identifying the longitudinal preference of the grains, two blocks were cut and treated to heat treatment condition T7451, with the rolling direction along the

orientation of the elongated dendrites. Specimens were then machined from the final blocks. To ensure that the through-thickness grain microstructure was completely accommodated into the stress relieved condition of T7451 (a treatment that requires pre-deformation), the specimens were subjected to a 2% axial cold work.

For these through-thickness cast AA7050 specimens with average planar grain size of ~106 μm, a ROI of 1,600 μm x 1,200 μm was delimited at the center to assure the characterization of a significant number of grains. For a precise match of the areas of interest between the front and back sides of the through-thickness cast AA7050 specimens, a transparent mask was used to determine the center of the gage section. During this process, both the specimen and mask were flipped for indentation on the specimen's backside.

To quantify the through-thickness condition on the AA7050 specimens, EBSD was performed on the front and back, as shown in **Fig. A2**. The back face EBSD inverse pole figure was flipped vertically for comparison with respect to the same direction. The lattice orientations were also mirrored to coincide with the same view as the front face. The grains were numbered from one to nine for grains that could be identified in the front and back of the specimen (**Fig. A2**), covering the extended area of interest of 1,600 μm x 1,200 μm in the front, and a larger area on the back to facilitate the grain identification. It is observed that at least 70% of the grains resolved by EBSD on the front side could be identified on the backside, for the specimen shown. The result is also coherent with the sequence of grain identifications numbers as marked on the front- and back-sides. The difference between the front and back faces shows that the material is not perfectly columnar. All of the cast specimens selected for testing exhibited the same characteristics, having >70% of the grains going completely through the thickness. This result was considered satisfactory for the purpose of the case study. Constituent particle distribution and void content of the fabricated columnar specimens are consistent with that of rolled plate AA7050-T7451.

.

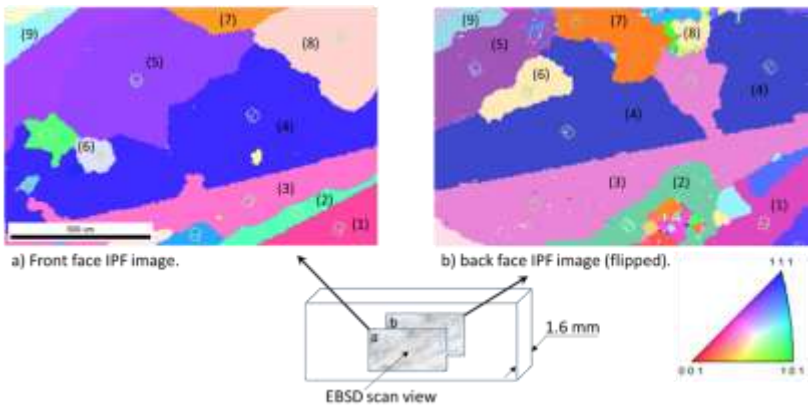

Fig A.4 Schematics of the EBSD characterization from a specimen (a) front and (b) back face, and their respective inverse pole figures.

To obtain a through-thickness grain structure of the fabricated AA7050 samples required that this material had a relatively large grain size. For DIC analysis of this large grain structure, a micro stamping procedure was used since it provides a repeatable, high-resolution, patterning method capable of covering large surface areas in which a stamp surface pattern is replicated on the material's surface [48]. To create the flexible micro textured stamps, a binary image with randomly distributed features was generated. The pattern distribution was designed such that: (i) The speckle population is set to be between 21-26% of the covered area and (ii) no more than two features can be connected side by side. Once the reference image was designed, the pattern was replicated using electron-beam lithography for generating the stamp master [103].

A flexible casting material able to conform to sub-micron features was selected to be vacuum cast to the master. It should be noted that the castable material must polymerize without shrinking, to guarantee that precise micro textures are replicated. In the present case study, we used a stamp with 2 μm features to allow a sub grain spatial strain resolution. To improve the adhesion of the photoresist during the stamping process, a primer was applied beforehand. For the present case study, we used MicroChem Corp MCC Primer 80/20, based on a combination of 20% HMDS (Hexamethyldisilazane) and 80% PM Acetate (1-Methoxy-2- propanol acetate). The primer was cured for 3 minutes at 115 °C on a hot plate. To create the visible pattern elements on the surface, we used micro-deposit Shipley 1805 photoresist. The photoresist was dropped on the specimen surface to be patterned and the stamp was pressed on the top. A pressure of 28 kPa was

applied on the stamp for 3 minutes at 115 °C. After 3 minutes, the pressure was removed and the stamp was peeled from the specimen. After checking the pattern for consistency, the specimen was ready for use in the tensile DIC experiment.

The through-thickness AA7050 specimens were deformed to slightly above 1% total strain and unloaded, so that the material was mechanically deformed past the yield point of the material. It should be noted that the through-thickness cast AA7050 samples exhibit a lower 0.2% offset yield stress of 356 MPa, below the 440 MPa reported for conventional AA7050-T7451 in the TS direction [110]. This is explained by the significantly larger grain size in these samples and the through-thickness grains not offering the same 3D constraints that are customary in the bulk material. As a consequence, the Voce hardening parameters (Eq. 4) were recalibrated to macroscopic stress-strain curves for these specimens, where $\tau_0 = 142.5$ MPa, $\tau_1 = 12$ MPa, $\theta_0 = 30$ MPa, and $\theta_1 = 5$ MPa.

APPENDIX B. RECONSTRUCTION ALGORITHM

1. **READ** H5 microstructure file with *FeatureIDs* and *EulerAngles* (from DREAM3D)
2. **SET** final depth *n* for 3D reconstruction
3. **SET** stereological growth factor *growthdepth* = 4/pi

GEOMETRIC RECONSTRUCTION

4. **GET** spatial sizes *x* and *y* from *FeatureIDs*
5. **CREATE** list of entire 3D spatial coordinates *allcoords* of size *x*y*n*
6. **CREATE** extruded grains *ExtrudedFIDs* of depth n from 2D *FeatureIDs* data
7. **CREATE** zero array *FinalFIDs* of size [*x y n*]

Surface Stereological Projection

FOR *grain* = 1 : length(*FeatureIDs*)

a. **FIND** 2D spatial grain centroid *centroid* for *grain*
b. **FIND** 2D equivalent grain radius *radius* for *grain*
c. **SELECT** 3D coordinates from *allcords* where *ExtrudedFIDs* == *grain*
d. **WRITE** selected 3D coordinates as *eachgraincoords*
e. **CALCULATE** distances *drange* between *eachgraincoords* and *centroid*
    i. This step finds euclidean distances, limited by the extruded grain
f. **RESELECT** 3D coordinates from *eachgraincoords* via stereological factor
    i. *drange* ≤ *radius*growthdepth* → *(4r/pi)*
g. **REWRITE** reselected 3D coordinates as *eachgraincoords*
h. **SET** *FinalFIDs* == *grain* where points belong to *eachgraincoords*

END

Subsurface Tessellation

8. **SET** number of seed points *nseeds* for subsurface tessellation (*nseeds* =1000)
9. **SELECT** 3D coordinates from *allcoords* where *FinalFIDs* == 0 (no defined grain)
10. **WRITE** selected 3D coordinates as *synthcoords*
11. **SELECT** randomly *nseed* coordinates from *synthcoords*
12. **WRITE** selected 3D coordinates as *seedpoints*
13. **REWRITE** z portion of seedpoints to enforce average grain length seen on TL
14. **CALCULATE** k-nearest neighbor in *seedpoints* for each *synthcoords* and WRITE as

a. *synthgrainmap* = knnsearch(*seedpoints*,*synthcoords*,'K',1)

b. This is the main step behind tessellation.

15. **GET** next available grain ID for tessellating grains *g* = max(*FeatureIDs*)+1

FOR s*point* = 1:length(*seedpoints*)

a. **SELECT** coordinates from *synthcoords* where *synthgrainmap* == *spoint*

b. **WRITE** selected coordinates as *eachsynthcoords*

c. **SET** *FinalFIDs* == *g* + *spoint* where points belong to *eachsynthcoords*

END

Grain Boundary Smoothing Algorithm

This is a standalone algorithm that can be skipped if the tessellation geometry is acceptable

16. **LOAD** *FinalFIDs* data
17. **CREATE** zero array *grainIDnew* of size(*FinalFIDs*)
18. **SELECT** level of smoothing *s* = 1…5;
19. **CREATE** smoothing kernel sphere *kernelsphere* of diameter *s*
    a. *kernelsphere* = strel(sqrt(X.^2 + Y.^2 + Z.^2) <=*s*)
20. **OBTAIN** grain boundaries as binary *GB*
21. **DILATE** binary grain boundaries *GB* using *kernelsphere*
22. **ERODE** binary grain boundaries *GB* using *kernelsphere*
23. **RESELECT** *FinalFIDs* using *GB* as mask and WRITE to *grainIDnew*
24. **SET** *grainIDnew* == 0 where points belong to dilated *GB*
25. **CALCULATE** Euclidean distances *ECL* inside dilated GBs ; *grainIDnew* == 0

FOR stepcount = 1 : max(*ECL*)

i. **FIND** locations *borderlocs* were *ECL* == 0 (locations bordering grains)

FOR *loc* = 1 : length(*borderlocs*)

a. FIND all *FinalFIDs* values neighboring *loc* (*grainID_loc*)

b. SELECT max(*grainID_loc*)

c. SET *grainIDnew*(*loc*) == max(*grainID_loc*)

END

ii. **RECALCULATE** Euclidean distances *ECL*

IF ECL is empty

i. **STOP** loop; *grainIDnew* is fully populated with smoothed grains

END

26. **REPLACE** first slice on *grainIDnew* with original EBSD slice in *FinalFIDs*
27. **RENAME** *grainIDnew* as *FinalFIDs* and WRITE to output

Orientation Reconstruction - Creating Statistical Orientations

28. **OPEN** Dream3D
29. **READ** H5 file containing sizes, orientations, ratios, etc. (from Dream3D)
30. **CREATE** statistical orientations datafile using *StatsGenerator* command
31. **CLOSE** Dream3D

Assigning Orientations

32. **READ** CSV datafile containing statistical orientations
33. **CREATE** extruded orientation *FinalEuler* of depth n from 2D *EulerAngles* data
    a. *FinalEuler* is of size [*x y n* 3]
34. **GET** randomly *nseed* orientations from *CSV* orientation list (*rEuler_Tess*)
    a. *rEuler_Tess* is of size [*nseed* 3]
35. **GET** all grain IDs belonging to tessellated grains (*GrainIDs_Tess*)

FOR ii = 1 : length(*GrainIDs_Tess*)

a. SELECT a statistically equivalent orientation *t_euler* == *rEuler_tess*(ii)
b. SELECT coordinates from *allcoords* where *FinalFIDs* == *GrainIDsTess*(ii)
c. WRITE selected 3D coordinates as *eachgraincoords*
d. SET *FinalEuler* == *t_euler* where points belong to *eachgraincoords*

END

36. **SAVE** *FinalFIDs*. Output is a matrix of size [*x y n* 1]
37. **SAVE** *FinalEuler* Output is a matrix of size [*x y n* 3]

REFERENCES

[1] E.F. Hertzberg, S. Guo, R.F. Stroh, T.K. Chan, A. Morris, A. Stevenson, Estimated Impact of Corrosion on Cost and Availability of DoD Weapon Systems: FY2018 Update, LMI, Virginia, 2018.

[2] G.A. Shoales, S.A. Fawaz, M.R. Walters, Compilation of damage findings from multiple recent teardown analysis programs, in: Bridg. Gap between Theory Oper. Pract. 25th ICAF Symp., 2009: pp. 187–207. doi:10.1007/978-90-481-2746-7_11.

[3] M.E. Hoffman, P.C. Hoffman, Corrosion and fatigue research—structural issues and relevance to naval aviation, Int. J. Fatigue. 23 (2001) 1–10.

[4] N.E.C. Co, J.T. Burns, Galvanic corrosion-induced fatigue crack initiation and propagation behavior in AA7050-T7451, Corrosion. 72 (2016) 1215–1219. doi:10.5006/2132.

[5] W. Li, D.Y. Li, Influence of surface morphology on corrosion and electronic behavior, Acta Mater. 54 (2006) 445–452. doi:10.1016/j.actamat.2005.09.017.

[6] K.D. Ralston, N. Birbilis, Effect of grain size on corrosion: A review, Corrosion. 66 (2010) 0750051–07500513. doi:10.5006/1.3462912.

[7] C. Ornek, D.L. Engelberg, SKPFM measured Volta potential correlated with strain localisation in microstructure to understand corrosion susceptibility of cold-rolled grade 2205 duplex stainless steel, Corros. Sci. 99 (2015) 164–171. doi:10.1016/j.corsci.2015.06.035.

[8] S.P. Knight, M. Salagaras, A.M. Wythe, F. De Carlo, A.J. Davenport, A.R. Trueman, In situ X-ray tomography of intergranular corrosion of 2024 and 7050 aluminium alloys, Corros. Sci. 52 (2010) 3855–3860. doi:10.1016/j.corsci.2010.08.026.

[9] M. Chaussumier, C. Mabru, R. Chieragatti, M. Shahzad, Fatigue life model for 7050 chromic anodized aluminium alloy, in: Procedia Eng., 2013: pp. 300–312. doi:10.1016/j.proeng.2013.12.085.

[10] A. Ben Rhouma, H. Sidhom, C. Braham, J. Lédion, M.E. Fitzpatrick, Effects of surface preparation on pitting resistance, residual stress, and stress corrosion cracking in austenitic stainless steels, J. Mater. Eng. Perform. 10 (n.d.) 507–514. doi:10.1361/105994901770344638.

[11] C. Montero-Ocampo, L. Veleva, Effect of cold reduction on corrosion of carbon steel in aerated 3% sodium chloride, Corrosion. 58 (2002) 601–607. doi:10.5006/1.3277651.

[12] Z.A. Foroulis, H.H. Uhlig, Effect of Cold-Work on Corrosion of Iron and Steel in Hydrochloric Acid, J. Electrochem. Soc. 111 (1964) 522–528. doi:10.1149/1.2426172.

[13] D. Nickel, D. Dietrich, T. Mehner, P. Frint, D. Spieler, T. Lampke, Effect of Strain Localization on Pitting Corrosion of an AlMgSi0.5 Alloy, Metals (Basel). 5 (2015) 172–191. doi:10.3390/met5010172.

[14] G. Hamu, D. Eliezer, L. Wagner, The relation between severe plastic deformation microstructure and corrosion behavior of AZ31 magnesium alloy, J. Alloys Compd. 468 (2009) 222–229. doi:http://dx.doi.org/10.1016/j.jallcom.2008.01.084.

[15] J.M. Zhang, M.A. Przystupa, A.J. Luevano, Characterizations of pore and constituent particle populations in 7050-T7451 aluminum plate alloys, Metall. Mater. Trans. a-Physical Metall. Mater. Sci. 29 (1998) 727–737. doi:DOI 10.1007/s11661-998-0263-2.

[16] B.R. Crawford, C. Loader, A.R. Ward, C. Urbani, M.R. Bache, S.H. Spence, et al., The EIFS distribution for anodized and pre-corroded 7010-T7651 under constant amplitude loading, Fatigue Fract. Eng. Mater. Struct. (2005). doi:10.1111/j.1460-2695.2005.00912.x.

[17] J.T. Burns, S. Kim, R.P. Gangloff, Effect of corrosion severity on fatigue evolution in Al-Zn-Mg-Cu, Corros. Sci. 52 (2010) 498–508. doi:10.1016/j.corsci.2009.10.006.

[18] E.J. Dolley, B. Lee, R.P. Wei, Effect of pitting corrosion on fatigue life, Fatigue Fract. Eng. Mater. Struct. (2000). doi:10.3760/cma.j.issn.0366-6999.2012.18.009.

[19] C.M. Liao, R.P. Wei, Galvanic coupling of model alloys to aluminum - a foundation for understanding particle-induced pitting in aluminum alloys, Electrochim. Acta. (1999). doi:10.1016/S0013-4686(99)00299-6.

[20] N. Birbilis, R.G. Buchheit, Electrochemical Characteristics of Intermetallic Phases in Aluminum Alloys, J. Electrochem. Soc. 152 (2005) B140. doi:10.1149/1.1869984.

[21] N. Birbilis, Cavanaugh, M.K. Cavanaugh, R.G. Buchheit, Electrochemical behavior and localized corrosion associated with Al7Cu2Fe particles in aluminum alloy 7075-T651, Corros. Sci. 48 (2006) 4202–4215. doi:10.1016/j.corsci.2006.02.007.

[22] F.X. Song, X.M. Zhang, S.D. Liu, N.M. Han, D.F. Li, Anisotropy of localized corrosion in 7050-T7451 Al alloy thick plate, Trans. Nonferrous Met. Soc. China (English Ed. 23 (2013) 2483–2490. doi:10.1016/S1003-6326(13)62758-2.

[23] E. Nizery, H. Proudhon, J.-Y. Buffiere, P. Cloetens, T.F. Morgeneyer, S. Forest, Three-dimensional characterization of fatigue-relevant intermetallic particles in high-strength aluminium alloys using synchrotron X-ray nanotomography, Philos. Mag. 95 (2015) 2731–2746. doi:10.1080/14786435.2015.1076940.

[24] S. Suresh, Fatigue of Materials. pp. 79-83. (1998)

[25] K. Jones, D.W. Hoeppner, Pit-to-crack transition in pre-corroded 7075-T6 aluminum alloy under cyclic loading, Corros. Sci. 47 (2005) 2185–2198. doi:10.1016/j.corsci.2004.10.004.

[26] N.E.C., Co, N. E. C., J.T. Burns, Effects of macro-scale corrosion damage feature on fatigue crack initiation and fatigue behavior, Int. J. Fatigue. 103 (2017) 234–247. doi:10.1016/j.ijfatigue.2017.05.028.

[27] P.S., Pao, C.R. Feng, S.J. Gill, Corrosion fatigue crack initiation in aluminum alloys 7075 and 7050, Corrosion. 56 (2000) 1022–1031. doi:10.5006/1.3294379.

[28] T.P. HOAR, Stress-Corrosion Cracking, Corrosion. 19 (1963) 331t–338t. doi:10.5006/0010-9312-19.10.331.

[29] M.D. Sangid, The physics of fatigue crack initiation, Int. J. Fatigue. 57 (2013) 58–72. doi:10.1016/j.ijfatigue.2012.10.009.

[30] Y. Pang, R. Huang, Nonlinear effect of stress and wetting on surface evolution of epitaxial thin films, Phys. Rev. B - Condens. Matter Mater. Phys. (2006). doi:10.1103/PhysRevB.74.075413.

[31] J.O. Bogkris, W. Beck, M.A. Genshaw, P.K. Subramanyan, F.S. Williams, The effect of stress on the chemical potential of hydrogen in iron and steel, Acta Metall. 19 (1971) 1209–1218. doi:https://doi.org/10.1016/0001-6160(71)90054-X

[32] G. Salvago, G. Fumagalli, D. Sinigaglia, The corrosion behavior of AISI 304L stainless steel in 0.1 M HCl at room temperature-II. The effect of cold working, Corros. Sci. (1983). doi:10.1016/0010-938X(83)90101-4.

[33] P. Kramer, F. Friedersorf, M. Merrill, C.M. Hargarter, S.A. Policastro, M. Kim, N. Brown, Relationship between electrochemical processes and environment-assisted crack growth under static and dynamic atmospheric conditions, Corros. Rev. (2017). doi:10.1515/corrrev-2017-0002.

[34] C.M. Liao, J.M. Olive, M. Gao, R.P. Wei, In-Situ Monitoring of Pitting Corrosion in Aluminum Alloy 2024, Corrosion. (1998). doi:10.5006/1.3284873.

[35] W.Y. Guo, J. Sun, J.S. Wu, Effect of deformation on corrosion behavior of Ti-23Nb-0.7Ta-2Zr-O alloy, Mater. Charact. (2009). doi:10.1016/j.matchar.2008.08.006.

[36] L.Y. Xu, Y.F. Cheng, Development of a finite element model for simulation and prediction of mechanoelectrochemical effect of pipeline corrosion, Corros. Sci. 73 (2013) 150–160. doi:10.1016/j.corsci.2013.04.004.

[37] A.M. Glenn, A.E. Hughes, A. Torpy, G. Nolze, N. Birbilis, Defect density associated with constituent particles in AA2024-T3 and its role in corrosion, Surf. Interface Anal. 48 (2016) 780–788. doi:10.1002/sia.5813.

[38] A. King, G. Johnson, D. Engelberg, W. Ludwig, J. Marrow, Observations of Intergranular Stress Corrosion Cracking in a Grain-Mapped Polycrystal, Science (80). 321 (2008) 382–385. doi:10.1126/science.1156211.

[39] K.D. Ralston, N. Birbilis, C.H.J. Davies, Revealing the relationship between grain size and corrosion rate of metals, Scr. Mater. 63 (2010) 1201–1204. doi:10.1016/j.scriptamat.2010.08.035.

[40] C.M. Barr, S. Thomas, J.L. Hart, W. Harlow, E. Anber, M.L. Taheri, Tracking the evolution of intergranular corrosion through twin-related domains in grain boundary networks, Npj Mater. Degrad. 2 (2018) 14. doi:10.1038/s41529-018-0032-7.

[41] A. Barbucci, G. Cerisola, P.L. Cabot, Effect of cold-working in the passive behavior of 304 stainless steel in sulfate media, J. Electrochem. Soc. 149 (2002) B534–B542. doi:Doi 10.1149/1.1516774.

[42] J.G. Brunner, J. May, H.W. Höppel, M.Göken, S. Virtanen, Localized corrosion of ultrafine-grained Al-Mg model alloys, Electrochim. Acta. 55 (2010) 1966–1970. doi:10.1016/j.electacta.2009.11.016.

[43] W.Z. Abuzaid, M.D. Sangid, J.D. Carroll, H. Sehitoglu, J. Lambros, Slip transfer and plastic strain accumulation across grain boundaries in Hastelloy X, J. Mech. Phys. Solids. 60 (2012) 1201–1220. doi:10.1016/j.jmps.2012.02.001.

[44] M. Sutton, W. Wolters, W. Peters, W. Ranson, S. McNeill, Determination of displacements using an improved digital correlation method, Image Vis. Comput. 1 (1983) 133–139. doi:10.1016/0262-8856(83)90064-1.

[45] A. Kammers, S. Daly, Deformation mapping at the microstructural length scale, in: Conf. Proc. Soc. Exp. Mech. Ser., 2013: pp. 15–20. doi:10.1007/978-1-4614-4226-4_2.

[46] J. Tracy, A. Waas, S. Daly, A New Experimental Approach for In Situ Damage Assessment in Fibrous Ceramic Matrix Composites at High Temperature, J. Am. Ceram. Soc. 98 (2015) 1898–1906. doi:10.1111/jace.13538.

[47] A.W. Mello, A. Nicolas, M.D. Sangid, Fatigue strain mapping via digital image correlation for Ni-based superalloys: The role of thermal activation on cube slip, Mater. Sci. Eng. A. 695 (2017) 332–341. doi:10.1016/j.msea.2017.04.002.

[48] A.H. Cannon, J.D. Hochhalter, A.W. Mello, G.F. Bomarito, M.D. Sangid, MicroStamping for Improved Speckle Patterns to Enable Digital Image Correlation, Microsc. Microanal. 21 (2015) 451–452. doi:10.1017/S1431927615003050.

[49] R.J. Asaro, R. J., (1983), Micromechanics of Crystals and Polycrystals, in: J.W.H. and T.Y.W.B.T.-A. in A. Mechanics (Ed.), Elsevier, 1983: pp. 1–115. doi:http://dx.doi.org/10.1016/S0065-2156(08)70242-4.

[50] S.R. Kalidindi, C.A. Bronkhorst, L. Anand, Crystallographic texture evolution in bulk deformation processing of FCC metals, J. Mech. Phys. Solids. (1992). doi:10.1016/0022-5096(92)80003-9.

[51] R.J. Asaro, Crystal Plasticity, J. Appl. Mech. 50 (1983) 921. doi:10.1115/1.3167205.

[52] T.J. Turner, P. a Shade, J.C. Schuren, M. a Groeber, The influence of microstructure on surface strain distributions in a nickel micro-tension specimen, Model. Simul. Mater. Sci. Eng. 21 (2013) 015002. doi:10.1088/0965-0393/21/1/015002.

[53] A.J. Beaudoin, K.K. Mathur, P.R. Dawson, G.C. Johnson, Three-dimensional deformation process simulation with explicit use of polycrystal plasticity models, Int. J. Plast. 9 (1993) 833–860. doi:http://dx.doi.org/10.1016/0749-6419(93)90054-T.

[54] D. Raabe, F. Roters, Using texture components in crystal plasticity finite element simulations, Int. J. Plast. 20 (2004) 339–361. doi:http://dx.doi.org/10.1016/S0749-6419(03)00092-5.

[55] R.A. Lebensohn, A.K. Kanjarla, P. Eisenlohr, An elasto-viscoplastic formulation based on fast Fourier transforms for the prediction of micromechanical fields in polycrystalline materials, Int. J. Plast. 32–33 (2012) 59–69. doi:10.1016/j.ijplas.2011.12.005.

[56] H. Moulinec, P. Suquet, A numerical method for computing the overall response of nonlinear composites with complex microstructure, Comput. Methods Appl. Mech. Eng. 157 (1998) 69–94. doi:10.1016/S0045-7825(97)00218-1.

[57] B. Liu, D. Raabe, F. Roters, P. Eisenlohr, R.A. Lebensohn, Comparison of finite element and fast Fourier transform crystal plasticity solvers for texture prediction, Model. Simul. Mater. Sci. Eng. 18 (2010) 085005. doi:10.1088/0965-0393/18/8/085005.

[58] A. Rovinelli, H. Proudhon, R.A. Lebensohn, M.D. Sangid, Assessing the Reliability of Fast Fourier Transform-Based Crystal Plasticity Simulations of a Polycrystalline Material near a Crack Tip, Int. J. Solids Struct. (2019). doi:https://doi.org/10.1016/j.ijsolstr.2019.02.024.

[59] M. Diehl, P. Shanthraj, P. Eisenlohr, F. Roters, Neighborhood influences on stress and strain partitioning in dual-phase microstructures, Meccanica. 51 (2016) 429–441. doi:10.1007/s11012-015-0281-2.

[60] C. Zhang, H. Li, P. Eisenlohr, W. Liu, C.J. Boehlert, M.A. Crimp, et al., Effect of realistic 3D microstructure in crystal plasticity finite element analysis of polycrystalline Ti-5Al-2.5Sn, Int. J. Plast. 69 (2015) 21–35. doi:10.1016/j.ijplas.2015.01.003.

[61] A. Zeghadi, F. N'Guyen, S. Forest, A.F. Gourgues, O. Bouaziz, Ensemble averaging stress-strain fields in polycrystalline aggregates with a constrained surface microstructure-part 1: Anisotropic elastic behaviour, in: Philos. Mag., 2007: pp. 1401–1424. doi:10.1080/14786430601009509.

[62] Z. Zhao, M. Ramesh, D. Raabe, A.M. Cuitiño, R. Radovitzky, Investigation of three-dimensional aspects of grain-scale plastic surface deformation of an aluminum oligocrystal, Int. J. Plast. 24 (2008) 2278–2297. doi:10.1016/j.ijplas.2008.01.002.

[63] H. Lim, J.D. Carroll, C.C. Battaile, B.L. Boyce, C.R. Weinberger, Quantitative comparison between experimental measurements and CP-FEM predictions of plastic deformation in a tantalum oligocrystal, Int. J. Mech. Sci. 92 (2015) 98–108. doi:10.1016/j.ijmecsci.2014.12.010.

[64] H. Lim, J.D. Carroll, C.C. Battaile, T.E. Buchheit, B.L. Boyce, C.R. Weinberger, Grain-scale experimental validation of crystal plasticity finite element simulations of tantalum oligocrystals, Int. J. Plast. 60 (2014) 1–18. doi:10.1016/j.ijplas.2014.05.004.

[65] X. Tu, A. Shahba, J. Shen, S. Ghosh, Microstructure and property based statistically equivalent RVEs for polycrystalline-polyphase aluminum alloys, Int. J. Plast. (2018). doi:https://doi.org/10.1016/j.ijplas.2018.12.002.

[66] J.A. Ewing, J.C.W. Humfrey, The Fracture of Metals under Repeated Alternations of Stress, Philos. Trans. R. Soc. A Math. Phys. Eng. Sci. (2006). doi:10.1098/rsta.1903.0006.

[67] A.W. Thompson W.A. Backofen, The effect of grain size on fatigue, Acta Metall. (1971). doi:10.1016/0001-6160(71)90012-5.

[68] Z.F. Zhang, Z.G. Wang, Comparison of fatigue cracking possibility along large- and low-angle grain boundaries, Mater. Sci. Eng. A. (2000). doi:10.1016/S0921-5093(00)00796-6.

[69] N.H. Paulson, M.W. Priddy, D.L. McDowell, and S.R. Kalidindi: Mater. Des., 2018, vol. 154, pp. 170–83. doi: 10.1016/j.matdes.2018.05.009

[70] M.D. Sangid, H.J. Maier, H. Sehitoglu, A physically based fatigue model for prediction of crack initiation from persistent slip bands in polycrystals, Acta Mater. (2011). doi:10.1016/j.actamat.2010.09.036.

[71] F.P.E. Dunne, D. Rugg, On the mechanisms of fatigue facet nucleation in titanium alloys, Fatigue Fract. Eng. Mater. Struct. (2008). doi:10.1111/j.1460-2695.2008.01284.x.

[72] P. Veerappan, M.D. Sangid, The role of defects and critical pore size analysis in the fatigue response of additively manufactured IN718 via crystal plasticity, Mater. Des. (2018). doi:10.1016/j.matdes.2018.04.022.

[73] Y. Kondo, Prediction of fatigue crack initiation life based on pit growth, Corrosion. (1989). doi:10.5006/1.3577891.

[74] A. Turnbull, Corrosion pitting and environmentally assisted small crack growth, Proc. R. Soc. A Math. Phys. Eng. Sci. 470 (2014). doi:10.1098/rspa.2014.0254.

[75] A. Turnbull, L.N. McCartney, S. Zhou, A model to predict the evolution of pitting corrosion and the pit-to-crack transition incorporating statistically distributed input parameters, in: Environ. Crack. Mater., 2008. doi:10.1016/B978-008044635-6.50006-6.

[76] T. Magnin, A. Chambreuil, B. Bayle, The corrosion-enhanced plasticity model for stress corrosion cracking in ductile fcc alloys, Acta Mater. 44 (1996) 1457–1470. doi:https://doi.org/10.1016/1359-6454(95)00301-0.

[77] J.T. Burns, J.M. Larsen, R.P. Gangloff, Driving forces for localized corrosion-to-fatigue crack transition in Al-Zn-Mg-Cu, Fatigue Fract. Eng. Mater. Struct. (2011). doi:10.1111/j.1460-2695.2011.01568.x.

[78] N.O. Larrosa, R. Akid, R.A. Ainsworth, Corrosion-fatigue: a review of damage tolerance models, Int. Mater. Rev. 63 (2018) 283–308. doi:10.1080/09506608.2017.1375644.

[79] L. Salvo, P. Cloetens, E. Maire, S. Zabler, J.J. Blandin, J.Y. Buffière, W. Ludwig, E. Boller, D. Bellet, C. Josserond, X-ray micro-tomography an attractive characterisation technique in

materials science, in: Nucl. Instruments Methods Phys. Res. Sect. B Beam Interact. with Mater. Atoms, 2003. doi:10.1016/S0168-583X(02)01689-0.

[80] S.T. Carter, J. Rotella, R.F. Agyei, X. Xiao, M.D. Sangid, Measuring fatigue crack deflections via cracking of constituent particles in AA7050 via in situ x-ray synchrotron-based micro-tomography, Int. J. Fatigue. 116 (2018) 490–504. doi:https://doi.org/10.1016/j.ijfatigue.2018.07.005.

[81] B.J. Connolly, D.A. Horner, S.J. Fox, A.J. Davenport, C. Padovani, S. Zhou, A. Turnbull, M. Preuss, N.P. Stevens, T.J. Marrow, J.-Y. Buffiere, E. Boller, A. Groso, M. Stampanoni, X-ray microtomography studies of localised corrosion and transitions to stress corrosion cracking, Mater. Sci. Technol. (2006). doi:10.1179/174328406X114199.

[82] K. Madi, S. Forest, M. Boussuge, S. Gailliègue, E. Lataste, J.Y. Buffière, D. Bernard, D. Jeulin, Finite element simulations of the deformation of fused-cast refractories based on X-ray computed tomography, Comput. Mater. Sci. (2007). doi:10.1016/j.commatsci.2006.01.033.

[83] M. Shenoy, J. Zhang, D.L. McDowell, Estimating fatigue sensitivity to polycrystalline Ni-base superalloy microstructures using a computational approach, Fatigue Fract. Eng. Mater. Struct. (2007). doi:10.1111/j.1460-2695.2007.01159.x.

[84] D.L. McDowell, F.P.E. Dunne, Microstructure-sensitive computational modeling of fatigue crack formation, Int. J. Fatigue. 32 (2010) 1521–1542. doi:10.1016/j.ijfatigue.2010.01.003.

[85] J.D. Hochhalter, D.J. Littlewood, R.J. Christ, M.G. Veilleux, J.E. Bozek, A.R. Ingraffea, A.M. Maniatty, A geometric approach to modeling microstructurally small fatigue crack formation: II. Physically based modeling of microstructure-dependent slip localization and actuation of the crack nucleation mechanism in AA 7075-T651, Model. Simul. Mater. Sci. Eng. 18 (2010) 045004. doi:10.1088/0965-0393/18/4/045004.

[86] S. Sheen, G. Bao, P. Cooke, Food surface texture measurement using reflective confocal laser scanning microscopy, J. Food Sci. 73 (2008). doi:10.1111/j.1750-3841.2008.00787.x.

[87] F. Bachmann, R. Hielscher, H. Schaeben, Texture Analysis with MTEX – Free and Open Source Software Toolbox, Solid State Phenom. (2010). doi: 10.4028/www.scientific.net /SSP.160.63.

[88] A.D. Kammers, S. Daly, Self-Assembled Nanoparticle Surface Patterning for Improved Digital Image Correlation in a Scanning Electron Microscope, Exp. Mech. 53 (2013) 1333–1341. doi:10.1007/s11340-013-9734-5.

[89] A.W. Mello, T.A. Book, A. Nicolas, S.E. Otto, C.J. Gilpin, M.D. Sangid, Distortion Correction Protocol for Digital Image Correlation after Scanning Electron Microscopy: Emphasis on Long Duration and Ex-Situ Experiments, Exp. Mech. 57 (2017) 1395–1409. doi:10.1007/s11340-017-0303-1.

[90] C. Tome, C., Canova, G.R., Kocks, U.F., Christodoulou, N., Jonas, J.J., (1984). The relation between macroscopic and microscopic strain hardening in F.C.C. polycrystals. Acta Metall. doi:10.1016/0001-6160(84)90222-0.

[91] A. Rovinelli, Y. Guilhem, H. Proudhon, R.A. Lebensohn, W. Ludwig, M.D. Sangid, Assessing the Reliability of Fast Fourier Transform-Based Crystal Plasticity Simulations of a Polycrystalline Material near a Crack Tip, Int. J. Solids Struct. (2019). doi:https://doi.org/10.1016/j.ijsolstr.2019.02.024

[92] A. Rovinelli, R.A. Lebensohn, M.D. Sangid, Influence of microstructure variability on short crack behavior through postulated micromechanical short crack driving force metrics, Eng. Fract. Mech. 138 (2015) 265–288. doi:10.1016/j.engfracmech.2015.03.001.

[93] A. Fatemi, D.F. Socie. A Critical Plane Approach To Multiaxial Fatigue Damage Including Out-Of-Phase Loading, Fatigue Fract. Eng. Mater. Struct. (1988). doi:10.1111/j.1460-2695.1988.tb01169.x.

[94] A. Clair, M. Foucault, O. Calonne, Y. Lacroute, L. Markey, M. Salazar, V. Vignal, E. Finot, Strain mapping near a triple junction in strained Ni-based alloy using EBSD and biaxial nanogauges, Acta Mater. 59 (2011) 3116–3123. doi:10.1016/j.actamat.2011.01.051.

[95] J. L. Carter, M. W. Kuper, M. D. Uchic, M. J. Mills, (2014). Characterization of localized deformation near grain boundaries of superalloy Rene-104 at elevated temperatures. Mat. Sci. & Eng. A 605, 127-136. doi:10.1016/j.msea.2014.03.048

[96] F. Di Gioacchino, J. Quinta da Fonseca, Plastic Strain Mapping with Sub-micron Resolution Using Digital Image Correlation, Exp. Mech. 53 (2013) 743–754. doi:10.1007/s11340-012-9685-2.

[97] J. Esquivel, M.D. Sangid, Digital image correlation of heterogeneous deformation in polycrystalline material with electron backscatter diffraction, Microsc. Microanal. 21 (2015) 1167–1168.

[98] C.C. Tasan, J.P.M. Hoefnagels, M. Diehl, D. Yan, F. Roters, D. Raabe, Strain localization and damage in dual phase steels investigated by coupled in-situ deformation experiments and crystal plasticity simulations, Int. J. Plast. 63 (2014) 198–210. doi:10.1016/j.ijplas.2014.06.004.

[99] AMS 4050J, (2014). Aluminum Alloy, Plate, 6.2Zn - 2.3Cu - 2.2Mg - 0.12Zr (7050-T7451), Solution Heat Treated, Stress Relieved, and Overaged. SAE International.

[100] ASTM E8 / E8M-13a, (2013). Standard Test Methods for Tension Testing of Metallic Materials, ASTM Int. 1–28. doi:10.1520/E0008_E0008M-11.

[101] C. Efstathiou, H. Sehitoglu, J. Lambros, Multiscale strain measurements of plastically deforming polycrystalline titanium: Role of deformation heterogeneities, Int. J. Plast. (2010). doi:10.1016/j.ijplas.2009.04.006.

[102] A.H. Cannon, M.C., Macguire, J.D., Hochhalter, (2015). US Patent Application 62116742.

[103] A.H. Cannon, W.P. King, Casting metal microstructures from a flexible and reusable mold, J. Micromechanics Microengineering. 19 (2009) 095016. doi:10.1088/0960-1317/19/9/095016.

[104] B.R. Crawford, P.K. Sharp, Equivalent Crack Size Modelling of Corrosion Pitting in an AA7050-T7451 Aluminum Alloy and its Implications for Aircraft Structural Integrity. Air Vehicles Division. (2012) Defence Science and Technology Organisation. DSTO-TR-2745. Australia.

[105] F. Roters, P. Eisenlohr, L. Hantcherli, D.D. Tjahjanto, T.R. Bieler, D. Raabe, Overview of constitutive laws, kinematics, homogenization and multiscale methods in crystal plasticity finite-element modeling: Theory, experiments, applications, Acta Mater. 58 (2010) 1152–1211. doi:http://dx.doi.org/10.1016/j.actamat.2009.10.058.

[106] R. Becker, Analysis of texture evolution in channel die compression—I. Effects of grain interaction, Acta Metall. Mater. 39 (1991) 1211–1230. doi:http://dx.doi.org/10.1016/0956-7151(91)90209-J.

[107] M. Groeber, T. Rollett, M. Jackson, D. Rowenhorst, G. Rohrer, (2015). Dream3D. Bluequartz Software. http://dream3d.bluequartz.net.

[108] M.D. Sangid, S.R. Yeratapally, A. Rovinelli, Validation of Microstructure-Based Materials Modeling. AAIA Journal. 55th AIAA/ASMe/ASCE/AHS/SC Structures, Structural Dynamics, and Materials Conference. January 14, (2014), National Harbor, Maryland. DOI: 10.2514/6.2014-0462.

[109] M.A. Groeber, Development of an Automated Characterization- Representation Framework for the Modeling of Polycrystalline Materials in 3D, PhD. thesis, The Ohio State University, 201 West 19th Avenue, Columbus, OH 43210, 2007.

[110] A.W. Mello, A. Nicolas, R.A. Lebensohn, M.D. Sangid, Effect of microstructure on strain localization in a 7050 aluminum alloy: Comparison of experiments and modeling for various textures, Mater. Sci. Eng. A. 661 (2016) 187–197. doi:10.1016/j.msea.2016.03.012.

[111] A.P Barten, The coefficient of determination for regression without a constant term, in: R. Heijmans, H. Neudecker (Eds.), Pract. Econom. Stud. Demand, Forecast. Money Income, Springer Netherlands, Dordrecht, 1987: pp. 181–189. doi:10.1007/978-94-009-3591-4_12.

[112] T. Dursun, C. Soutis, Recent developments in advanced aircraft aluminium alloys, Mater. Des. 56 (2014) 862–871. doi:10.1016/j.matdes.2013.12.002.

[113] G.S. Frankel, Pitting Corrosion of Metals A Review of the Critical Factors, J. Electrochem. Soc. 145 (1998) 2186–2198. doi:10.1149/1.1838615.

[114] J. Telesman, Review of the effects of microstructure on fatigue in aluminum alloys, NASA techn, National Aeronautics and Space Administration, Washington, D.C, 1984.

[115] Y. Liu, X.M. Zhang, H. Zhang, Role of secondary phase particles of 2519A aluminium alloy in localised corrosion, Mater. Res. Innov. 17 (2013) 83–88. doi:10.1179/1432891713Z.000000000187.

[116] R.G. Buchheit, N. Birbilis, Electrochemical microscopy: An approach for understanding localized corrosion in microstructurally complex metallic alloys, Electrochim. Acta. 55 (2010) 7853–7859. doi:10.1016/j.electacta.2010.04.046.

[117] S.S. Singh, C. Schwartzstein, J.J. Williams, X. Xiao, F. De Carlo, N. Chawla, 3D microstructural characterization and mechanical properties of constituent particles in Al 7075 alloys using X-ray synchrotron tomography and nanoindentation, J. Alloys Compd. 602 (2014) 163–174. doi:10.1016/j.jallcom.2014.03.010.

[118] S. Dray, T. Jombart, Revisiting Guerry's data: Introducing spatial constraints in multivariate analysis, Ann. Appl. Stat. 5 (2011) 2278–2299. doi:10.1214/10-AOAS356.

[119] C.E. Rasmussen, C.K.I. Williams, Gaussian processes for machine learning., 2004. doi:10.1142/S0129065704001899.

[120] J. Hensman, N. Fusi, N.D. Lawrence, Gaussian Processes for Big Data, in: UAI, 2013: pp. 282–290. doi:10.1162/089976699300016331.

[121] X.G. Zhang, Galvanic Corrosion, in: Uhlig's Corros. Handb. Third Ed., 2011: pp. 123–143. doi:10.1002/9780470872864.ch10.

[122] H.-J. Jordan, M. Wegner, H. Tiziani, Highly accurate non-contact characterization of engineering surfaces using confocal microscopy, Meas. Sci. Technol. 9 (1998) 1142–1151. doi:10.1088/0957-0233/9/7/023.

[123] A. Nicolas, A. Mello, M. Sangid, The effect of strain localization on galvanic corrosion pitting in AA7050, CORROSION. (2018). doi:10.5006/2729.

[124] Z. Szklarska-Smialowska, Pitting corrosion of aluminum, Corros. Sci. (1999). doi:10.1016/S0010-938X(99)00012-8.

[125] G.S. Chen, M. Gao, R.P. Wei, Microconstituent-Induced Pitting Corrosion in Aluminum Alloy 2024-T3, Corrosion. (1996). doi:10.5006/1.3292099.

[126] J.M. Papazian, E.L. Anagnostou, S.J. Engel, D. Hoitsma, J. Madsen, R.P. Silberstein, G. Welsh, J.B. Whiteside, A structural integrity prognosis system, Eng. Fract. Mech. (2009). doi:10.1016/j.engfracmech.2008.09.007.

[127] P. Khullar, J.V. Badilla, M.L.C. Lim, S.C. Hahn, D.W. Ellis, R.G. Kelly, Critical factors affecting intergranular corrosion of AA5083 under atmospheric axposures, in: ECS Meet. Abstr., 2015.

[128] S. Kim, J.T. Burns, R.P. Gangloff, Fatigue crack formation and growth from localized corrosion in Al-Zn-Mg-Cu, Eng. Fract. Mech. (2009). doi:10.1016/j.engfracmech.2008.11.005.

[129] N.E.C. Co. The Effect of Corrosion Damage Morphology on Fatigue Crack Initiation and Small Crack Propagation Behavior of AA 7050-T7451, University of Virginia, 2018.

[130] P. Westenberger, AVIZO-3D visualization framework, in: Geoinformatics Conf., 2008: pp. 1–11.

[131] J.S. Lim, Two-Dimensional Signal and Image Processing, Englewood Cliffs, NJ, Prentice Hall. (1989).

[132] M. Gao, R.P. Wei, P.S. Pao, Chemical and metallurgical aspects of environmentally assisted fatigue crack growth in 7075-T651 aluminum alloy, Metall. Trans. A. (1988). doi:10.1007/BF02645142.

[133] A.M. Korsunsky, D. Dini, F.P.E. Dunne, M.J. Walsh, Comparative assessment of dissipated energy and other fatigue criteria, Int. J. Fatigue. 29 (2007) 1990–1995. doi:10.1016/j.ijfatigue.2007.01.007.

[134] G.M. Castelluccio, D.L. McDowell, Microstructure and mesh sensitivities of mesoscale surrogate driving force measures for transgranular fatigue cracks in polycrystals, Mater. Sci. Eng. A. (2015). doi:10.1016/j.msea.2015.05.048.

[135] S. Güngör, L. Edwards, Effect of surface texture on the initiation and propagation of small fatigue cracks in a forged 6082 aluminium alloy, Mater. Sci. Eng. A. (1993). doi:10.1016/0921-5093(93)90493-X.

[136] R. Bandyopadhyay, P. Veerappan, M.D. Sangid. Uncertainty quantification in the mechanical response of crystal plasticity simulations. Submitted to JOM, 2018.

[137] K. Kapoor, M.D. Sangid, Initializing type-2 residual stresses in crystal plasticity finite element simulations utilizing high-energy diffraction microscopy data, Mater. Sci. Eng. A. (2018). doi:10.1016/j.msea.2018.05.031.

[138] M.L.N.M. Melo, E.M.S. Rizzo, R.G. Santos, Predicting dendrite arm spacing and their effect on microporosity formation in directionally solidified Al-Cu alloy, J. Mater. Sci. 40 (2005) 1599–1609. doi:10.1007/s10853-005-0659-y.

[139] T.X. Araujo Sousa, R. Gomes dos Santos, R. Batista de Andrade, J.R. Pereira Rodrigues, M. de L. Noronha Motta Mello, Overheating influence on solidification - thermal variables and microstructure formation of aluminium alloy, Rem Rev. Esc. Minas. 62 (n.d.) 481–486.